Effect of Viscosity Contrast and Wetting on Frictional Flow Patterns

Swansea University
Prifysgol Abertawe

Dawang Zhang

Faculty of Science and Engineering
Swansea University

Submitted to Swansea University in fulfilment of the requirements for the Degree of
Doctor of Philosophy

November 2022

To my beloved family...

Declarations

This work has not previously been accepted in substance for any degree and is not being concurrently submitted in candidature for any degree.

Signed .....dawang zhang.....

Date .....28/11/2022.....

This thesis is the result of my own investigations, except where otherwise stated.
Other sources are acknowledged by footnotes giving explicit references. A bibliography is appended.

Signed .....dawang zhang.....

Date .....28/11/2022.....

I hereby give consent for my thesis, if accepted, to be available for photocopying and for inter-library loan, and for the title and summary to be made available to outside organisations.

Signed .....dawang zhang.....

Date .....28/11/2022.....

The University's ethical procedures have been followed and, where appropriate, that ethical approval has been granted.

Signed .....dawang zhang.....

Date .....28/11/2022.....

Publications

The following publications are based on the research presented in this thesis:

(1) **Dawang Zhang**, James M. Campbell, Jon A. Eriksen, Eirik G. Flekkøy, Knut Jørgen Måløy, Christopher W. MacMinn and Bjørnar Sandnes. Frictional fluid instabilities shaped by viscous forces. *Nature Communications*. (Under Review)

(2) **Dawang Zhang** and Bjørnar Sandnes. From capillary fracturing to blasting in wet granular packing. (In Preparation)

(3) **Dawang Zhang** and Bjørnar Sandnes. Frictional flow patterns in repelling, imbibing and mixed-wet granular material. (In Preparation)

Acknowledgements

I would like to thank firstly Bjørnar Sandnes, the best supervisor ever and forever. Thank you for your invaluable patience and advice over the past four years. Your philosophy and enthusiasm to the science has brought me deeper interests to the world. Your approach to the research has taught me how to walk as a new toddle in the science world. You have opened me a window to see how beautiful the patterns can be whatever in my research area or beyond. You are not only the tutor of my research work but also life.

I want to thank Prof. Chenfeng Li, thank you for leading me pursuing PhD here in Swansea University. Your insightful advice has inspired me a lot during my research. I want to thank Deren Ozturk, Miles Morgan and James Campbell for the help and comments they gave me in the experiment, simulation and data analysis. Additional thanks to Peter Angerman for being great colleague. I want to thank Jinsheng Wang, Bin Chen, Jinlong Fu, Sizeng You, Bingbing Chen, Shan Zhong, Shuai Shu, Xiangyun Ge and others for being great fellow travelers and friends on my PhD journey. Many thanks also to Christopher MacMinn, Jon Eriksen, Eirik Flekkøy and Knut Måløy for all the discussions and advice in my study.

To my parents, brother and sister, thank you for your continuous encouragement and support. The life experiences you shared with me have taught me how to get through difficulties. The support from you and the happiness because of you give me strength to finish my PhD.

Special thanks to Swansea University for offering me the scholarship for tuition fee and providing great facilities for my scientific work. Many thanks to China Scholarship Council (CSC) for a 48-month fund covering my living costs.

Abstract

Multiphase flows involving two fluids and a granular material occur in such diverse scenarios as mud and debris flows, methane venting from sediments, degassing of volatiles from magma, and the processing of granular and particulate systems in the food, pharmaceutical, and chemical industries. The presence of the granular material introduces solid friction as a governing force in the dynamics, alongside viscosity and capillarity. This multitude of interacting elements and forces can give rise to instabilities and the emergence of patterns, making these multiphase frictional flows inherently difficult to predict or control. We refer to these granular-fluid-mixtures as frictional fluids.

We explore here systematically the competition between frictional, viscous, and capillary forces in frictional fluid flows. Viscously stable (more viscous invading fluid) and unstable (more viscous defending fluid) scenarios are investigated, and we study wetting conditions from drainage (grains wetted by defending fluid), through mixed-wet, to imbibition (grains wetted by invading fluid). The emerging flow patterns are studied using both experiments and simulations. Firstly, the effect of viscous stabilization on frictional finger pattern formation is discovered. When the flow is viscously stable, increasing the viscous force leads to a striking transition from the growth of one solitary finger to the simultaneous growth of multiple, wandering fingers to the axisymmetric growth of a radial spoke pattern as the flow is increasingly viscously stabilised. When the flow is viscously unstable, in contrast, the invasion patterns transition from frictional fingering to classical viscous fingering as viscous force increases beyond a critical fluidisation threshold. Later, the effects of parameters such as plate spacing and its gradient along the cell, and the tilt angle of the cell, on the pattern formation is studied. Furthermore, viscously unstable fracturing in drainage is studied. A small change on the volume fraction of granular material which govern the friction stress in the system, can convert the invasion from bulldozing fractures to pore invasion. At high air pressure, the fractures form a radially symmetric pattern where the fractures also gradually widen over time. Finally, viscously stable displacement from imbibition through mixed-wet to drainage is explored. Here, three types of invasion dynamics happens simultaneously or sequentially: pore invasion, capillary bulldozing and erosion, and five regimes of invasion patterns are identified: (I) pure pore invasion, (II) pure capillary bulldozing, (III) capillary bulldozing followed by pore invasion, (IV) pore invasion followed by erosion and (V) capillary bulldozing followed by pore invasion and erosion. These are caused by the relative importance of capillarity, friction and viscous pressures determined by the experimentally controlled variables.

Table of contents

List of figures

Nomenclature

Roman Symbols

$2R$	finger width
Δp_{cap}	capillary pressure difference accross the interface of two fluids
ΔP_b	threshold pressure to sprout a new finger
Δr_b	distance from the finger tip to the the point where viscous pressure reach ΔP_b
η	viscosity
κ	Janssen coefficient
$\mathcal{M}$	the log of the viscosity ratio between the invading fluid and defending fluid
W	wettability
$\mid \nabla P \mid$	fluid pressure gradient
μ	friction coefficient
ϕ	filling fraction of the granular materials
σ	stress required to push a bulldozed front forward to the thickness L of the front
σ_0	fitting number to experimental results
σ_{xx}	horizontal bulldozing stress
σ_{zz}	vertical stress exerted on the Hele-Shall cell by jammed granular front
θ	contact angle
φ	self-defined filling level of the granular packing, is equal to granular layer thickness over plates gab

C_b proportion of hydrophobic beads in the granular packing

D_{visc} viscous deformability

G frictional strength of the granular layer

k permeability of the granular packing

N number of active fingers

n porosity of the granular materials

P_t threshold pressure for finger growth

u characteristic velocity

Chapter 1

Introduction

The thesis is focused on multiphase flows involving granular media, the effect of viscosity contrast between the invading and defending fluids, and the wetting between fluids and grains. Such flows are of great importance for the study of contaminants treatment in soil [1, 2], CO_2 storage [3–5], oil recovery [6, 7], and methane migration in sediments [8–11]. In this section, we will introduce some of the diverse range of flows and fluid displacement in the nature, science and engineering, and point out the novelty of the thesis.

1.1 Flows forming patterns

1.1.1 Pattern formation in nature

Flows, macroscopic or microscopic in scale, are ubiquitous in the physical world. The flow of air generates the wind, the wind shapes the surface of our planet and creates various landforms such as mushroom rocks, barchan dunes and yardang. The flow of liquid, typically river flow, shapes the land by erosion and deposition. Apart from their benefits and hazards to the creatures of this planet, beautiful patterns themselves are worth to be explored for the insight they give into how the physical world operates.

In the formation of the meanders in rivers, a process regarded as unstable [12, 13], while a force balance exists in the system, the higher fluid velocity at the outer bank causes higher shear stress and thereby erosion, and the lower fluid velocity at the inner bank lead to lower shear stress and thereby deposition [14]. Finally, the meander may become an oxbow lake along the river side as shown in Figure 1.1 a.

Lava, a mixture of molten rock, crystal particles and gas, forms splendid patterns when it flows, and these patterns are determined by the physical properties of the lava. Lava flow has been explained in [15], where a prediction model for flow dimensions was developed. In

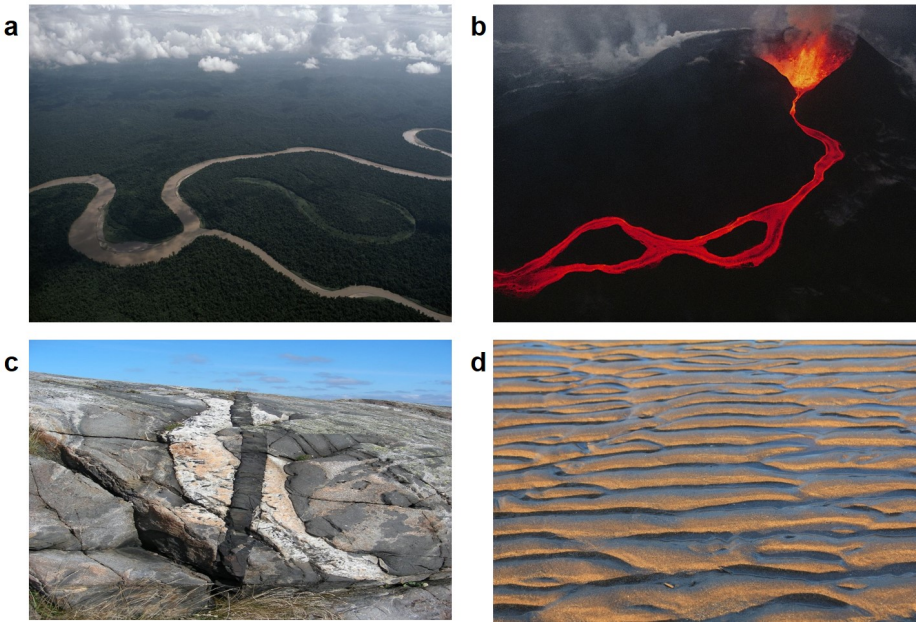

Fig. 1.1 Pattern formed by flow in nature. (a) Oxbow lake [20]. (b) Lava flow [21]. (c) Igneous intrusions [22]. (d) Beach sand ripples [23].

Figure 1.1c, molten magma can intrude and displace existing country rock to form an igneous intrusion. The invasion is driven by the buoyancy because of the much smaller density of magma than its source rock [16].

Ripple marks are commonly seen in nature and a plenty of studies have focused on the mechanism of pattern formation in various situations, the desert dunes [17], the river dunes [18], the extraterrestrial dunes [19] and so forth. In Figure 1.1(d), the sand ripples one can observe on a beach were formed by the shearing of the oscillating waves.

These are but a few examples of pattern formation in the physical world. The patterns are created spontaneously by the forces involved and the interactions between the fluids, gases and grains. To understand such flows we must uncover these forces and interactions to enable us to predict and control natural and industrial processes.

1.1.2 Patterns formed by fluid-fluid displacement

The way in which one fluid displaces another has been of interest to scientists for decades. One principal tool in this effort has been the Hele-Shaw cell, a pair of parallel glass plates closely spaced to reduce fluid dynamics to an essentially two-dimensional process. The plates can be put horizontally [24], vertically [25] or tilted [26]. There are normally two ways of fluid flow into Hele-Shaw cell: injection [27–29] and withdrawal [24, 26]. The injection

inlet or withdrawl outlet can be at the center of the cell or close to one side of the plate. And the displacement of the fluids can be flow-rate controlled or pressure controlled.

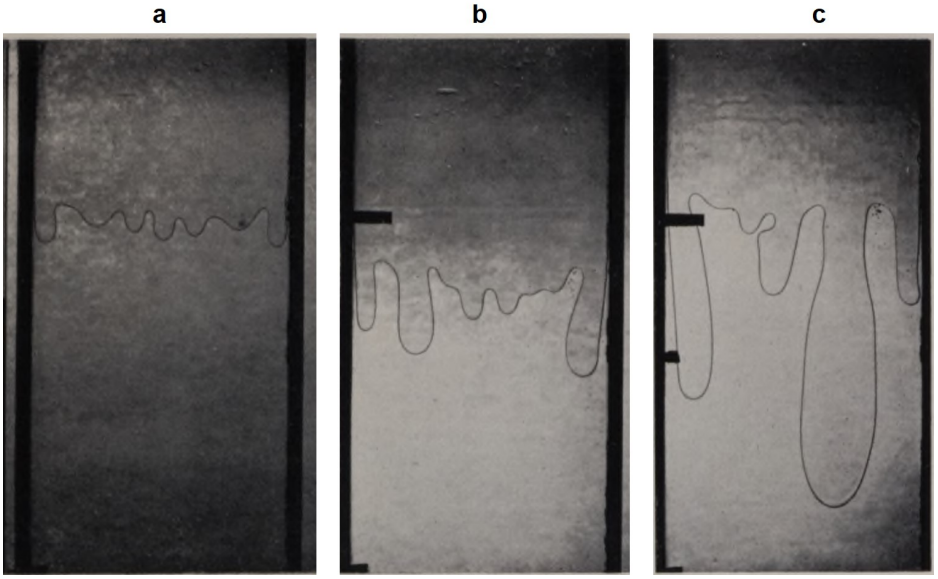

Fig. 1.2 Viscous fingering formation after air invading (downwards in the figure) the glycerine within a Hele-Shaw cell [25]. (a) Early stage of the instability on the air-glycerine interface. (b) Development of the pressure screening of the fluid falling behind the most advanced finger. (c) A finger grows ahead of its neighbours because of the instability. The width of channels are all 12 cm.

Saffman and Taylor in their groundbreaking paper in 1958 pumped air (lower-viscosity fluid) into a Hele-Shaw cell filled with glycerine (higher-viscosity fluid), and demonstrated the phenomenon of viscous fingering [25], in which an invading fluid injected into an immiscible defending fluid produces an instability on the interface as shown in Figure 1.2. The pressure gradient is located in the high viscosity fluid, and therefore any spontaneous bulge on the interface will protrude deeper into the high-viscosity fluid and experience a slightly steeper pressure gradient as a result. The steeper pressure gradient causes the bulge to accelerate. The positive feedback between deformation and velocity increase is at the heart of the instability that causes the viscous fingers to develop.

Bertrand *et al*. revisted Saffman-Taylor experiment by injecting the aqueous solutions into a Hele-Shaw cell filled with silicon oil [30]. They varied the contact angle of the cell by coating Norland Optical Adhesives (NOA81) on the surface of both plates. The contact angle ranged from $120\pm2^\circ$ to $7\pm2^\circ$, *i.e*., the surface of the cell varied from non-wetting to wetting to the invading fluid (aqueous solutions). With non-wetting surface experiment, the tip splitting of the viscous fingering similar to Saffman-Taylor pattern was observed.

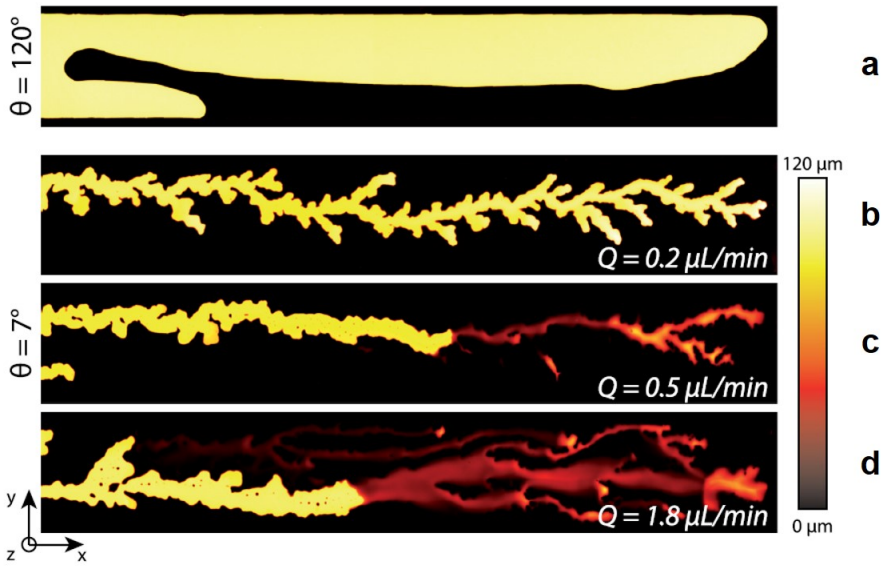

Fig. 1.3 Aqueous solution (yellow region) invades silicon oil (black region) within a Hele-Shaw cell to form different fingering patterns by varying the wetting condition (quantified by contact angle θ) of the plates and fluid invasion rate [30]

.

However, with wetting-surface experiment, different patterns were observed as shown in Figure 1.3. They verified the reason behind was the entrainment of thin liquid films.

1.1.3 Pattern formation in granular systems

By adding granular material into the defending fluid, the patterns formed will vary. Sandnes *et al*. in 2007 mixed a water/glycerol solution and glass beads together to form a granular mixture [24]. They filled the Hele-Shaw cell with the mixture and kept the edges open to the surrounding air. The fluid was then withdrawn at a slow rate such that the viscous forces were negligible. A labyrinth pattern was observed as shown in Figure 1.4,where the characteristic spacing between fingers resulted from the competition between capillary forces and the frictional stress.

Later in 2011, they performed performed experiments where air contained in a "reservoir" syringe was injected at different rates into a linear cell containing a grain-liquid mixture [27]. By varying the volume of air in the reservoir and filling fraction of glass beads, frictional fingers and bubbles were observed at low injection rate. The new pattern – “stick-slip bubbles” were found to be relevant to both filling fraction and air volume and more likely to appear in the experiments with high filling fraction and larger air volume. The bubbles appeared when the system entered an intermittent regime, where high friction caused the front to stop moving.

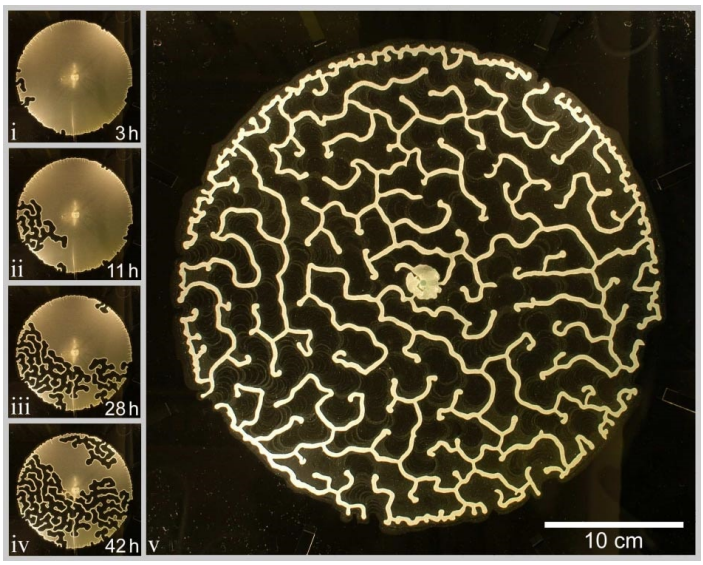

Fig. 1.4 Labyrinth pattern after air (black region) invades mixture of glass beads and glycerine solution (gold region) [24]. Images i–iv show the time evolution of finger growth.

The pressure built in the air reservoir which was being continuously compressed by the piston of the syringe pump, and the larger the syringe volume, the larger the resulting bubble when the front finally broke. They also observed a transition from the frictional to the viscous regime when increasing the air injection rate. In the frictional regime, the pattern formation was mainly governed by the friction stress because of the negligible viscous forces at low flow rate. In the viscous regime, a locally fluidized front was formed at moderate injection rate (from 0.3 to 3mL/min in the paper), a new "coral" structure was discovered. At even higher injection rate, the viscous forces of the fluid dragged the granular bed along and the mixture now behaved very much like a suspension. They therefore observed viscous fingering that was similar to what occurred in pure fluid displacement. The patterns mentioned above is shown in Figure 1.5

Eriksen *et al*. tilted the cell to different angles to study the effects of gravitational potential on pattern formation [26]. A small increase of the tilt angle α, say 1°, would change the patterns significantly. In a horizontally placed cell, finger growth was random and nondirectional, the cell space was partially displaced by the air and other places remained undisturbed. In a tilted cell, the fingers grew along each other downwards, the air invaded the whole space of the cell in a compact pattern of aligned fingers. This was because the gravity provided a hydrostatic stabilization of the height of the interface between the dense defending fluid and the invading air. They also changed the filling fraction of granular material and observed a transition from vertical growth to horizontal growth of fingers as shown in Figure 1.6.

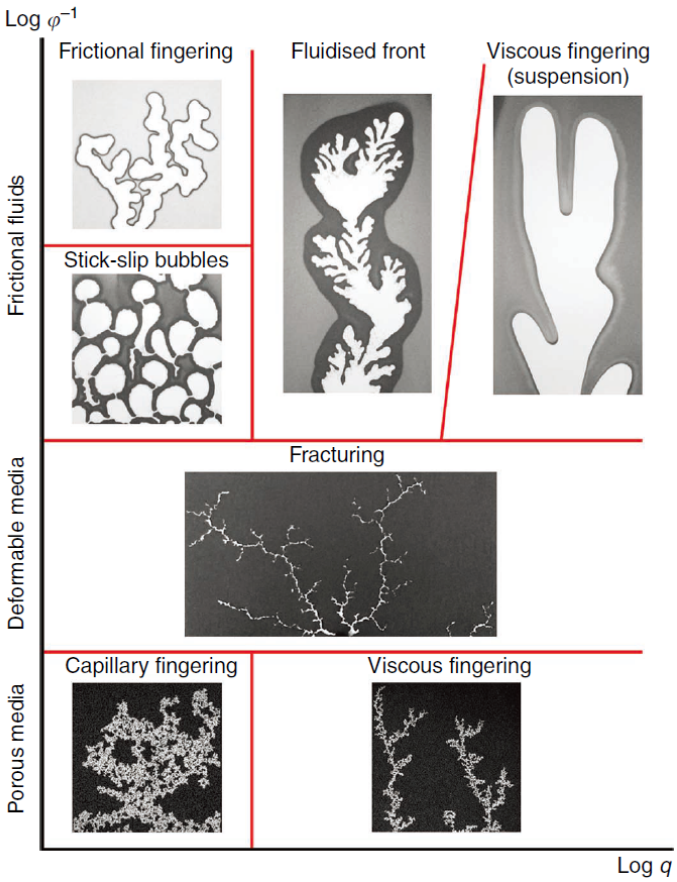

Fig. 1.5 Phase diagram of patterns formed after air (white region) invades granular material with different volume fractions (y axis in the figure) at different injection rates (x axis) [27].

Chevalier *et al.* varied the grain fraction in the granular suspension by density matching and observed fingering and hydrofracturing-like patterns after injection of air [31]. At grain fraction $\phi < 50\%$, fingering was observed at different finger velocities, although the finger shape became less uniform and had finger branching occurring at high velocity. At $\phi > 50\%$, fracturing was found to be the reason of rearrangement of the local grains around the fracture body when the packing was just below the jamming point.

This fracturing was later observed in many studies [32–35]. Holtzman *et al.* described a transition from capillary fingering to viscous fingering in porous media flows, and a transition from fingering to capillary fracturing by changing the air invasion rate and the confining force exerted on the glass beads [36].

Xue *et al.* pumped pressurized air into a dry granular packing within a Hele-Shaw cell [37]. They studied the effects of boundaries (by changing the gap) and angularity of grains on the pattern formation. They observed a transition from stable to unstable displacement after increasing the angularity of the grains or decreasing the gap between

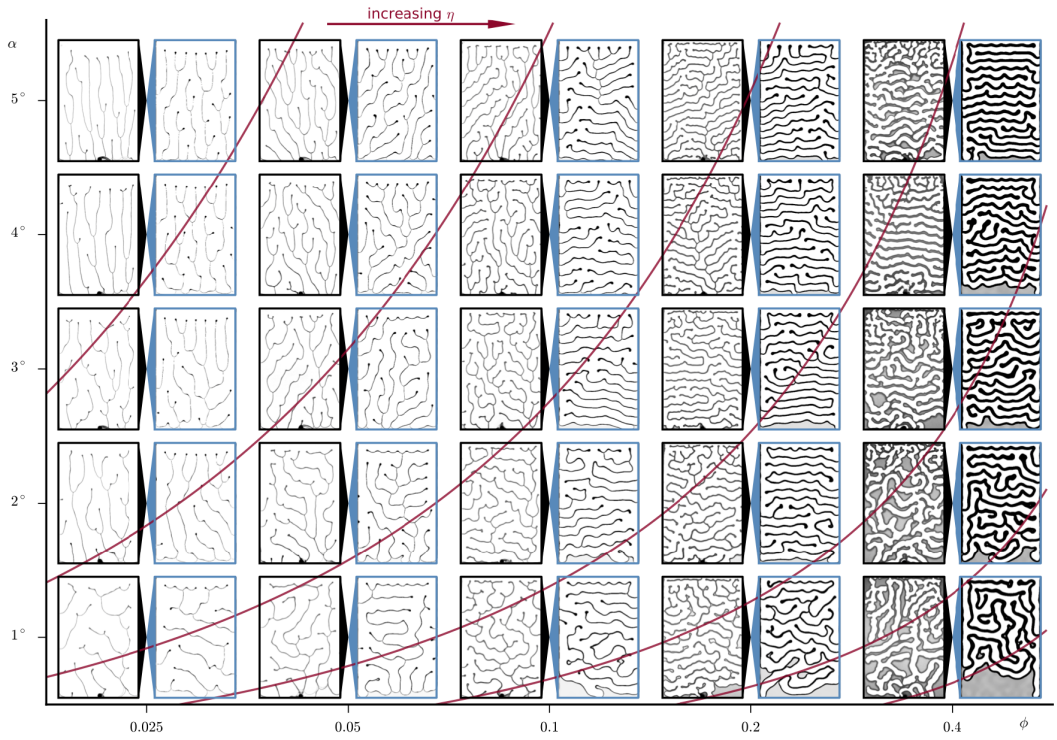

Fig. 1.6 Patterns formation after air (white region in the images) invading to the suspension within tilted Hele-Shaw cell [26]. The variation of the patterns is related to the tilt angle α and the volume fraction ϕ. The black frames show experimental results and the blue frames the corresponding simulation results. η, defined by the authors, is the ratio between the noise of the system and the hydrostatic difference of with a horizontally oriented finger. Red lines indicate the contours of a constant η.

the plates. Less angular grains or larger gap made the packing more likely to fluidize, i.e., increased the flowability of the particles, such that the invasion front became more stable. Similar results have observed in [29, 38].

Pattern formation in shear-thickening [39] and shear-thinning [40] suspensions have been studied in 2D Hele-Shaw geometries. In the case of discontinuous shear thickening, the authors pumped the pressurized air into the cornstarch suspensions in [39]. Three distinct patterns were discovered by changing the volume fraction of cornstarch and pressure of air: viscous fingering, dendritic fracturing and system-wide fracturing as shown in Figure 1.8.

Some researchers have also focused on the pattern formation in 3D systems [41–47]. Dalbe and Juanes injected silicon oil into a 3D deformable granular medium saturated by glycerol. By using a the planar laser-induced fluorescence (PLIF) 3D imaging technique, the authors were able to observed the invasion morphodynamics of different places in 3D packing with the laser sheet [41]. The increase of the injection rate or the decrease of confinement stress of the granular packing led to a transition from pure fluid-fluid displacement in pores

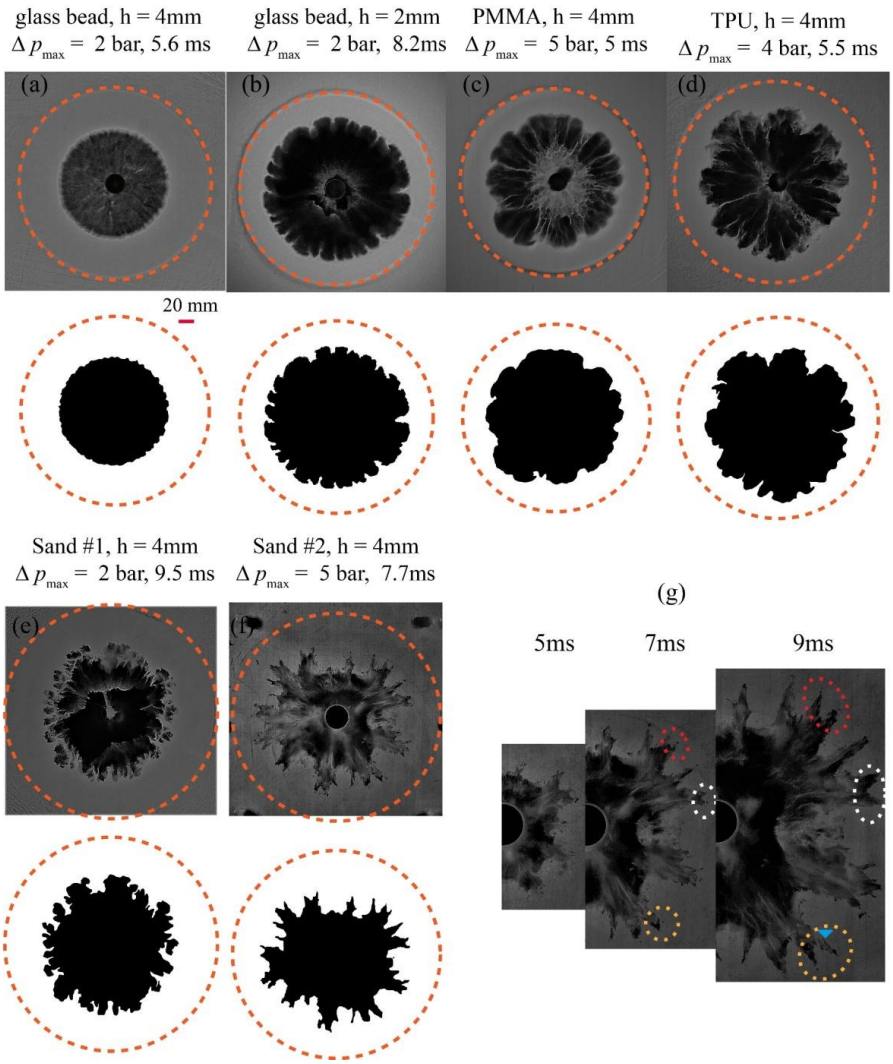

Fig. 1.7 Pattern formation after invasion of pressurized air into the dry granular packing within the Hele-Shaw cell [37]. h is the gap, ΔP_max is the air pressure before invasion, ms is the unit of time.

to the deformation of the packing. This transition was explained to be the balance between the frictional and viscous forces by a analytical model.

In summary, previous studies have mainly focused on the situation when a less/equally viscous fluid invades the granular material saturated by a higher/equally viscous fluid. In the current thesis, we will study the opposite situation when a high viscous fluid invades the granular material saturated by a less viscous fluid.

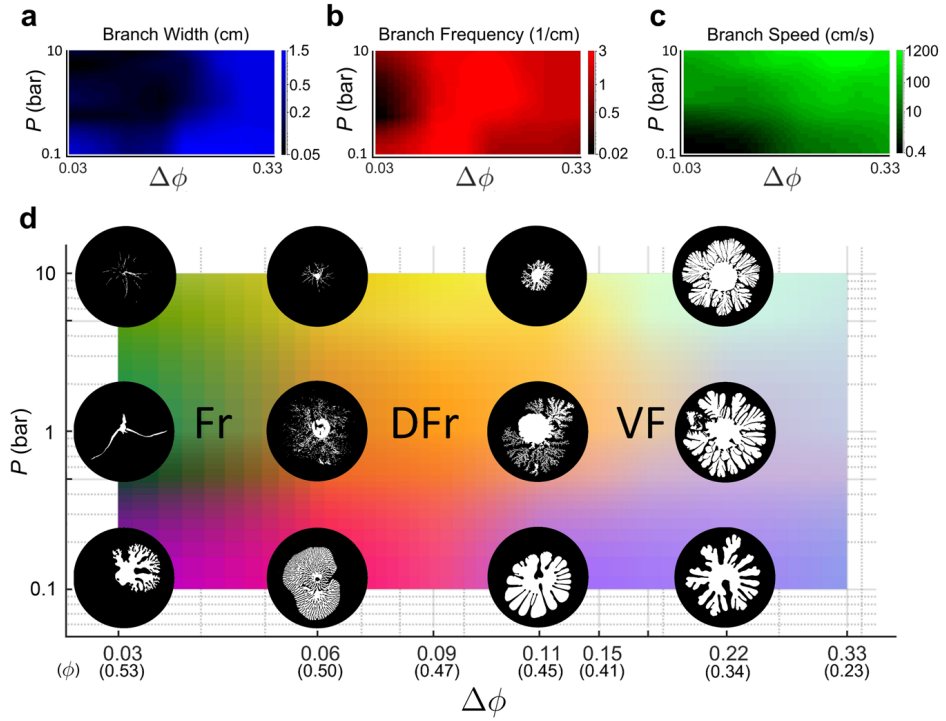

Fig. 1.8 Phase diagram for invasion patterns in a shear thickening fluid [39]. Pattern formation is controlled by both volume fraction and pressure. Fr represents fracturing, DFr represents dendritic fracturing and VF represents viscous fingering. White regions in the images is the area invaded by the air.

1.2 Wettability control on interfacial behavior

Wettability of a solid surface by a liquid, quantified by the contact angle, governs many phenomena in both nature and engineering. The contact angle is generally measured where the vapor-liquid interface meets the solid surface. At contact angle larger than 90°, a solid surface such as lotus leaves [48] exhibits hydrophobicity: water is non-wetting to the surface of the lotus leaves. At contact angle smaller than 90°, a surface such as for example clean glass is hydrophilic: water is wetting to the surface of the clean glass. Self-cleaning textiles has been studied widely based on either hydrophobic or hydrophilic approaches [49]. Water-repellent soil has received extensive attention because of its hazards to erosion and plant growth [50]. Fluid-fluid displacement governed by wettability has also been universally studied in the field of CO_2 storage [3–5] and oil recovery [6, 7].

1.2.1 Fluid displacement in homogenously wetted porous media

When one fluid displaces another that hosts the granular material, typically at the gas-liquid-solid interface, the wettability of the granular material can govern the flow pattern. Fluid displacement in porous media is a classic example and has received much research attention for decades. According to the wetting conditions of the fluid to the porous media, the ways of fluid-fluid displacement can be classified into drainage and imbibition. If a fluid that is non-wetting to the porous medium, displaces a wetting fluid saturating the porous media, it referred to as drainage. When the invading fluid is wetting to the porous medium this is referred to as imbibition.

Most of the studies have focused on drainage. In [51], the authors injected air into a 2D porous medium filled with glycerol, and discovered the viscous fingering which was similar to the pattern formed by diffusion-limited aggregation (DLA) considering the appearance and fractal dimension [52].

Haines jumps is a well-known phenomenon in slow drainage where the non-wetting fluid breaks through the narrower pore throat and rapidly invades the wider pore space, causing a capillary pressure jump [53–55]. Steffen *et al.* obtained 3D real-time images of Haines jumps by using an advanced X-ray microtomography [56]. They found that 10-20 pores was cascaded and dissipated 64% of the energy in a jump event.

Lenormand and Zarcone in 1985 studied the invasion pattern after a non-wetting fluid invading to a wetting fluid (drainage) in an Etched Network [57]. Later in 1990, Lenormand studied the invasion patterns of both drainage and imbibition, and the phase diagrams for both were obtained [58]. In drainage, three regimes were identified: 1) capillary fingering at low capillary number and the viscous forces were negligible in both invading and defending fluid; 2) stable circular invasion at high capillary number and the pressure drop was mainly inside the invading fluid; 3) viscous fingering at high capillary number and the pressure drop was mainly inside the defending fluid. In imbibition, stable circular invasion and viscous fingering similar to the situation in drainage at high capillary number were identified. In addition, the continuous capillary domains (without film flow) at intermediate capillary number and the discontinuous capillary domains (with film flow) at low capillary number were classfied.

Zhao *et al.* studied the invasion patterns under different wetting conditions ranging from strong drainage to strong imbibition, and at different capillary numbers in porous media [59] as shown in Figure 1.9. At low capillary number, except the strong-imbibition experiment, the invasion front generally became more and more compact with the decrease of contact angle θ. In strong imbibition case, the fluid displacement was even more incomplete than that in strong drainage case. The authors explained this as the results of corner flow which had been studied widely [60–65]. At higher capillary number, they observed a decrease

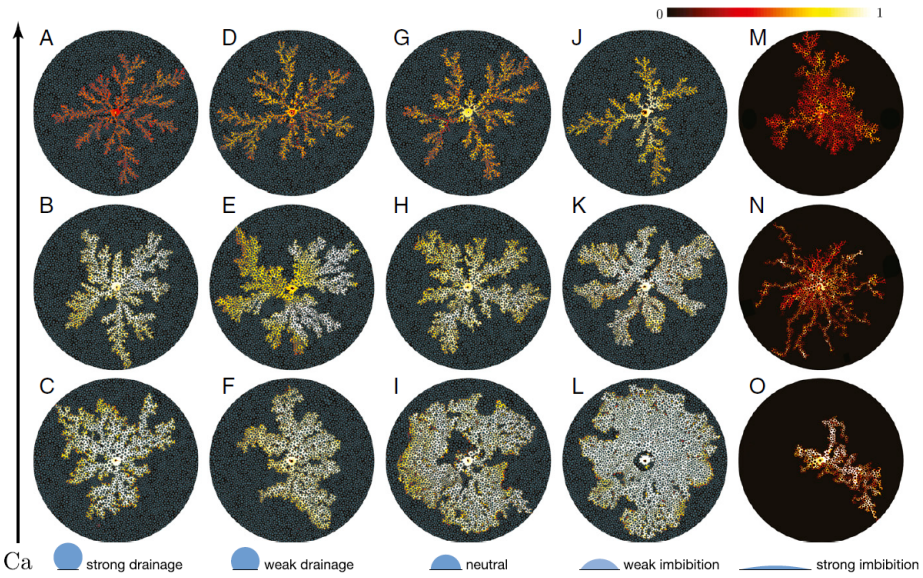

Fig. 1.9 Phase diagram for invasion patterns under different wetting conditions and at different capillary number Ca in porous media by Zhao *et al.* [59]. Water is injected from the center into the porous medium saturated by the silicone oil, with the colormap represents the saturation of the invading water. Except the situation of strong imbibition, the compactness of the pattern generally decreases as the invading water became less wetting to the granular material.

of displacement completion in all different wetting conditions, *i.e.*, the patterns became less compact. This was caused by the trailing films of the defending fluid with a higher viscosity in drainage, and the leading films of the invading fluid with a lower viscosity in imbibition. Furthermore, at higher contact angle, *i.e.*, the invading fluid became less wetting to the granular material, a decrease of the compactness of the patterns was observed. Corresponding numerical studies have also been widely published [66–73].

1.2.2 Fluid displacement in heterogenously wetted porous media

The wettability of porous media in nature and engineering is generally heterogenous, causing a fluid displacement behavior different from that in homogenously wetted porous media.

According to the study by Murison *et al.* in [74], the situation of wetting heterogeneity in porous media were divided into four types: Patchy, Janus, Mixed and Clusters. The authors performed the capillary pressure saturation (CPS) experiment, with water displacing the oil initially saturating the bead pack and then oil reinvading the pack. They found that the Pathy samples had the biggest hysteresis loop opening (the distance between the saturation lines of water and oil invasion), while the Cluster samples had the smallest opening in CPS curves.

By X-ray tomography, they observed a more compact invasion front in Pathy and Janus samples, while in Mixed and Clusters samples they observed a fingering-like invasion front.

Ahmed *et al.* identified a broad distribution of contact angles in porous media using X-ray tomography, and discovered the relationship between the wettability and surface roughness [75]. Amir *et al.* used direct numerical simulations to discover effects of the heterogeneous wettability on fluid displacement in porous media [76]. Kamaljit et al. verified the conductance of oil in oil-wet corners of the mixed-wet porous media during brine flooding [77], in contrast to the disconnected oil ganglia in pure water-wet system [78].

Invasion patterns in mixed-wet porous media are different to those observed in pure water-wet (immbibition) and water-repellent (drainage) systems [79]. Using X-ray imaging, they observed a phenomenon of interface pinning which prevented the interface recession and snap-off during invading process. The order of invasion to the pore with varied throat radius was also found to have no filling preferences, unlike the situation in imbibition and drainage.

Many of the previous studies have focused on the invasion patterns in fixed porous media at different wetting conditions, but none of the study to our knowledge has discovered the invasion patterns in deformable granular materials at mixed-wet conditions, and this will be one of the focuses of the current thesis.

1.2.3 Wettability control on particle rearrangement

Meng *et al.* numerically studied the effects of wettability on pattern formation after a less viscous fluid invaded a granular packing saturated by a more viscous fluid [80]. Three regimes: cavity expansion & fracturing, frictional fingers and capillary compaction were observed by only changing the contact angle, with the first regime occurring at contact angle 75-140°, the second regime occurring at 65-70° and the third regime occurred at 46-55°. More studies on this have also seen in [81, 82] and the similar results were obtained.

When a droplet of water rolls accross the surface of a bed of hydrophobic beads (in the scale of nm to tens of μm), self-arrangement of the particles around the droplet will be observed. The objects formed this way are called *liquid marbles* which were reported 20 years ago by Aussillous *et al.* when they tried to develop a new method for transporting small amounts of liquid on a solid surface [83]. When the particles attaches to a droplet, proportions of the liquid-air and the solid-air interfacial area are replaced by the solid-liquid interface. In this attachment before the particles are engulfed, the changes of the net surface free energy (solid-liquid surface free energy after attachment minus solid-air and liquid-air surface free energy before attachment) of the particles are calculated to be always reduced, such that the attachment of the particles to the droplet is energetically favored [84, 85].

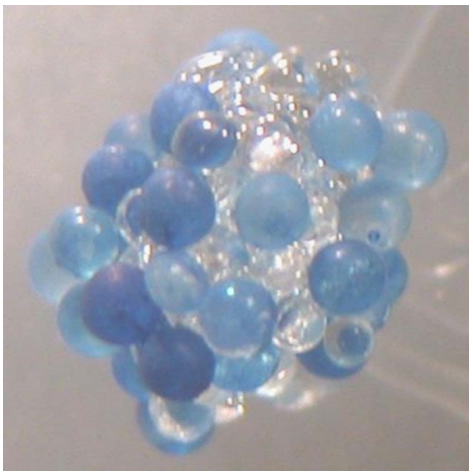

Fig. 1.10 Self-organization of hydrophobic (blue) and hydrophilic (white) beads on the surface of water droplet [92]. The structure was formed after drying of the droplet.

A wild fire could volatilize waxy compounds in surface litter layer which later condense on the soil and forming the water-repellent soil [86, 87]. Water-repellent soil can cause hazards such as plant death, soil erosion and hill slope runoff [88–90]. Many studies have focused on the principles and properties of water-repellent soil [50, 91]. Water repellency of the soil is promoted by drying. McHale *et al.* studied the drying process of the water on the bed of hydrophobic beads and found the lifting and self-coating of hydrophobic beads on the droplet surface to form a temporary liquid marbles. They mixed the hydrophobic and hydrophilic beads together and repeated the experiment above. Both types of beads were observed to be lifted, but only hydrophobic beads were seen on the outer skin. After drying of the droplet, a structure, composed of outer hydrophobic beads and inner hydrophilic beads, was formed (as shown in Figure 1.10).

1.3 Layout of the thesis

The current thesis will study the physics of pattern formation by fluid-fluid displacement in the granular material, which is controlled by the viscosity contrast between the invading and defending fluid, and the wettability condition of the materials. If we define $\mathcal{M}$ as the log of the viscosity ratio between the two fluids, $\mathcal{M} = \log(\eta_{\text{def}}/\eta_{\text{inv}})$, where η_{inv} is the viscosity of the invading phase and η_{def} that of the defending phase. We define wettability $\text{W} = -\cos\theta$ by the contact angle θ inside the invading fluid against the solid material. Negative W ($-$W), where the granular bed is wetted by the invading fluid, results in spontaneous imbibition, whereas $+$W results in the granular bed resisting penetration by the invading fluid (drainage). Such that we obtained a quadrantal diagram as shown in Figure 1.11. Chapter 2 introduces

the basic concepts and fundamentals relevant to the study of the thesis. Chapter 3 studies the physics of frictional fingering in a viscously stable condition. Chapter 4 studies the effect of viscosity on the pattern formation and compares the patterns formed in viscously-stable and viscously-unstable situations. Chapter 5 focuses on the alignment of the frictional fingering in the linear Hele-Shaw cell. Chapter 6 presents viscously unstable fracturing in different conditions. Chapter 7 demonstrates the patterns formed in mixed-wet granular materials. Finally, Chapter 8 summarises the results and provides recommendations for future work.

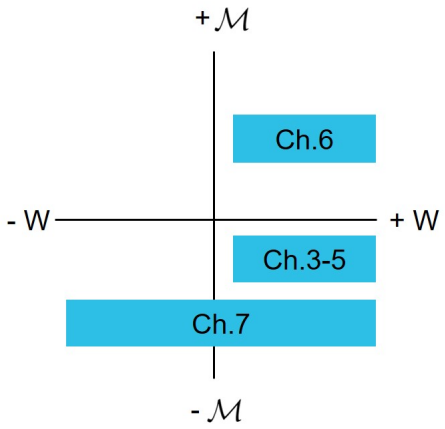

Fig. 1.11 Quadrantal diagram of viscosity ratio $\mathcal{M}$ and wettability $\mathrm{W} = -\cos\theta$ to show the study focus of each chapter.

Chapter 2

Basic concepts and fundamentals

In this chapter we will introduce the basic concepts and fundamentals relevant to the topic of the thesis. The properties of granular materials and grain-grain friction will be explained in the first section. Fluid properties that determine the flow behaviour will be introduced in the second section. Interfacial physics such as wettability and surface energy will be described in the third section.

2.1 Properties of granular materials

2.1.1 Arrangement of granular packings

A porous object consists of not only granular particles but also pore space. The ratio of pore space volume V_p to the bulk volume V_b of the porous object is called porosity $n = V_p/V_b$. In contrast to porosity, the filling fraction ϕ is used to describe how much space in a porous object is occupied by the grains:

$$\phi = 1 - n = 1 - \frac{V_p}{V_b} \tag{2.1}$$

Different arrangement of particles can vary the filling fraction significantly. The densest packing possible, or so called close packing of same-size hard spheres in theory, has a filling fraction of 0.74 [93]. However, the highest filling fraction achievable is 0.64 out of all the packing methods and is verified by experiments and simulations [98–101]. Random Loose Packing (RLP) with the lower limit of the fraction 0.55 remains stable and can be achieved by some preparation methods, for instance, the sedimentation of the spheres in a liquid which has the same density as the spheres [96, 97]. Random close packing (RCP) with a filling fraction ϕ_{RCP} of 0.64 can be achieved by shaking the container.

The filling fraction ϕ of a granular packing is also significantly affected by the properties of the grains such as the diameter, the shape, the size distribution, the roughness *etc*. A lager particle diameter and a rougher particle surface can both lead to a decrease of ϕ according to [94, 97]. Donev *et al*. discovered that a packing consisting of ellipsoids, rather than spheres, can achieve a filling fraction above ϕ_{RCP}. By varying the aspect ratio of the ellipsoids, they even achieved a filling fraction approaching 0.74 [102]. The increase of the angularity or eccentricity of the particles led to a decrease of minimum and maximum filling fraction according to [103, 104]. The effect of particle-size distribution (PSD) on filling fraction has also been studied widely for different purposes [105–109], with a general conclusion that a wider range of particle size can lead to an increase of ϕ_{RCP} since smaller particles can occupy some void spaces between bigger particles.

2.1.2 Hele-Shaw flow and Darcy's law

Hele-Shaw flow, named after Henry Selby Hele-Shaw who studied the flow of water in 1898 [110], is a Stokes flow between a pair of closely spaced parallel transparent plates. A Hele-Shaw cell therefore permits he visualisation of laminar flows in 2D. The Hele-Shaw cell itself can be considered a model for porous media flows, or often the cell gap is filled with a granular or porous material that provides heterogeneity. Fluid flow through a porous medium is generally described by Darcy's law [111].

Henry Darcy in 1856 performed experiments where water flowed through beds of sand and obtained a relationship between the instantaneous flux q and pressure drop Δp [112]. Morris Muskat later refined Darcy's equation in the absence of gravity [113], and is written as:

$$q = Q/A = -\frac{k}{\eta}\frac{dp}{dx} \tag{2.2}$$

where q is the flux, Q is the volume flow rate, A is the cross-sectional area, k is the permeability of the medium, η is the dynamic viscosity of the fluid, Δp is the pressure difference across a certain distance L.

Kozeny [114] in 1927 derived an equation to estimate the permeability of granular packing. Later it was modified by Carman [115, 116]:

$$k = \frac{d^2}{180}\frac{n^3}{(1-n)^2} \tag{2.3}$$

where d is the average diameter of the particles.

The equation shows that the permeability of the granular packing is controlled by the porosity of the packing and diameter of the particles. For two sets of packings with the same porosity, smaller particles means a lower permeability. However, one needs to notice that Kozeny-Carman holds well for narrow size distributions of the particles with well-defined mean diameter, but less well for granular materials with wide size distributions or distinctly non-spherical shapes.

2.2 Force chains and granular friction

2.2.1 Granular force chains in confined geometries

Granular materials in a confined geometry can adopt significantly different states after the application of forces which will later be transmitted through the packing by the complex network of grain-grain contacts, known as force chains [117, 118]. The combination of 2D cell and photoelastic discs [119] visualized the force chain network and enabled a deeper understanding of granular systems. Majmudar and Behringer performed experiments in such a set-up, and measured the tangential and normal forces of the grains that were subject to pure shear and isotropic compression [120]. They found that the tangential forces were exponentially distributed in both cases, while the normal forces were more rounded in compression than that in shear situation. As shown in Figure 2.1, the sheared system showed longer range correlations in the direction of force chains compared to the isotropically compressed system.

The existence of force chains in granular materials leads to a well-known phenomena, jamming, that the granular materials undergo a transition between fluid-like and solid like behaviour [121, 122]. Cates *et al.* in 1998 proposed that force chains in the granular materials would form along the shear direction, which later will evolve to a rectangular force network [118]. Liu and Nagel presented a jamming phase diagram in which the load, packing fraction and temperature determined whether the grains were jammed or not [123].

Howell *et al.* performed the experiments in a Couette geometry where the photoelastic discs were sheared, and observed the jamming transition that depended on the packing density [124, 125]. The experimental results were also simulated using discrete element method (DEM) in the same period [126].

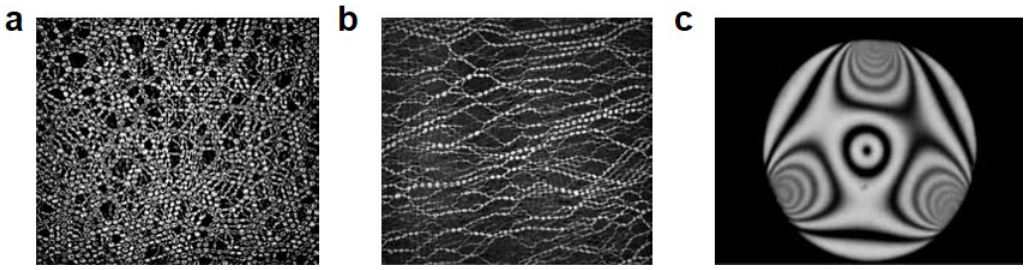

Fig. 2.1 Photoelastic images by [120]. (a) is the image of an isotropically compressed experiment, (b) is the image of a sheared experiment, and (c) is the close-up image of a single disk.

2.2.2 Janssen's friction model

The friction that resists the relative lateral motion of two solid surfaces in contact is proportional to the normal force exerted by each surface on the other according to Coulomb' friction model:

$$F_f = \mu F_N \tag{2.4}$$

where F_f is friction, μ is the friction coefficient, and F_N the normal force.

For granular materials in confined systems, there is friction between grains and the confining walls, and friction internally within the packing at grain-grain contacts. After applying a external force on such a granular packing, there are a number of potential actions. The grains could be in a state of static or dynamic frictional contacts and could be either sliding or rolling. The surfaces of the particles and the confinement wall could be dry or lubricated by liquid films. At the individual particle level, one could assign separate friction coefficients to all these scenarios, however, often the problem is simplified by assuming an overall effective friction coefficient, which may or may not be assumed the same for grain-grain and grain-wall interactions.

The normal forces at grain-grain contacts, and between grains and the walls, depends on the stress state of the system. Gravitational and externally imposed compressive stresses are transmitted through the heterogeneous force chains. Inside the confinement of a Hele-Shaw cell, the frictional resistance of a granular packing against the walls of the cell is determined by Equation 2.5 (with the grain-wall effective friction coefficient) where the normal force depends on both gravity and the externally imposed stress transmitted through force chains. Bulldozing of grains by an invading meniscus may create a granular compaction front that fills the cell from top to bottom, eventually forming a jammed granular front. If a bulldozing force is applied laterally to the jammed front, this force will be dispersed to each grain by the

contact network of the granular packing. These forces will have various directions, ultimately generating a vertical component of stress σ_{zz}.

Janssen in 1895 studied the horizontal stress of granular materials applied to the wall of a silo as a function of the filling height [127] and proposed that this stress is proportional to the vertical driving stress. Although the direction of the driving stress in their study is vertical, this relationship can also be used for horizontally driven systems. In the jammed granular front within the horizontally placed Hele-Shaw cell, the vertical stress σ_{zz} exerted on the plates can be deduced by simply multiply the driving stress or the bulldozing stress σ_{xx} with the Janssen coefficient κ:

$$\sigma_{zz} = \kappa\sigma_{xx} \tag{2.5}$$

Note that this is simply Coulomb friction (i.e. Eq.2.4) again - here applied to the continuum of grains rather than to a single solid object.

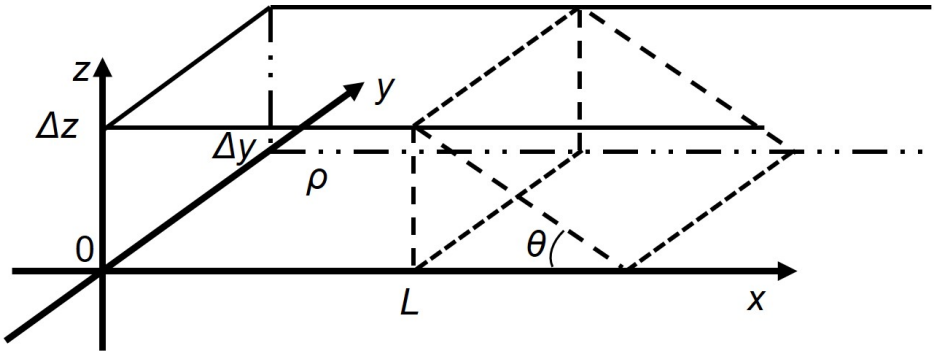

Fig. 2.2 Schematic of the compaction front of granular packing with a density of ρ [128].

Knudsen *et al.* derived a friction law that relates the interfacial stress σ required to push a bulldozed front forward to the thickness L of the front, and using the Janssen' model above found that the friction increases exponentially with L [128]. A force balance of a vertical differential slice in x direction in the compaction front (Figure 2.2) can be written as:

$$[\sigma(x) - \sigma(x+dx)]\Delta y\Delta z - \mu\sigma_{zz}(x)2\Delta y dx - g\rho\Delta y\Delta z dx\mu = 0 \tag{2.6}$$

where μ is the friction coefficient, ρ is the density of the granular packing, Δz is equal the gap b between two plates, $\sigma(x)$ here is equivalent to σ_{xx} in Equation. 2.5.

Replacing σ_{zz} with Equation 2.5, Equation 2.6 can be reduced to:

$$\frac{d\sigma(x)}{dx} = -\frac{2\mu\kappa\sigma(x)}{b} - g\rho\mu \tag{2.7}$$

Assuming the block at $x = L$ is held back by the mass inside (the triangle region in Figure 2.2), the force balance here is:

$$\sigma(L)b\Delta y = m_{tr}g\mu \tag{2.8}$$

where m_{tr} is written as:

$$m_{tr} = \frac{\rho\Delta y b^2}{2tan\theta} \tag{2.9}$$

The solution of Equation 2.7 is hereby written as:

$$\sigma = \frac{g\rho b}{2\kappa}\left[(\kappa\mu+1)\exp\left(\frac{2\mu\kappa L}{b}\right)-1\right] \tag{2.10}$$

Eriksen *et al.* used a simplified linear approximation of the model above in their papers [35, 129] written as:

$$\sigma = \frac{\sigma_\xi}{\xi}L \tag{2.11}$$

where σ_ξ is the characteristic frictional stress which can be obtained from the experiment/simulation data fitting. ξ is the characteristic length, can be assumed to be equal to the plates spacing b.

2.3 Physics of fluids and grain-liquid mixtures

2.3.1 Viscosity of the fluid and suspension

The concept of viscosity quantifies the internal frictional force between adjacent fluid layers. A fluid with low viscosity means it has little resistance to the shear stress. Viscosity relates the viscous stresses in a fluid to the rate of deformation change which can be visualized and defined in a planar Couette flow [130].

In the Couette flow, the fluid is in between two parallel plates, one is fixed and another moved along the parallel direction at a constant speed u. Consider u is low enough to avoid turbulence and top plate is in motion, the fluid in between is sheared by the top plate and the speed of fluid layers from the top down varies from u to 0.

The force acting on the top plate F that are required to overcome the friction between fluid layers and maintain the constant speed, is found to be related to u, the plate area A and plates separation y:

$$F = \eta A \frac{u}{y} \tag{2.12}$$

which can be written as the expression for viscosity η:

$$\eta = \frac{Fy}{Au} \tag{2.13}$$

The viscosity of a suspension η_s increases significantly with the increase of filling fraction of the particles suspended. When the particle concentration reaches a maximum ϕ_c, or the jamming point, the suspension ceases to flow. In [131], the authors summarized the experiment data, the theoretical predictions and the simulation results of the previous studies on the relationship between η and ϕ. All the results followed the same trend and can be collapsed to ϕ_c to fit the same curve. Among the theoretical correlations, Maron-Pierce model is the one normally used, the viscosity relative to the solvent viscosity is written as [132]:

$$\eta_s = (1 - \frac{\phi}{\phi_c})^{-2} \tag{2.14}$$

2.3.2 Hagen–Poiseuille equation

Poiseuille in 1838 performed water-flow experiments in tubes to study the relationship between volumetric flow rate Q, pressure difference ΔP, tube length L and the tube radius R [133]. Similar experimental results were published in 1839 by Hagen, in which differences between laminar and turbulent flow were observed [133]. In their papers, the equation later named the Hagen–Poiseuille equation was deduced, and the theoretical justification of the equation was given by George Stokes [134].

The Hagen–Poiseuille equation describes the pressure drop in an incompressible Newtonian fluid flowing through a long cylindrical tube of constant cross section in laminar flow regime:

$$\Delta p = \frac{8\eta LQ}{\pi R^4} = \frac{8\pi\eta LQ}{A^2} \tag{2.15}$$

where η is the dynamic viscosity of the fluid, A is the cross section of the tube.

Description of Poiseuille flow in the Hele-Shaw cell is a variant of the equation above, is written as:

$$Q = -\frac{dp}{dx}\frac{b^3}{12\eta} \tag{2.16}$$

This expression is also referred to as Darcy's law, with permeability $k = b^2/12$ for the gap thickness b between the two parallel plates of a Hele-Shaw cell.

2.3.3 Fluidization of frictional fluids

In the mixture of granular materials and fluid, friction plays a vital role during the invasion process of another fluid. Such granular-fluid mixtures were referred to as 'frictional fluids' in [27]. At low invasion rate before the fluid viscosity has the effect on the displacement, particles within the friction fluid will accumulate and finally have jammed front formed as mentioned in the last section, friction dominates the process.

At high invasion rate, however, viscous forces become non-negligible. The drag force provided by the friction between fluid and particles is larger than the friction of the granular bed, the granular bed is thereby fluidized [27, 28]. In other words, the fluid pressure gradient ∇P is larger than the gravitational friction of the granular bed:

$$\mid \nabla P \mid > \mu \rho_e g \tag{2.17}$$

where μ is the friction coefficient, $\Delta\rho$ is the density contrast between the grains and the hosting fluid in the granular packing.

According to Darcy's equation, the pressure gradient ∇P of the fluid through the packing can be written as:

$$\mid \nabla P \mid = \frac{\eta Q}{kA} \tag{2.18}$$

Combining Eq. 2.17 and Eq. 2.18, the prediction for critical fluidization flow rate Q_f can be written as:

$$Q_f = \frac{\mu \rho_e g k A}{\eta} \tag{2.19}$$

In [28], the authors proposed a dimensionless number F, the fluidization number to make the prediction model more general:

$$F = \frac{q\eta}{\mu \rho_e g k} \tag{2.20}$$

For $F > 1$ the bed is thought to be fluidized.

2.4 Physics on the interface

2.4.1 Surface tension and Young-Laplace Equation

Surface energy and surface tension are different expressions for the same mechanism: how strongly molecules are attracted to each other. However, surface energy is normally referred to the cases in solids and surface tension applies to liquids.

The molecules on the liquid surfaces attract each other which contributes to the surface tension, the surfaces tends to shrink into the minimum surface area. The most common phenomenon is water droplet. At a water-air interface, the attraction between water molecules themselves (cohesion) is greater than the attraction of water molecules to air molecules (adhesion), so water tends to shrink to a droplet to form a minimum surface area.

Surface tension provides an elastic force that resist the stretching of an interface between two immiscible fluids. If there is no pressure difference between the fluids, the interface remains flat. The surface tension generates a 'capillary' pressure Δp that is proportional to the curvature as described by the Young-Laplace equation:

$$\Delta p = -\gamma \left(\frac{1}{R_1} + \frac{1}{R_2} \right) \tag{2.21}$$

where γ is the surface tension, R_1 and R_2 are the principle radii of curvature (shown in Figure 2.3).

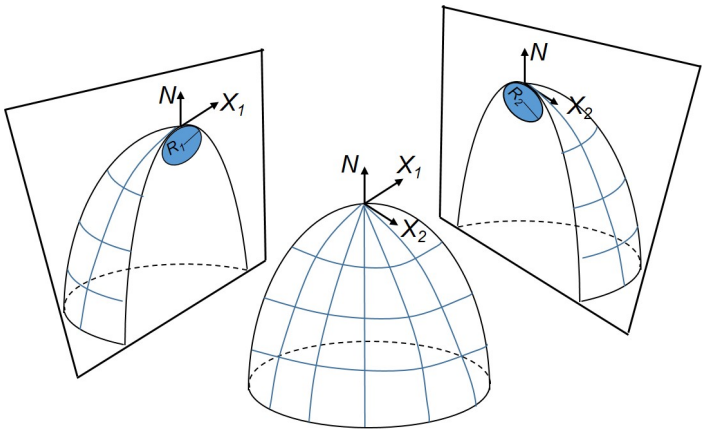

Fig. 2.3 Schematic of the principle radii of curvature R_1 and R_2 at two directions X_1 and X_2 respectively. X_1 and X_2 are perpendicular to each other, and are both vertical to the normal N.

2.4.2 Wettability and contact angle

Wettability is the ability of a liquid to maintain contact with the surface of a solid, this ability in principle is also related to the inter-molecule attraction and surface energy. If the adhesive forces between the liquid molecules are larger than the cohesive forces between liquid and solid molecules, the liquid is non-wetting to the solid, otherwise the liquid is wetting to the solid.

Wettability is quantified by the contact angle θ which can be directly measured on the gas-liquid-solid interface. The Young equation describes a thermodynamic equilibrium between interfacial energies and can be used to calculated the contact angle:

$$\gamma_{SG} - \gamma_{SL} - \gamma_{LG} cos\theta = 0 \tag{2.22}$$

where γ_{SG} is the solid-gas interfacial energy, γ_{SL} the solid-liquid interfacial energy, γ_{LG} the liquid-gas interfacial energy as shown in Figure 2.4.

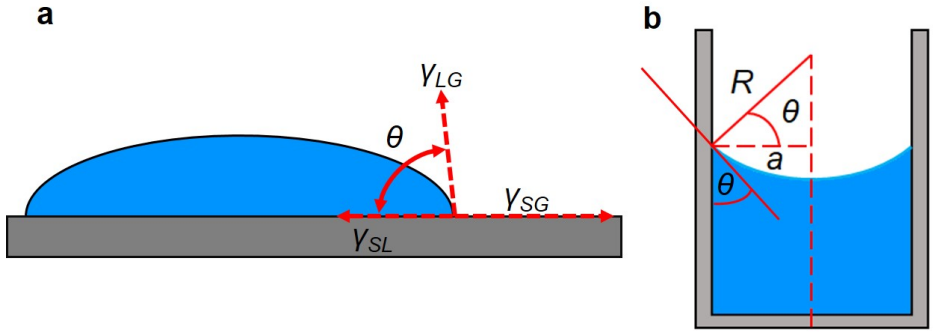

Fig. 2.4 Contact angle θ of gas-liquid-solid interface. (a) A liquid droplet rests on the surface of a solid surface. (b) The meniscus of a liquid which is wetting to the tube.

2.4.3 Cassie-Baxter state and surface treatment

In a gas-liquid-solid system, aqueous solution is the most commonly used liquid. If the contact angle in this system is larger than 90° the solid surface is regarded as hydrophobic, while at contact angle smaller than 90° the solid surface is hydrophilic. The solids used in the experiment are usually made of the materials that are naturally hydrophilic, glass for instance. A surface treatment is often required to generate hydrophobic surfaces on materials that are otherwise naturally hydrophilic.

The roughness of a solid surface significantly effects the contact angle [75]. Robert Wenzel in 1936 developed a model (Figure 2.5) by modifying Young's equation to calculate the contact angle θ for homogeneous surfaces:

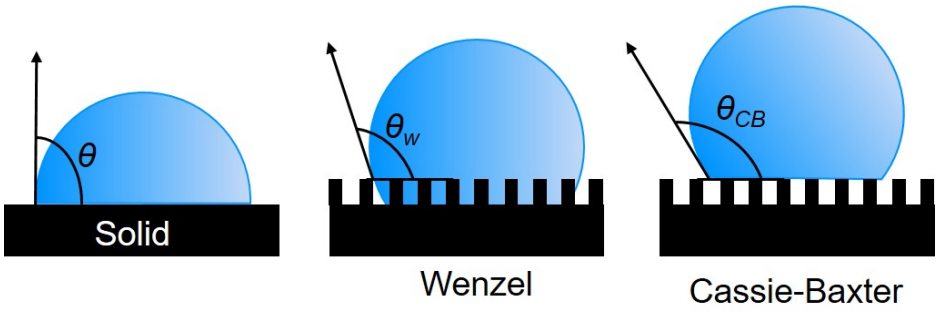

Fig. 2.5 Different contact angle scenarios : liquid state on smooth solid surface, Wenzel state and Cassie-Baxter state.

$$\cos\theta^* = r\cos\theta \tag{2.23}$$

where θ^* is the apparent contact angle, r is the roughness ratio.

Later in 1944, Cassie and Baxter extended the results to heterogeneous surfaces (Figure 2.5):

$$\cos\theta = \sum_{k=1}^{N} A_k \cos\theta_k, \quad \text{with} \sum_{k=1}^{N} A_k = 1 \tag{2.24}$$

where A_k is the surface area of k_{th} type of composite material (with contact angle θ_k) of the whole surface.

There are normally two ways of hydrophobic treatment according to the principles above. One is directly altering the solid surface in microscopic scale using the methods such as laser pulses [135] and UV radiation [59]. Another is surface coating by applying materials such as manganese oxide polystyrene nano-composite, precipitated calcium carbonate, silica nano-coating, etc., on the solid surface to form a thin layer that repels aqueous solutions. Among these materials, silica-based coatings are the most cost effective [136] and will be used in the current thesis.

Chapter 3

Frictional fluid instabilities shaped by viscous forces

3.1 Introduction

Viscous fingering, or the Saffman-Taylor instability [137, 25], is a classic example of unstable flow: A low-viscosity fluid pushes away a high-viscosity fluid in a flow cell. Any bulge on the interface steepens the pressure gradient inside the high-viscosity fluid, and the growth accelerates such that a fingering pattern evolves where the most advanced tips grow at the expense of the fluid falling behind [138, 139].

Whether or not viscous fingering is observed depends on two dimensionless numbers: the mobility ratio $\mathcal{M}$. Here we define $\mathcal{M}$ as the log of the viscosity ratio between the two fluids, $\mathcal{M} = \log(\eta_{\text{def}}/\eta_{\text{inv}})$, where η_{inv} is the viscosity of the invading phase and η_{def} that of the defending phase. If $\mathcal{M}$ is negative ($-\mathcal{M}$), the higher viscosity in the invading fluid acts to stabilise the interface, leading to compact displacement (e.g. a growing circular invaded region if fluid is injected from a central point). Unstable viscous fingering is observed for flows when $\mathcal{M}$ is positive ($+\mathcal{M}$). Here the stabilising effect of surface tension is in competition with the destabilising effect of viscosity.

Unstable flows involving granular suspensions and granular material sedimented in the defending fluid have been shown to produce a wide variety of flow patterns [27, 140], including viscous fingering in suspensions [141, 31, 39], frictional fingering [24, 27, 26], channeling [29, 37, 38, 41, 42, 80–82] and capillary fracturing [142, 32, 33, 143, 34–36, 28]. The introduction of granular material adds solid friction – between grains, and between grains and confining surfaces – as a governing force in the dynamics.

The wetting controls the capillary forces imposed by the meniscus on the grains. Here we define wettability $\mathrm{W} = -\cos\theta$ by the contact angle θ inside the invading fluid against the solid material. Negative W ($-$W), where the granular bed is wetted by the invading fluid, results in spontaneous imbibition, whereas $+$W results in the granular bed resisting penetration by the invading fluid (drainage). We quantify the balance of viscous forces, which drive the motion of the grains, to friction, which resists the motion of the grains, via a dimensionless 'viscous deformability' D_{visc}:

$$D_{\mathrm{visc}} = \frac{\eta_{\mathrm{max}} u/d}{G}, \tag{3.1}$$

where $u = Q/2Rb$, and where we use the grain diameter d as the relevant viscous length scale. The frictional strength of the granular layer is $G = \mu\rho_b g b\varphi$, where μ is the friction coefficient between the grains and the plate, g is the body force per unit mass due to gravity, and $\rho_b = (\rho_g - \rho_{\mathrm{def}})(1-n)$ is the bulk density difference between the granular layer and the defending fluid, where n is the porosity of the packing. In current study, the density of the grains is 2.5 g/cm^3 and the density of the defending fluid, air, is negligible, here ρ_b = 2.5 g/cm^3. There is no one well-defined velocity that applies to all the fingers in an experiment, so we must choose a characteristic velocity that is representative for the experiment as a whole. We choose to use $u = Q/A_{\mathrm{cross}} = Q/(bw_c)$ where w_c = 1 cm is a "typical" finger width which is close to the finger width in each experiment.

Our D_{visc} is analogous to the large capillary number Ca limit of the 'fracturing number' from [36], where the motion of a granular solid is resisted by friction under confining stress, and to the 'viscous fracturing number' [148], where the motion of a porous viscoplastic solid is resisted by a yield stress. The ratio of viscous to frictional forces was referred to as a 'fluidisation number' by [28].

Most of the previous work on displacement patterns in confined granular suspensions has focused on viscously unstable flows ($+\mathcal{M}$) in drainage ($+$W) (e.g. [31, 27, 36, 140]). One exception is Huang et al. [29] who investigated viscously stable displacement ($-\mathcal{M}$) of a dry granular packing by injecting aqueous glycerol solutions into dry sand. As such, the wetting condition was imbibition ($-$W) where the invading fluid penetrated the pore space of the granular packing. In this section we study the viscously stable ($-\mathcal{M}$) frictional flow patterns in drainage ($+$W) (Figure 3.1). Viscously stable frictional fingering was achieved by injecting water into dry layers of silanized hydrophobic glass beads. In this case air is the (low viscosity) defending fluid in which the grains are "submerged". By varying Q over a wide range and also varying filling level φ, we observe how the shifting balance between viscous forces, friction and surface tension influences the pattern of invasion in

a negative $\mathcal{M}$ fingering system. Experiments are supported by a theoretical model and numerical simulations.

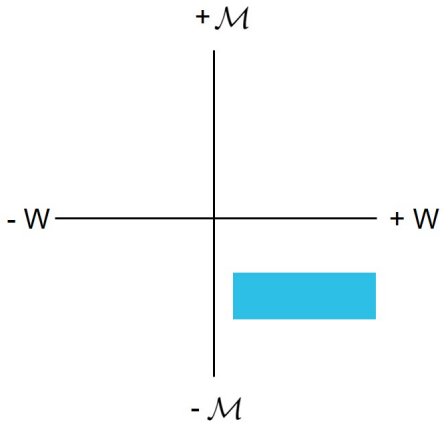

Fig. 3.1 The quadrant with blue square in the diagram of viscosity ratio $\mathcal{M}$ and wettability W is the study focus of Chapter 3.

3.2 Methodology

3.2.1 Experimental setup and materials

Our Hele-Shaw cell comprised two 40×40×1.5 cm glass plates. A 6 mm diameter hole was drilled through the centre of the top plate to provide an inlet. The internal surfaces of the plates were silanized to avoid exposing a strongly hydrophilic surface which aids aqueous solution invasion and preventing aqueous solution travelling along the headspace of the cell. Our silanization protocol followed the method outlined in [144]. The silanization solution used here is a mixture of Trimethoxy(octadecyl)silane (OTMS), and Isopropyl alcohol(IPA) with a ratio of 1:100.

The silanization process was as follows: 1) mix the OTMS and IPA together with the ratio mentioned above; 2) the pH of the solution was adjusted to 3 by adding the diluted Sulfuric acid (H_2SO_4, 0.1 M) to promote the hydrolysis of OTMS; 3) the solution was strongly stirred using magnetic stirrer for at least 60 minutes at room temperature to form a alkylsilanol solution; 4) pour some of the reacted solution on the surface of a glass plate and wipe it several times to make the coating uniform; 5) dry the glass plate and we would get a surface with the contact angle of 120 degrees. Note that all the procedures were performed in fume hood to avoid any potential hazards.

Hydrophobic grains were produced by silanizing glass beads (Honite 18). All the glass beads used were cleaned by the following steps: first, glass beads were immersed into Hydrochloric acid (HCL, 0.1 M) and strongly stirred using magnetic stirrer for at least one hour. Then, they were rinsed thoroughly with deionized water. Finally, the cleaned beads were funnelled into a glass pan and oven dried at 80 degrees celsius.

The dried beads were then sieved to diameter 75–100 μm. The silanization solution preparation processes were the same as the procedures mentioned above when coating the surface of the glass plates. The sieved beads were immersed into the silanization solution in a beaker and heated on a hotplate to accelerate the evaporation of the solution. The coated hydrophobic beads were sieved again to get rid of the lumps in the beads.

The Hele-Shaw experiments were prepared by first spreading a layer of the hydrophobic beads on the bottom plate of the cell. In order to achieve a layer of uniform thickness, two strips of adhesive tape were placed along opposite sides of the bottom plate, and a straight-edged tool resting on both tape strips was used to scrape the granular material along the plate. In the first two parts of the results section, the top plate was then put in place, separated from the bottom plate with 0.9 mm spacers, which were slightly higher than the strips of tape so as to produce a granular bed with $\varphi < 1$. We varied the packing height by changing the thickness of the tapes and thereby varying φ. The cell was clamped together firmly after assembly to prevent the top plate from lifting. All four edges of the cell were left open to the atmosphere.

Stated values of φ were inferred from experimental images, which was considered more accurate than estimating φ from the thickness of the tapes and spacers. If an experiment produced an area A_i which had been invaded and cleared of grains and also an area A_f which had been fully compacted, then conservation of mass dictates that $\varphi = A_f/(A_i + A_f)$.

The experiment was performed at injection rates between 0.3 and 200 mL/min, with φ between 0.42 and 0.70. The experiment was repeated for injection rates between 0.3 and 200 mL/min, with φ between 0.42 and 0.70. $\mathcal{M}$ was calculated to be -3.9; W was sufficiently high that no penetration of water inside the hydrophobic packing was observed.

We injected water into the cell using a syringe pump (Harvard Scientific, PHD Ultra). The cell was backlit, such that invaded regions appear bright and compacted regions dark (Figure 3.2). Results were recorded using a Nikon 1 J2 digital camera at 30 frames per second.

3.2.2 Numerical method

We have performed the numerical simulations of the system using code previously used to model air invasion into a wet hydrophilic packing [129, 26], adapted to include viscous pres-

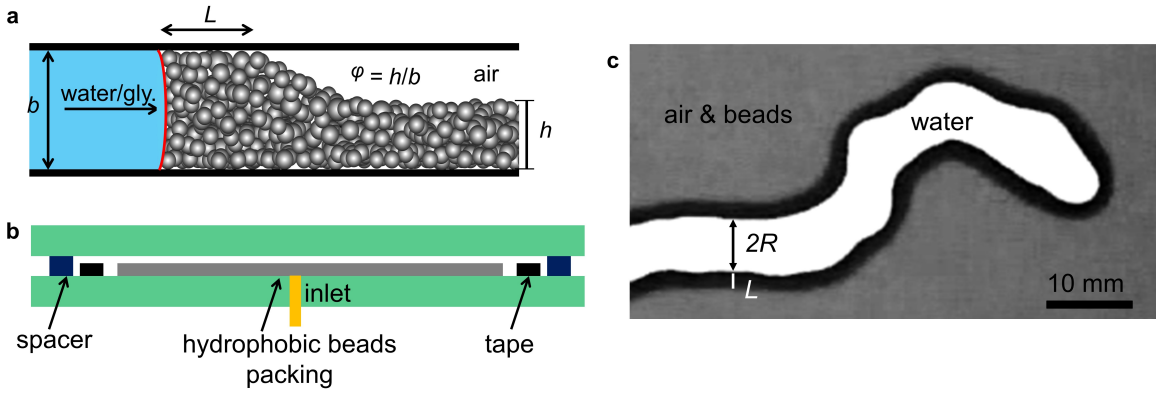

Fig. 3.2 (a) Schematic side view of an invading fluid interface. Water bulldozes the hydrophobic grains, forming a compaction front of width L. (b) Schematic cross-section of the Hele-Shaw cell. The thickness of the tape is smaller than that of the spacer, producing a granular bed with $\varphi < 1$. (c) Photographic top view of an invading finger. The white region has been invaded with water and cleared of grains, while the black region (the compaction front) has been completely filled with grains. Fingers are characterised by their tip radius R and their compaction front width L.

sure. The code including the viscous pressure is developed by my colleague James Campbell and my contribution is the calibration of the simulation according to the experimental results (more details can be found in A). As shown in Figure3.3, this code uses a chain of nodes which contain the coordinate information, to represent the interface of the invading fluid. The granular packing is discretized into grid cell, using a two-dimensional array of values, $f_{m,n}$, to represent the normalized filling fraction φ in the cell at each point in space where φ is equal to 1 in compaction front and less than 1 in undisturbed region.

For every mobile node, a *link* with a length L_i which represents the shortest distance between the current node i and the center of the linked cell where $f_{m,n}$ changes just from 1 to less than 1, is identified. A criterion to decide the moment of node stagnation is defined using a quarter-circle region with the radius of maximum cutoff length $L_{\max}$. If there is no link establishment within these the candidate cells, the node is regarded as stagnant. $L_{\max}$ in practice is set to be larger than the maximum compaction front width in experiment, say 1.5 cm here.

The node separation length ξ_{node} and the grid separation length ξ_{grid} must be much smaller than the finger width, and the smaller values lead to a better simulation results but higher time cost. Considering both effects, $\xi_{\text{node}} = 0.03$ cm and $\xi_{\text{grid}} = 0.025$ cm are set in the simulation.

The radius of curvature or half of the finger width R in the simulation is represented by B-spline approximation of the interface [129, 145]. To simulate the effects of the viscosity,

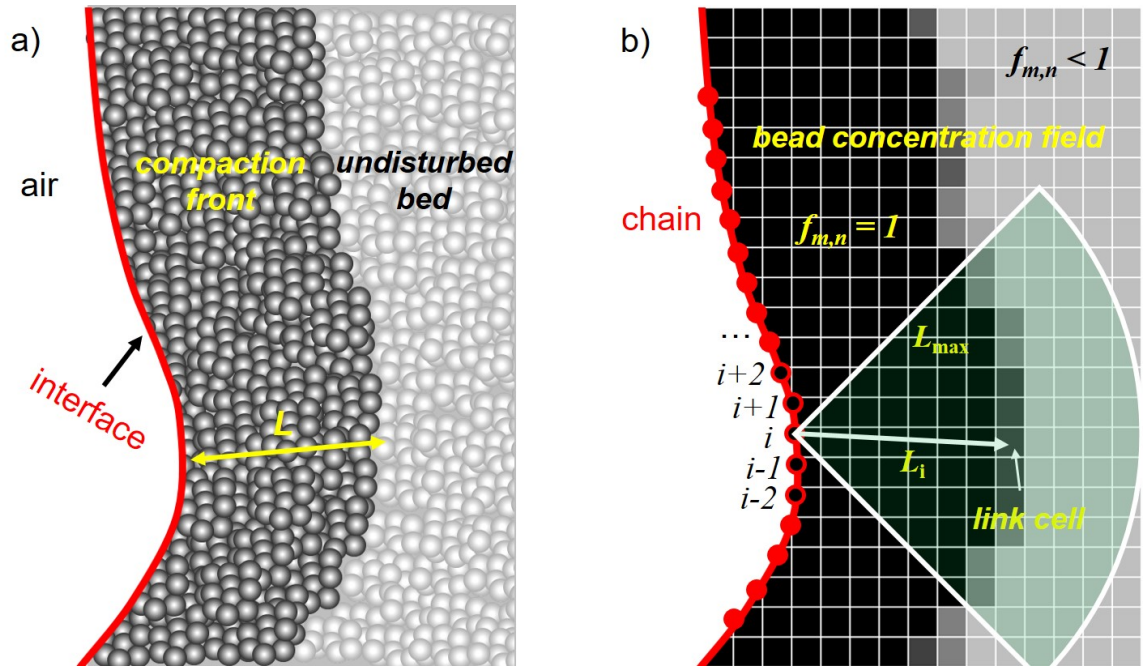

Fig. 3.3 Illustration of the discretization procedure of the bulldozed granular packing [129]. The interface is discretized to a chain of nodes with a separation ξ_{node}, the beads packing is discretized to grid cell, using a two-dimensional array of values, $f_{m,n}$, to represent the normalized filling fraction φ in the cell at each point in space where φ is equal to 1 in compaction front and less than 1 in undisturbed region. L_i is the shortest distance between the current node i and the center of the linked cell where $f_{m,n}$ changes just from 1 to less than 1. $L_{\max}$ is the radius of the quarter-circle region to limit the candidate cells. The size of the granular beads and grid cells are exaggerated for description, and size of the granular beads in the experiment is much smaller than the size of the grid cell.

the viscous pressure is added in Equation 3.2. Every timestep the threshold pressure P_t is calculated for every interface node, following

$$P_t = \frac{\gamma}{r} + \sigma + P_v \tag{3.2}$$

where r is the interface radius of curvature, σ is frictional stress resisting motion and P_v is the viscous pressure difference between that point and the inlet. σ is expressed as in Equation 2.10, with L being the distance to the nearest point on the array which is not yet fully filled, i.e., L_i. The static friction coefficient is used, with the kinetic friction coefficient being substituted in the exponent if the interface node has moved in the previous 500 cycles.

The viscous pressure difference P_v between each point and the inlet is calculated each timestep on a simplified version of the finger pattern, reduced to a branching tree of nodes as illustrated in Figure 3.7. This tree grows dynamically during the simulation to closely mimic

the shape of the invasion pattern, with each interface node reading P_v from its nearest node on this tree. Each node on the tree calculates P_v according to the Hagen-Poiseuille equation as

$$P_v = P_v' + \frac{6\eta Q_f X}{Rb^3} \tag{3.3}$$

where P_v' is the P_v of its parent node, η is the viscosity, Q_f is the flow rate into the finger downstream averaged over the last 250 timesteps, X is the distance to its parent node and R is the average half-width of the finger between itself and its parent node. The 250 timestep period for averaging viscosity and the 500 timestep period for transitioning from kinetic to static friction are arbitrary numbers. They were chosen for being large compared to the typical number of growing fingers (to avoid excessive discretisation of viscous pressure and to prevent slower-moving but still active fingers from taking on static friction), but still small compared to the typical time period of an entire simulation. Qualitative tests did not suggest that the fingering patterns were strongly sensitive to these parameters.

Once the node with the lowest P_t is identified, it is advanced forward slightly, along with its three nearest neighbours on each side to maintain a smooth interface. New nodes are introduced as needed as the interface lengthens. Granular material from the invaded region is redistributed to the nearest positions which have space available. Randomness is introduced by initialising the distribution of granular material with random fluctuations above and below φ. The beads concentration field is set to be circular and has the same size as the experiment, i.e., diameter of 26.8 cm. The simulation will stop once the finger reaches the boundary.

3.3 Results and discussion

In all cases we saw a fingering pattern of invasion, with water bulldozing granular material ahead of it, producing discrete fingers of water with well-defined characteristic width and a front of compacted grains surrounding them (Figure 3.2). Fingers grew only at their tips and generally did not widen after their initial formation. Figure 3.4 shows a selection of experimental results.

Changing φ affected the width of fingers: at the same injection rate, a higher φ led to a smaller R, due to a thick compaction front accumulating after relatively little advance of the interface. This trend was also seen in previous studies with air invasion, although in that case analogous conditions could also produce a discontinuous “bubble” invasion pattern if a large injection volume of gas was used [24, 27]. These bubble invasion patterns are thought to be a consequence of the compressibility of the gas, and their absence in our system is likely a consequence of the incompressibility of the invading fluid.

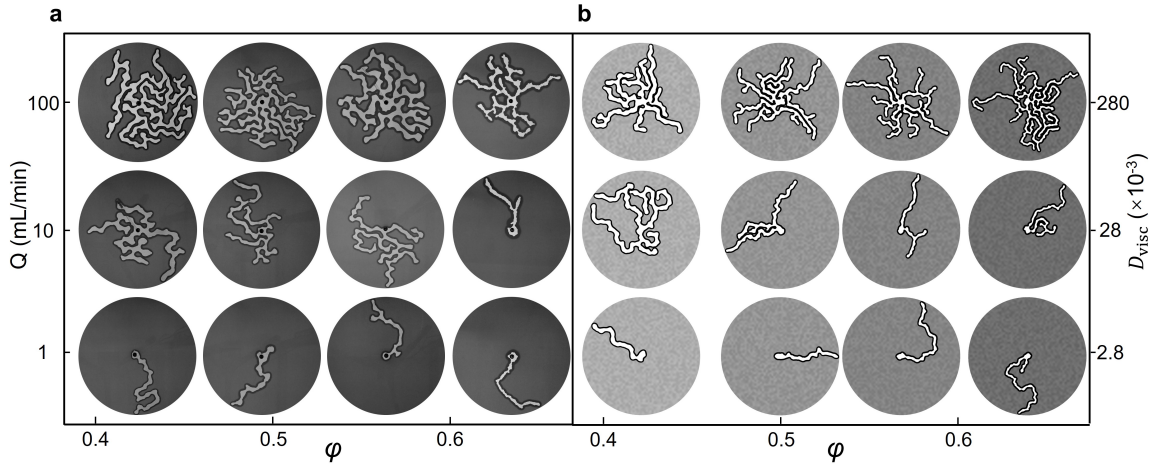

Fig. 3.4 Phase diagram of invasion patterns at different φ and D_{visc}. (a) experiment and (b) simulation. Water (bright fingering structure) invades from a central inlet, displacing a layer of hydrophobic material (dark gray). All images are cropped to a circle representing the moment the first finger reached a radius of 13.4 cm. Each disc has a diameter of 26.8 cm.

At very low injection rates, when the D_{visc} is small, it may be assumed that viscous effects are insignificant [128], and the pattern is determined exclusively by friction and capillary pressure. We vary our injection rate Q over nearly three orders of magnitude to observe both this viscosity-independent regime, which we term the frictional regime, and also the regime at higher values of Q when viscous pressure gradients become significant. In the frictional regime (10 mL/min and below, or $D_{\text{visc}} = 2.8 \times 10^{-2}$ and below), there is just one finger advancing at a time. As we increase Q to 30 ml/min ($D_{\text{visc}} = 8.3 \times 10^{-2}$) or above, we see two or more fingers advancing simultaneously.

We here divide the discussion into three parts. First, we consider the frictional regime, where only frictional forces and surface tension are important. Secondly, we consider the role played by viscous forces within the fingers and use this to explain the simultaneous growth of fingers at higher injection rates. Finally, the simulation results are matched with the experimental results and theoretical analyses.

3.3.1 Frictional regime

At low values of D_{visc} there are only two forces of significance: surface tension and friction [128, 27]. The invading water does not have enough pressure to invade between the grains of the hydrophobic packing, and therefore invades the cell by bulldozing the packing before it, forming a finger with an approximately semicircular tip of radius R, and an approximately constant width $2R$ behind the tip. The finger is prevented from widening by

a compacted front of grains of approximately constant thickness L, which can hold back a stress up to σ by frictional action with the top and bottom plates via force chains within the packing. We can express the threshold pressure difference P_t across the finger tip for a finger to be able to grow as the sum of the frictional stress σ to push forwards the compacted front and the capillary pressure, such that [24]:

$$P_t = \sigma + \Delta p_{\text{cap}}. \tag{3.4}$$

Capillary pressure

As introduced in Chapter 2, there is a capillary pressure difference across the interface of two fluids which is described by Young-Laplace equation, and in the current case can be written as:

$$\Delta p = \gamma \left(\frac{2cos\theta}{b} + \frac{1}{R} \right) \tag{3.5}$$

where γ is the surface tension, $2cos\theta/b$ is out-of-plane curvature, θ is contact angle, $1/R$ is the in-plane curvature (here is the radius R of finger tip).

We only need to consider the in-plane radius of curvature because the out-of-plane curvature between the two plates of Hele-Shaw cell is assumed to be constant throughout the system, and therefore would only lead to a constant contribution to P_t which would have no effect on the system dynamics. The in-plane radius of curvature is equal to the radius R of finger tip, the capillary pressure that affects the finger formation thus can be written as:

$$\Delta p_{\text{cap}} = \frac{\gamma}{R} \tag{3.6}$$

Frictional stress

Frictional stress σ during the capillary bulldozing in the system is caused by the force networks in granular materials, and the description models for it has been described in Chapter 2. For simplication, we here use the linear approximation for the frictional stress:

$$\sigma = \sigma_0 \frac{L}{b} \tag{3.7}$$

where b is the plate spacing and σ_0 is fit to experimental results. Here and throughout the paper we shall make the approximation that the finger width equals $2R$, or twice the tip radius of curvature. If we also assume that the front width L is approximately constant, then

conservation of mass dictates that

$$L = R\frac{\varphi}{1-\varphi}. \tag{3.8}$$

Prediction model for *R*

Combining equations 3.4, 3.7 and 3.8, we find that P_t can be written as

$$P_t = \sigma_0 \frac{R}{b}\frac{\varphi}{1-\varphi} + \frac{\gamma}{R}. \tag{3.9}$$

A finger propagating with a higher R would have a lower capillary pressure inside the finger, but also a higher front thickness L and therefore a higher frictional stress σ. There exists a value of R at which P_t is minimum (and therefore the rate of work done is minimum), which we can find by differentiating P_t with respect to R:

$$\frac{\partial P_t}{\partial R} = -\frac{\gamma}{R^2} + \frac{\sigma_0}{b}\frac{\varphi}{1-\varphi} = 0 \tag{3.10}$$

which can be reduced to

$$R = \sqrt{\frac{\gamma b(1-\varphi)}{\sigma_0 \varphi}}. \tag{3.11}$$

We plot R as a function of volume fraction φ in Figure 3.5 for low injection rate experiments only. There is a strong match between the experimental data and the theoretical curve, in common with previous research on air-invasion labyrinths [24, 26]. Therefore we conclude that behaviour at low D_{visc} may be well described without reference to viscous effects, both for positive and negative $\mathcal{M}$, with finger growth dynamics being determined exclusively by competition between capillary and frictional forces at the tip without any significant influence of longer-range forces or pressure gradients.

3.3.2 From single-fingering to multi-fingering

As we increase the injection rate Q, and hence D_{visc}, over two orders of magnitude, we observe a transition away from this viscosity-independent regime at low D_{visc}, which we term the frictional regime, toward a regime where viscous pressure gradients become significant. As Q increases, the number of simultaneously growing fingers increases monotonically from one in the frictional regime to nearly 20 at the highest values of Q explored here (Figs. 3.4 and 3.6).

The low-D_{visc} and high-D_{visc} are compared in Figure 3.6 a and b, where the invading-fluid-filled fingers are colourised by invasion time. Low D_{visc} gives incremental growth

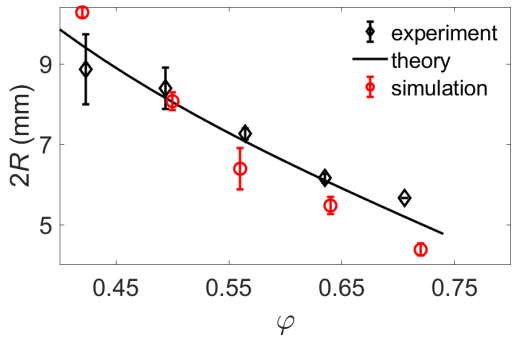

Fig. 3.5 Finger width $2R$ decreasing with increasing filling fraction φ. Black diamonds represent experimental results (mean and standard deviation of three experiments), while red circles represent simulation results (mean and standard deviation of three simulations); in both cases $2R$ is measured as the ratio between total invaded area and interface length. The solid line is the prediction of Equation 3.11 and $\sigma_0 = 4$.

localised at the tip of a single finger into which all the injected fluid flows. Branching is sometimes observed, however usually only one finger is actively growing at any one time. At high D_{visc}, several fingers grow simultaneously. New fingers sprout by side-branching, and the injected fluid flows through the network of fingers to the active tips indicated by rough axisymmetry of the colors in Figure 3.6 b.

For $-\mathcal{M}$, the viscous pressure gradient is located within the invading fluid, decreasing along the fingers from the inlet towards the active tips. Higher pressures further behind the growing tips increase the tendency for new fingers to break out from the walls of the old, favouring growth in the central parts of the pattern. This is the viscous stabilisation mechanism of flows at $-\mathcal{M}$. The frictional instability competes with viscous stabilization, favouring continued growth at the curved tip of the finger over displacement of the side walls. Two mechanisms also tend to suppress finger branching from a static side wall compared to the growing finger tip: (1) the geometrical factor accounting for the higher stress required to deform a flat compaction front compared to pushing forward an already curved tip [146] and (2) the frictional strength of the side walls may be higher on account of a higher solid-solid static friction coefficient μ_s compared to the dynamic friction coefficient μ_d of the moving tip due to short-lived lubrication layers between grains and the confining plates.

We represent these effects by introducing a threshold pressure $P_b = P_t + \Delta P_b > P_t$ required to sprout a new finger branch behind the tip. The viscous pressure within a finger increases backward from the tip. At some distance Δr_b from the tip, the pressure will therefore reach P_b. Assuming the volume flux in each growing finger to be the same (Q/N), this distance

can be inferred from Darcy's law,

$$\Delta r_b = \frac{Rb^3 \Delta P_b}{6\eta Q} N. \tag{3.12}$$

During the injection of a volume ΔV, each finger receives a volume $\Delta V/N$, and will on the average sprout $\Delta N/N$ new fingers. When the injected volume in a finger equals $2Rb\Delta r_b$ a branch will be sprouted behind the tip, so the average increase in N is

$$\frac{\Delta N}{N} = \frac{\Delta V/N}{2Rb\Delta r_b}, \tag{3.13}$$

which with Eq. 3.12 yields

$$N\Delta N = \frac{3\eta Q \Delta V}{R^2 b^4 \Delta P_b}. \tag{3.14}$$

For large N, we approximate the discrete variation of ΔN by a continuous one, writing

$$dN^2 = \frac{6\eta Q}{R^2 b^4 \Delta P_b} dV, \tag{3.15}$$

which by integration from $V = 0$ gives

$$N(V) = \sqrt{\frac{6\eta Q V}{R^2 b^4 \Delta P_b}}. \tag{3.16}$$

Using the expression for R in Equation 3.11, we can then estimate the number of active fingers $N(V)$ and compare to experimental observations.

Figure 3.6 shows experimental data for N as a function of injected volume V for a range of injection rates compared with the predictions of Equation 3.16. The simple theory appears to give a surprisingly good estimate of the number of propagating fingers, despite possessing none of the geometrical complexity of the experimental patterns.

3.3.3 Numerical verification

Figure 3.4 b shows sample simulation results across a range of filling fractions and injection rates. Lower values of φ produced slightly wider fingers, as predicted by Equation 3.11 and as demonstrated by experiments. Finger width as a function of φ at Q = 1 mL/min is compared to experiment and theory in Figure 3.5.

Figure 3.4 also shows that the number of fingers increases with increasing injection rate, as it does in experiments. In order to investigate this effect in more detail a series of

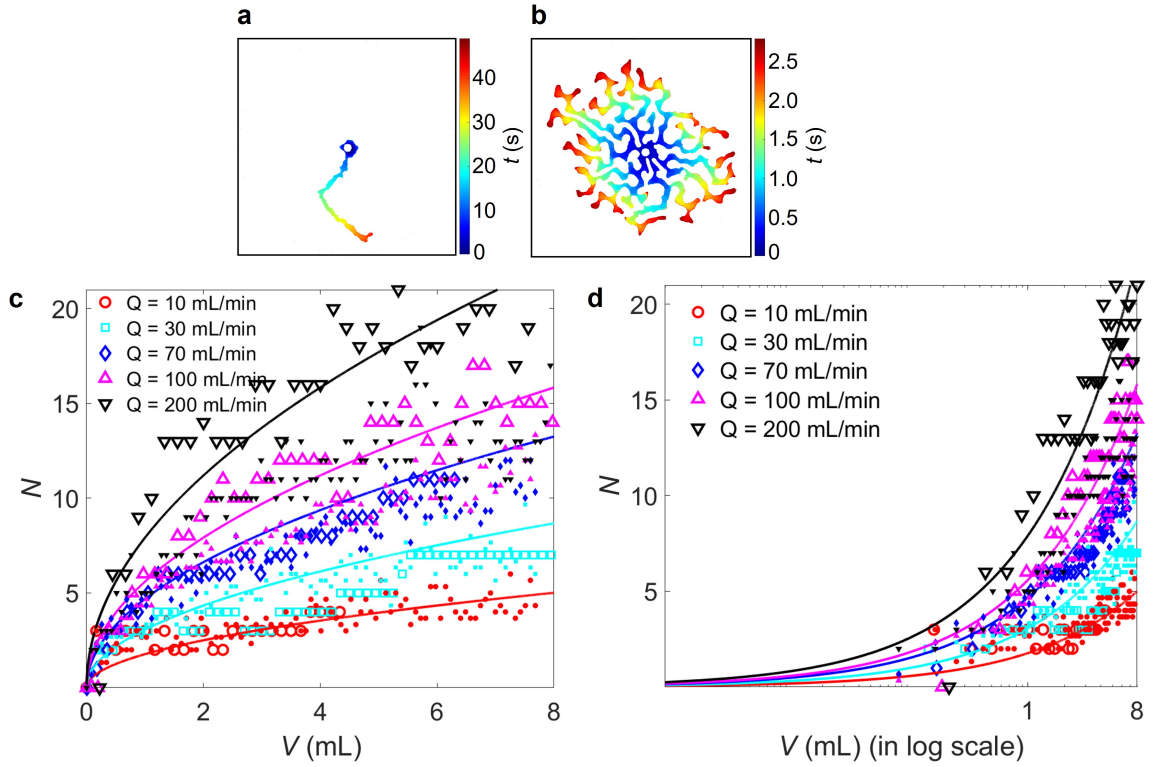

Fig. 3.6 Transition from a single finger to multiple fingers as Q increases. (a) Time evolution of a single finger ($Q = 1$ mL/min) and (b) multiple fingers (Q =200 mL/min) colourised according to invasion time t. (c) Count of simultaneously growing fingers N as a function of injected volume $V = Qt$ at different injection rates or D_{visc} for experiments (large open symbols), simulations (small filled symbols), and theory (solid lines). The theoretical lines are Equation 3.16 using $\Delta P_b = 30$ Pa as a fitting parameter. (d) is another version of $N - V$ plot while x-axis is set to be in log scale. In all panels, $\varphi = 0.56$.

simulations were performed in much larger cells, ten simulations at each of five different injection rates at $\varphi = 0.56$. The number of growing fingers in each 500-timestep period was counted and averaged across the 5 experiments, and the results are plotted in Figure 3.6 (c) and (d) alongside experimental and theoretical results. The numerical results show a good consistency to both experimental results and theoretical plot at $Q < 100$ mL/min. However, the simulation data start to deviate or more specifically smaller than the experimental data and theoretical line at $Q > 100$ mL/min. This might be caused by the inherent limitation of simulation itself.

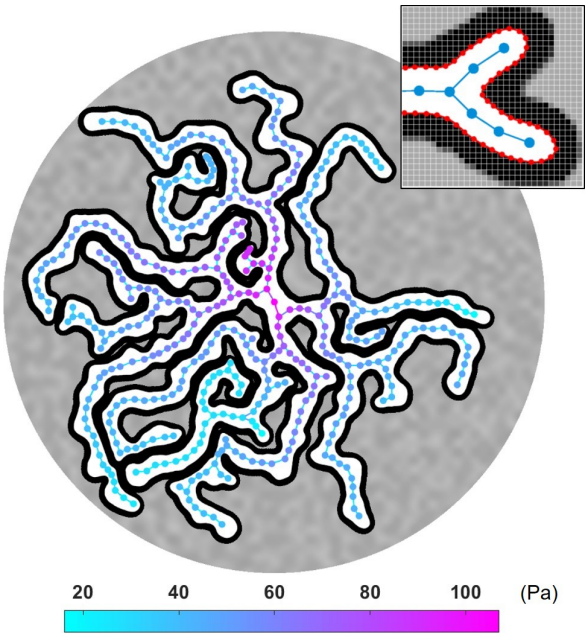

Fig. 3.7 Schematic illustration of the numerical simulation. The grey-black squares represent the filling level of the cell at each position, and the interface of the invading fluid is represented by a chain of nodes, here shown in red. Viscous pressure is calculated on a branching tree following the skeleton of the fingers, here shown in blue.

3.4 Conclusion

We have used experiment, simulation and theory to investigate a system in which liquid fingers invade a hydrophobic granular layer. Wider fingers are observed at lower granular filling fractions, in common with earlier experiments where fingers of air invaded a wet hydrophilic packing. A transition from single finger growth to multiple finger growth as we increase the injection rate, is observed, which has been demonstrated to be a consequence of viscous pressure gradients along the growing fingers. This study helps to fill an important gap in our knowledge of invasion patterns: understanding systems which produce complex patterns despite having an invading fluid of higher viscosity than the defending fluid. A firm grip on the fundamental effects of viscous pressure gradients is essential if we are to successfully extend our understanding to systems with high fluid invasion rates, far from quasi-static conditions.

Chapter 4

Viscous stabilization of frictional flow compared to viscously unstable displacements

4.1 Introduction

We have defined mobility ratio $\mathcal{M} = \log(\eta_{\text{def}}/\eta_{\text{inv}})$ to describe the viscosity difference between the two fluids in the system in Chapter 3. If $\mathcal{M} > 0$ the defending fluid has a higher viscosity, if $\mathcal{M} < 0$ the invading fluid has a higher viscosity. In the previous chapters, we have studied the situation when water invades the hydrophobic granular packing surrounded by air (-$\mathcal{M}$), the effect of increasing D_{visc} is to produce an increasing number of frictional fingers. The pattern is in effect becoming more compact because of the viscous stabilization effect that increases with higher injection rate. The pattern center of mass is roughly on the central injection point, as growth further away is discouraged by viscous dissipation within the fingers, however a large degree of randomness in finger growth direction still prevails.

In this chapter, we will study the situation of both $+\mathcal{M}$ and $-\mathcal{M}$ at $+$W (shown in Figure 4.1). We will study the pattern. formation when a liquid with higher viscosity than water invades the packing, the initial results are just the same scenario as in chapter 3, but at larger D_{visc}. The patterns become more compact and the finger growth becomes more directional in this case. In addition, we study the pattern formation in viscously unstable (+$\mathcal{M}$) invasion. A clear difference between the results of viscously stable (-$\mathcal{M}$) invasion and viscously unstable (+$\mathcal{M}$) is observed.

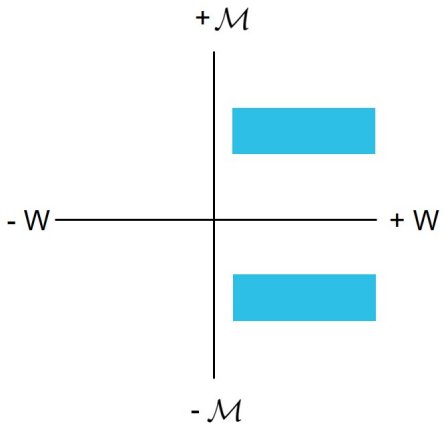

Fig. 4.1 The quadrant with blue square in the diagram of viscosity ratio $\mathcal{M}$ and wettability $\mathrm{W} = -\cos\theta$ is the study focus of Chapter 4.

4.2 Methodology

We use the same experimental setup, the same granular material and the same packing preparation method as in Chapter 3 when doing the viscously stable (-$\mathcal{M}$) invasion experiment. However, the viscosity of the invading fluid was varied in different experiments. Different viscosities were achieved by mixing glycerol and deionized water, with glycerol volume percentages of 0%, 58%, 84% and 100% corresponding to viscosities of 1, 14.1, 141.4 and 1414 mPa·s respectively [147]. The liquid was injected at rate between 3–100 mL/min.

The viscously unstable (+$\mathcal{M}$) experiments were performed in the similar cell as the (-$\mathcal{M}$) experiment except the surface of the plates remained hydrophilic. Figure 4.2 shows the setup difference between the two. The grains where acid-cleaned as described before (but not silanized), leaving them hydrophilic. A dispersion of the glass beads in the defending fluid (water/glycerol mixture with the viscosity of 14.14 and 141.4 mPa·s in different experiments) was loaded into the cell by fast injection, and subsequent sedimentation generated uniform granular layers corresponding to $\varphi = 0.5$. The invasion fluid (air) was injected at 0.1–100 mL/min using the syringe pump as described in Chapter 3.

4.3 Results and discussion

4.3.1 Viscous stabilization on frictional flow

Figure 4.3 shows the time evolution after water/glycerol mixture invading the dry hydrophobic granular packing. In addition to the increase of number of fingers N at higher Q as has been

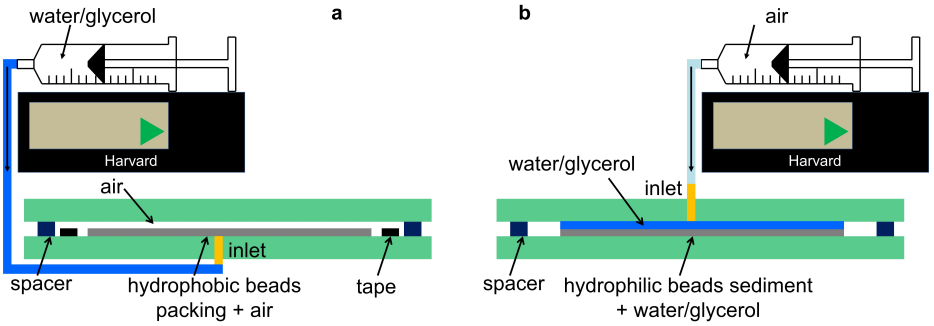

Fig. 4.2 Experimental setup used for viscously stable (-$\mathcal{M}$) and viscously unstable (+$\mathcal{M}$) invasion.

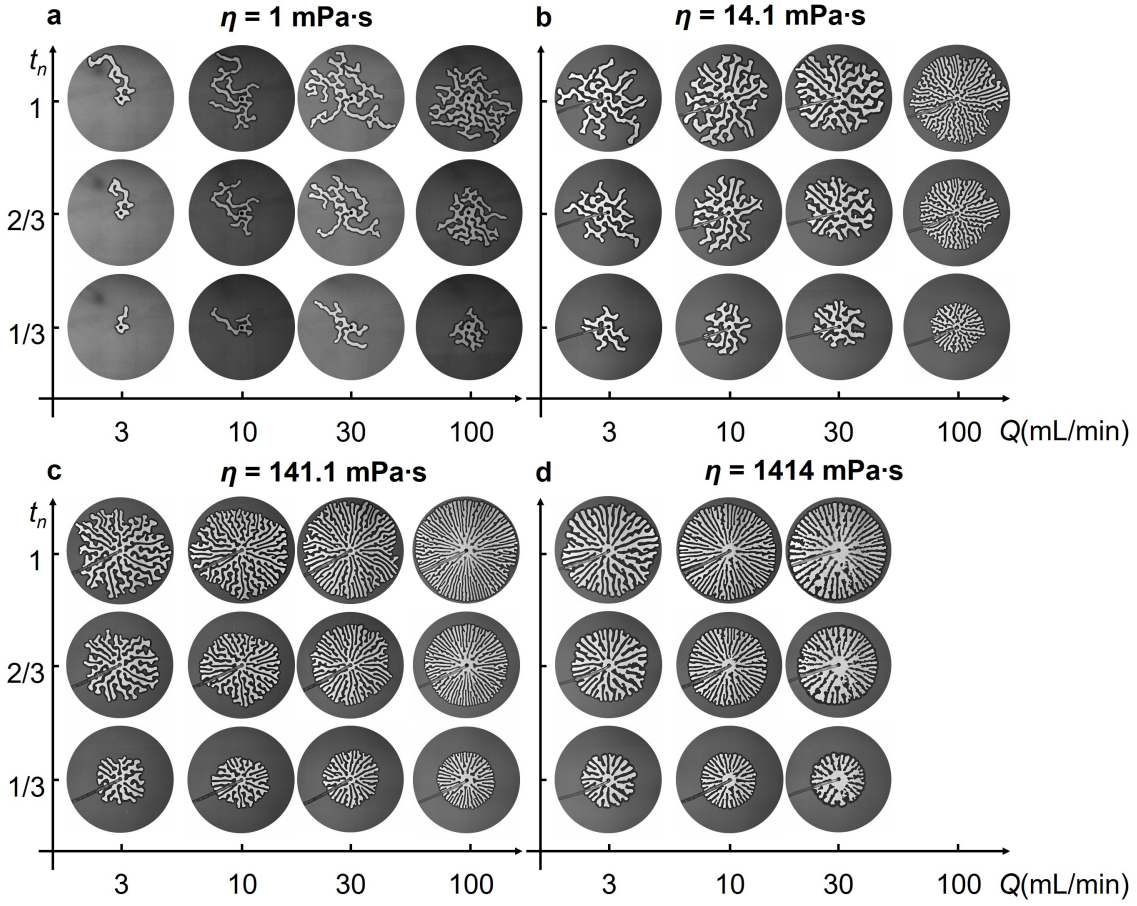

Fig. 4.3 Time evolution of experimental results of viscously stable (-$\mathcal{M}$) invasion at different injection rate Q and viscosity η. $t_n = t/t_{\text{all}}$ is a nornalized time where t is the real time over the period of pattern formation and t_{all} is the whole time of pattern formation within the experiment system. In all panels, φ=0.5, b=0.9 mm, and the disc diameter is 26.8 cm.

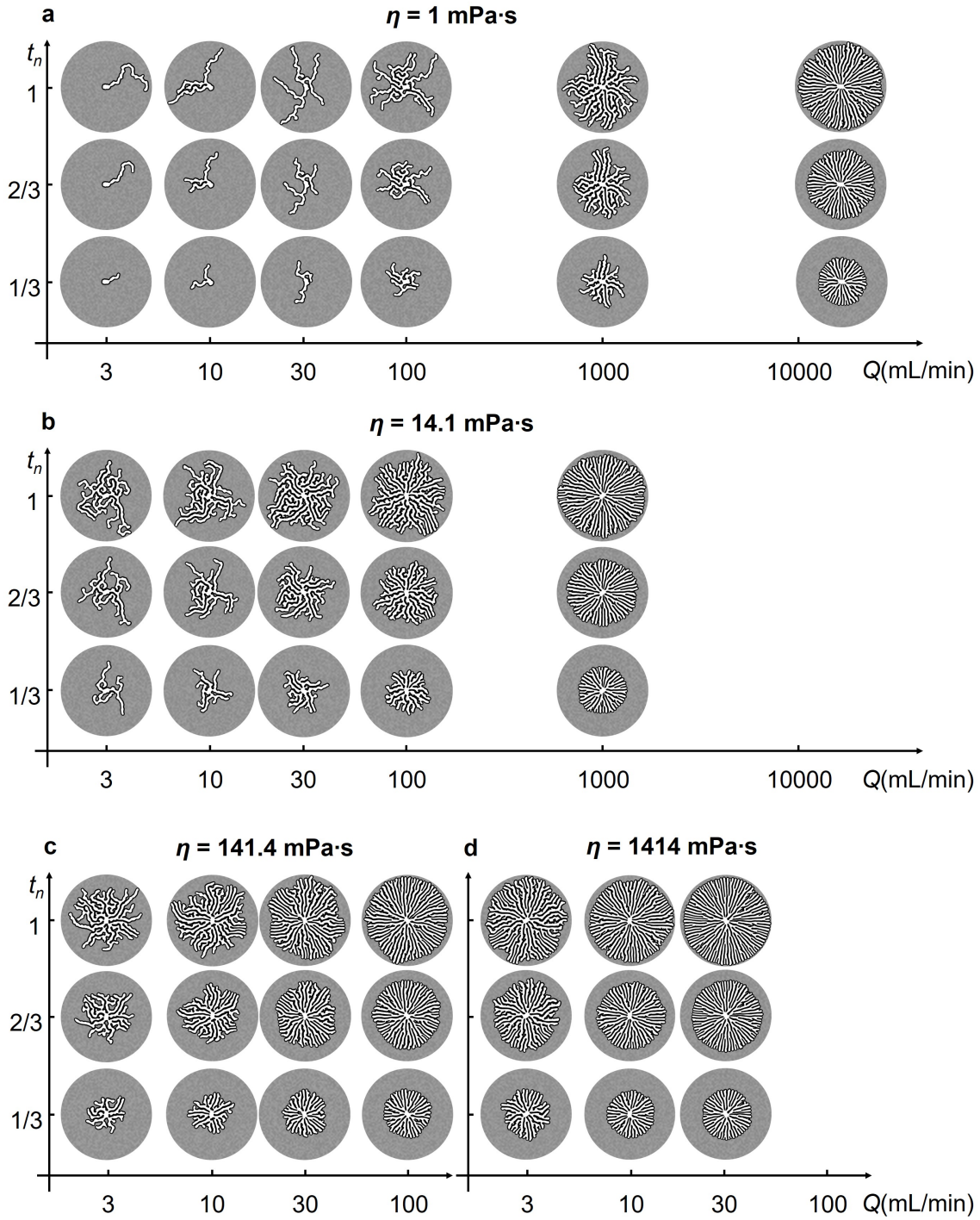

Fig. 4.4 Time evolution of experimental results of viscously stable (-$\mathcal{M}$) invasion at different injection rate Q and viscosity η. In all panels, φ=0.5, b=0.9 mm, and the disc diameter is 26.8 cm.

observed in Chapter 3, an increase of N at higher viscosity η of the invading fluid is observed. Corresponding simulation results are shown in Figure 4.4. The single frictional finger in Figure 4.3 occurs when viscous forces are insignificant and the frictional instability acts alone. The high viscosity of glycerol combined with the faster injection rate produces extreme viscous stabilization, where the pattern radiates outwards in an axisymmetric spoke pattern. Here, the frictional instability produces fingers and viscous stabilisation forces them to grow radially, with tips equidistant from the injection point, creating a circular displacement front with embedded radial streaks of packed grains. As the pattern expands over time, the fingers increase in number by splitting to populate the growing circumference while maintaining a constant characteristic finger width.

Figure 4.5 a shows an experimental η–Q phase diagram for viscously stable displacements, where the invading fluid is a mixture of water and glycerol and the defending grains are dry and hydrophobic. The viscosity of the invading fluid (*i.e.*, the fraction of glycerol) increases from bottom to top and Q increases from left to right. The top-right corner is empty because of the force limitation on the pump. Figure 4.5 b shows a corresponding η–Q phase diagram for the simulations over a wider range of Q. These phase diagrams illustrate that pattern formation in this system is governed by D_{visc}: Similar patterns fall on similar values for D_{visc}, along diagonal lines in the diagram.

In these phase diagrams, similar patterns fall along diagonal lines corresponding to constant values of the product $\eta_{\mathrm{inv}}Q$, which controls the strength of viscous forces. Viscous deformability D_{visc} as defined in Equation 3.1 in Chapter 3, is used to quantify the balance of viscous forces, which drive the motion of the grains, to friction, which resists the motion of the grains.

The critical viscous deformability for the transition from multiple fingers to radial spokes, D^{**}_{visc}, may be deduced from the theory presented in Equations 3.12 – 3.16. When the critical distance Δr_b becomes smaller than the finger width $2R$, branching will be suppressed by the presence of neighboring fingers as the pattern becomes space-filling. These patterns are then viscously stabilized in the sense that a finger that advances slightly ahead of its neighbors will decelerate due to its larger internal pressure drop, leading to a spoke pattern where all fingers extend roughly the same distance r from the injection point. The number of growing fingers and the injected volume are then $N^{**} = \pi r(1-\varphi)/R$ and $V = b(1-\varphi)\pi r^2$, respectively, by volume conservation. Eliminating r then gives

$$N^{**} = \sqrt{\frac{\pi V(1-\varphi)}{bR^2}} \tag{4.1}$$

as the space-filling limit of $N(V)$, which applies at sufficiently high values of D_{visc}.

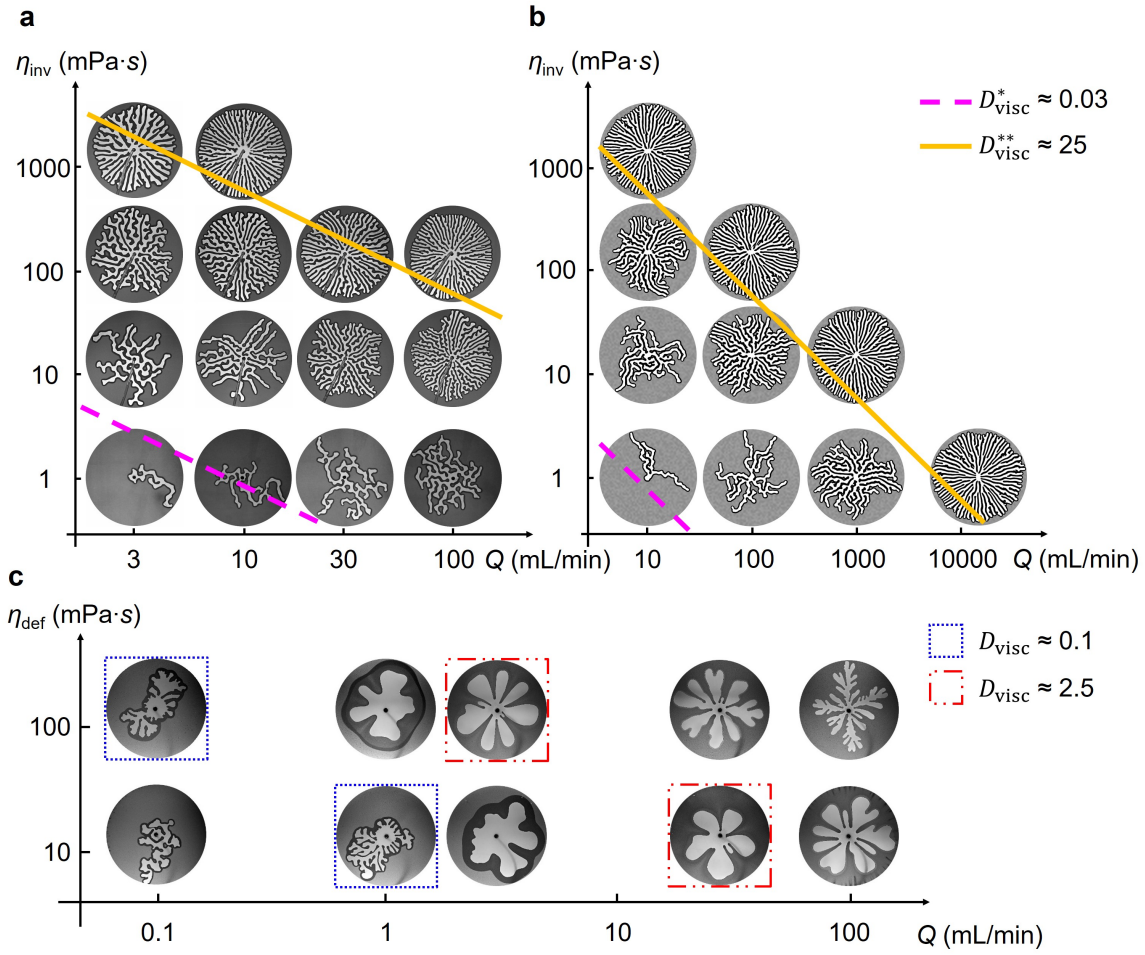

Fig. 4.5 η_{inv}–Q phase diagrams. (a) Experiments for viscously stable ($-\mathcal{M}$) invasion of water–glycerol mixtures into dry hydrophobic grains. The viscous deformability at which the pattern transitions from single to multiple fingers (D^{*}_{visc}, Eq. (4.4)) and from multiple fingers to radial spokes (D^{**}_{visc}, Eq. (4.3)) are plotted in dashed purple and solid yellow respectively. (b) Corresponding viscously stable ($-\mathcal{M}$) simulation results with an extended Q-axis. (c) Experiments for viscously unstable ($+\mathcal{M}$) invasion of air into hydrophilic grains submerged in a water–glycerol mixture. In all panels, $\varphi = 0.5$, $b = 0.9$ mm, and the disc diameter is 26.8 cm.

The critical viscous deformability D^{**}_{visc} at which $\Delta r_b = 2R$ can then be obtained by using Equation 3.12 to eliminate Q from (3.1), arriving at

$$D^{**}_{visc} = \frac{\Delta P_b b^2}{24GdR} N^{**}, \tag{4.2}$$

which, using the general expression for $R(\varphi)$ (Equation (3.11)), becomes

$$D^{**}_{\mathrm{visc}} = \frac{\Delta P_b b \pi r \sigma_0 \varphi}{24 G d \gamma} \approx 25, \tag{4.3}$$

where we have used $\varphi = 0.5$ and finger length $r = 13.4$ cm to compare directly to the experiments and simulations in the phase diagrams of Figure 4.5 a and b. D^{**}_{visc} agrees well with the visual characteristics of the patterns, transitioning from multiple fingers to a fully directional spoke pattern, although the transition is clearly a gradual one.

In the opposite limit of small D_{visc}, a single finger will grow without spawning a new finger while the breakout length Δr_b exceeds the radius r_{cell} of the flow cell. Taking the transition from a single finger to multiple fingers to occur at the value D^{*}_{visc} at which $\Delta r_b = r_{\mathrm{cell}}$, the same substitution that gave D^{**}_{visc} now yields

$$D^{*}_{\mathrm{visc}} = \frac{b^2 \Delta P_b}{12 G d r_{\mathrm{cell}}} \approx 0.03, \tag{4.4}$$

where $r_{\mathrm{cell}} = 13.4$ cm, $N = 1$, and other parameters are as in Equation (4.3). Note the dependence on system size: for a viscous invading fluid, branching will always occur if the system is large enough. Note also that the fingers in the experiments (and simulations) do not grow in a straight path toward the edge of the cell, but take tortuous paths dictated by local variations in packing density and the filling fraction. As a result, one should expect to see sprouting of a second finger at or slightly below D^{*}_{visc} as estimated above.

The ratio of the two critical deformabilities

$$\frac{D^{**}_{\mathrm{visc}}}{D^{*}_{\mathrm{visc}}} = \frac{r_{\mathrm{cell}} N^{**}}{2R} \approx 870 \tag{4.5}$$

is determined by the two characteristic length scales: system size and finger width.

For a quantitative analysis of the spatial characteristics of these patterns, we define 'pattern compactness' $c = A_{\mathrm{dis}}/(\pi r^2_{\mathrm{max}})$, where the displaced area A_{dis} includes both fingers and compaction fronts (but not undisturbed material) and r_{max} is the radial extent of the most advanced finger (Figure 4.6a). For the measurements presented here, $r_{\mathrm{max}} = r_{\mathrm{cell}}$. The theoretical low-D_{visc} limit $c' = 2R/(\pi r_{\mathrm{cell}}(1-\varphi)) \approx 0.04$ corresponds to a single straight finger. The measured c (Figure 4.6b) for $D_{\mathrm{visc}} < D^{*}_{\mathrm{visc}}$ is somewhat higher on account of the finger tortuosity. Beyond D^{*}_{visc}, c increases as viscous stabilisation creates multiple fingers and a more compact pattern. For radial spoke patterns beyond D^{**}_{visc}, the pattern compactness approaches 1.

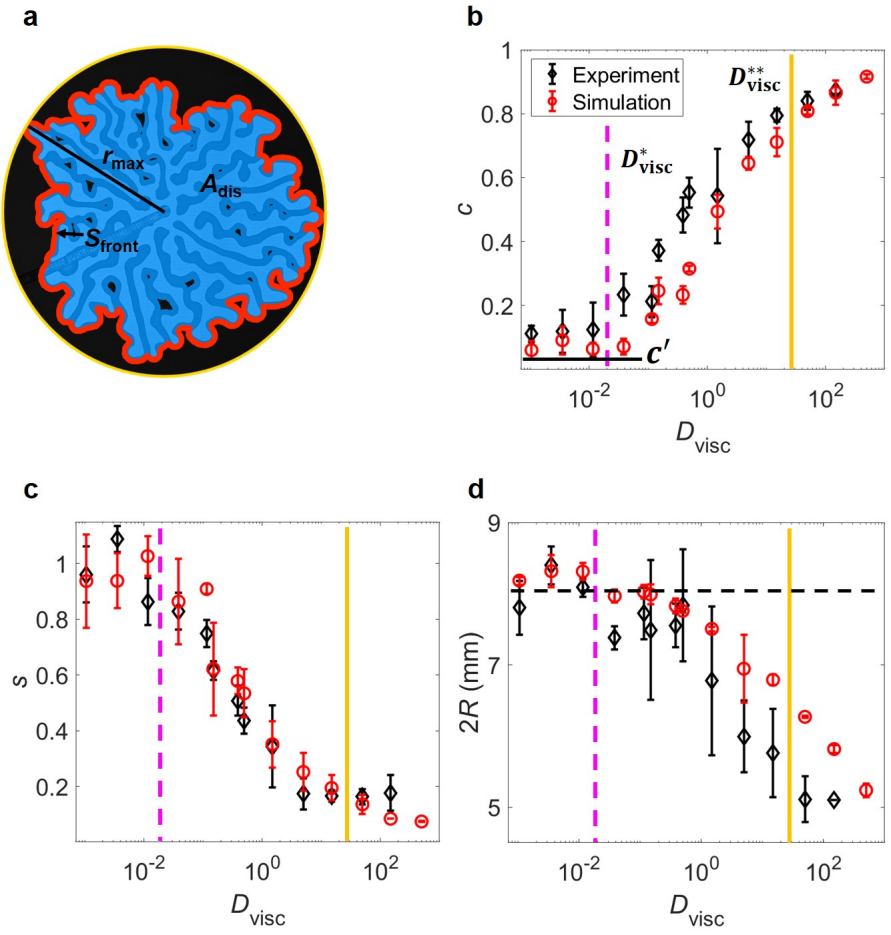

Fig. 4.6 Pattern characteristics: (a) definitions of front length S_{front} (red curve) and displaced area A_{dis} (invaded area plus compaction front, blue region), with r_{max} the reach of the most advanced finger. Then, (b) pattern compactness $c = A_{\text{dis}}/(\pi r^2_{\text{max}})$, (c) front instability number $s = S_{\text{front}}/S_{\text{finger}}$, and (d) finger width $2R$ as functions of D_{visc}. Black dashed line in (d): Theoretical prediction for 2R in frictional regime (Eq. 3.11). The error bars of the in the panels are obtained from three repeat experiments/simulations with the same parameters. All panels: $\varphi = 0.5$, $b = 0.9$ mm.

We define a 'front instability number' $s = S_{\text{front}}/S_{\text{finger}}$, where S_{front} is the outer perimeter of the connected advancing front (red line in Figure 4.6a) and S_{finger} is the internal perimeter of the finger pattern (along the fluid-air interface). $s \approx 1$ for a single finger, and decreases beyond D^{**}_{visc} as fingers increasingly meet to form a common front, plateauing at D^{**}_{visc} (Figure 4.6c).

The finger width $2R$ (Fig. 4.6d) is independent of D_{visc} for individual fingers, but starts to gradually decrease with D_{visc} as the self-confinement increases due to an increasing number of neighbouring fingers competing for space. There is a gradual transition from multiple

individual fingers to side-by-side radial spokes as viscous stabilisation becomes stronger and stronger as seen by $2R$ starting to decrease before the system reaches D^{**}_{visc}.

4.3.2 Viscously unstable displacement

Viscously *unstable* ($+\mathcal{M}$) flow was achieved by injecting air into hydrophilic glass beads submerged in a water/glycerol mixture in a Hele-Shaw cell [27]. The same batch of glass beads was used to create both the hydrophilic (acid washed) samples and the hydrophobic (acid washed then silanized) samples.

The key results for our purposes here are the changes in pattern formation as a function of D_{visc} illustrated in Fig. 4.7 and the $\eta - Q$ phase diagram in Fig.4.5 c. At low D_{visc}, ($Q = 0.1$ mL/min, $\eta = 14.14$ mPa·s, $D_{\text{visc}} = 5.9 \times 10^{-4}$) the invading air bulldozes the granular material into a compaction front in a similar way to that described in section 2.1. This is the "frictional regime" [27] and it behaves in much the same way in both $-\mathcal{M}$ and $+\mathcal{M}$ since the viscous effects are negligible in any case. One noticeable difference is the fact that the pumped invading fluid (air) is compressible in our $+\mathcal{M}$ experiments, causing the frictional fingers to start growing in an intermittent motion, transitioning to stick-slip bubbles [27]. The $-\mathcal{M}$ experiments by contrast, have an incompressible invading fluid (water/glycerol) that produces quasi-continuous motion with uniform finger widths.

A transition to a new flow pattern occurs as D_{visc} is increased ($Q = 0.1$ mL/min, $\eta = 141.4$ mPa·s, $D_{\text{visc}} = 9.7 \times 10^{-2}$ in Figure 4.7). The motion of the bulldozing granular front is now fast enough that it becomes partly lubricated by the interstitial viscous water/glycerol solution. The lower effective friction in the partly fluidised front results in a widening of the invasion structure and a thicker accumulation front. A striking consequence of the viscously unstable ($+\mathcal{M}$) configuration is the sprouting of secondary, narrower viscous fingers driven by the local pressure gradient across the fluidised front. This invasion structure (blue dotted box in Figure 4.5 c) was referred to as a "coral" pattern in [27].

At still higher D_{visc}, the fast flow drags the entire granular layer with it and there is no bulldozing up of a compaction front, for instance at $Q = 3$ mL/min, $\eta = 141.4$ mPa·s, $D_{\text{visc}} = 2.9$). The invasion dynamics is essentially that of *viscous fingering* into a granular suspension [141, 31, 27]. The viscous fingers are seen to narrow and become more dendritic with increasing D_{visc} as illustrated in Fig. 4.7 and the phase diagram (Fig. 4.5 c).

Note that for the patterns in the "viscous regime", the unstable viscous condition results in active growth focused on the most advanced sections of the interface, with regions behind experiencing viscous pressure screening such that they slow down and eventually come to rest, as is the case in the classical Saffmann-Taylor instability, as well.

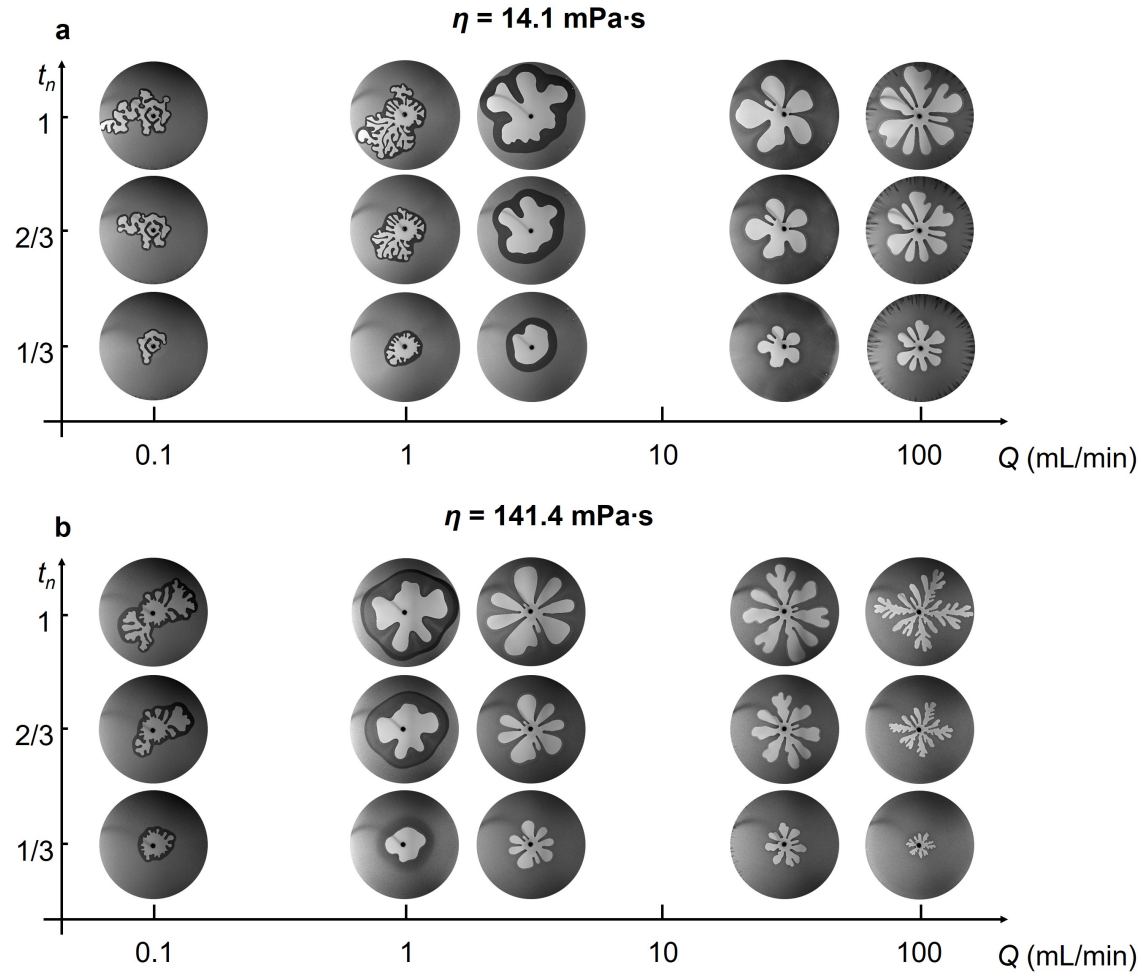

Fig. 4.7 Time evolution of experimental results of viscously unstable ($+\mathcal{M}$) invasion at different injection rate Q and viscosity η.In all panels, φ=0.5, b=0.9 mm, and the disc diameter is 26.8 cm.

4.3.3 Discussion

We have studied the fluid dynamics of an invading fluid displacing a defending fluid containing a sedimented granular material. In all cases, the granular material is wetted by the defending fluid and repelled by the invading meniscus (drainage). For loose packings of grains, as in this study, capillary forces dominate over the weak frictional strength G of the granular layer. In other words, the "capillary deformability" $D_{\mathrm{cap}} = (\gamma/d)/G$ is large in all experiments presented here, $D_{\mathrm{cap}} >> 1$, such that the meniscus can easily bulldoze the grains into compaction fronts that are then frictionally unstable.

Holding capillarity and friction essentially constant, we then explore the role of viscosity by studying both viscously stable ($-\mathcal{M}$) and viscously unstable ($+\mathcal{M}$) displacements. To do

so, we use mixtures of water and glycerol as either the invading fluid ($-\mathcal{M}$) or the defending fluid ($+\mathcal{M}$), with air as the opposing fluid. The log viscosity contrast is large in all our experiments ($1.7 < |\mathcal{M}| < 4.9$) such that pressure gradients in the low-viscosity fluid (air) are always negligible.

When viscous forces are negligible, the dynamics for both $-\mathcal{M}$ and $+\mathcal{M}$ are controlled by capillarity and the friction in the bulldozed compaction front. Pattern formation in this 'frictional regime' is rate-independent. Increasing Q or $\eta_{\max}$ increases the strength of viscous forces relative to frictional resistance, increasing the viscous deformability D_{visc}. As viscous forces become increasingly significant, there is a marked difference in how the $-\mathcal{M}$ and $+\mathcal{M}$ systems evolve.

Viscously stable ($-\mathcal{M}$) displacement involves pressure gradients along the invading fingers, with pressure decreasing from the central inlet toward the finger tips. Viscous stabilisation manifests as the sprouting of new, intermediate fingers once the frictional 'breakout' pressure ΔP_b of the walls is exceeded. Two mechanisms determine the role of viscous stabilization: (1) the strength of viscosity relative to friction, as measured by D_{visc}, and (2) the distance between the central inlet and the finger tips. We have identified two critical threshold values of D_{visc} that separate different fingering behaviour. Starting with a single finger at low D_{visc}, increasing D_{visc} eventually leads to the first threshold value $D^{*}_{\text{visc}} \sim \Delta P_b/G$ at which the viscous pressure along the finger grows large enough to cause branching before the finger reaches the outer boundary; this value depends on the size of the system, since a longer finger implies a larger viscous pressure drop for the same value of D_{visc}. As a result, larger cells would produced multiple fingers at lower D_{visc}. Further increasing D_{visc} leads to the second threshold value D^{**}_{visc}, at which the viscous pressure gradient within the fingers is large enough to produce breakout pressures immediately behind the finger tips. Fingers that move ahead of the pack are suppressed by their internal viscous pressure drop and new fingers sprout continuously to populate an ever increasing pattern perimeter (in a radial cell). Ultimately, the fingers grow side-by-side in a space-filling radial spoke pattern.

In contrast, viscously unstable ($+\mathcal{M}$) displacement localises the viscous pressure drop within the *defending fluid*. As a result, the growth of already-advanced sections of the interface is promoted and un-invaded regions are screened, as in classical Saffman–Taylor fingering. The second main mechanism controlling $+\mathcal{M}$ displacement at high D_{visc} is the fact that the grains are submerged in the high viscosity water/glycerol fluid which, entrained in the bulldozed front, lubricates the moving sections of the interface [28]. This lubrication reduces the granular friction, allowing fingers to widen and therefore also accumulate much thicker compaction fronts. Peculiar to this system is that the viscous instability mechanism

acts both on the system scale, and also locally: The compaction front is itself unstable to perturbations, with tiny air fingers growing along the moving sections of the front, leading to the coral pattern shown in Figure 4.7b. For extreme D_{visc}, the fluid flow is fast enough to mobilise the entire granular layer, and the system reverts to what is essentially viscous fingering in a granular suspension. All of these displacements depend inherently on system size.

4.4 Conclusion

We have used experiment and simulation to discover how frictionally unstable flow patterns are shaped by viscous forces in both viscously stable and unstable scenarios. Multiphase flows involving granular materials occur in a wide range of natural and engineering processes, including soil and mud flows, methane venting from sediments, degassing of volatiles from magma, fluidised bed chemical reactors, and the processing of granular and particulate systems in food-, pharmaceutical-, and numerous other industries [9, 16, 149–151]. These systems are inherently difficult to predict and control because of their complexity, which manifests itself through the self-organization of a wide variety of intricate patterns. In this study we have discovered how granular friction, capillary forces and viscous pressure together conspire to produce a striking variety of multiphase flow patterns, and how these can be characterized and understood in terms of the stabilizing and destabilizing mechanisms imparted by the forces involved.

Chapter 5

Stabilization by gradients in viscosity, gap thickness and gravity

5.1 Introduction

In the previous chapters, frictional fingers were observed after water/glycerol mixture invaded radial cell containing the dry hydrophobic granular material. In this chapter, we switch the geometry to a linear cell, and investigate three separate mechanisms for stabilization/destabilization: Viscous pressure gradients, gap thickness variations, and elevation gradients in the gravitational field. This chapter presents initial findings based on experiments and numerical simulations. Note that the studies in this chapter are within ($+$W, $-\mathcal{M}$) quadrant as shown in Figure 5.1.

As in the radial cell in the previous chapters, we find an increased degree of viscous stabilization when we increase the viscosity of the invading fluid. In the linear channel, instead of a radial spoke pattern, we get parallel streaks of granular material left behind a stabilized front confined to the width of the cell. After calibrating the simulation to experiments we find a striking stabilization/destabilization effect caused by implementing a gradient in the cell gap in in the simulated geometry. Finally in this chapter we demonstrate the stabilization/destabilization effect of gravity by tilt the cell. Note that all the studies in Chapter 5 focuses on the situation of $-\mathcal{M}$ and $+$W (shown in Figure 5.1).

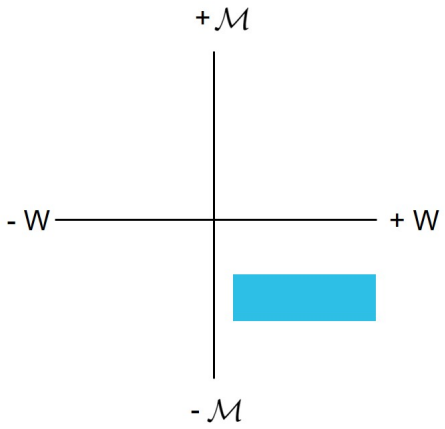

Fig. 5.1 he quadrant with blue square in the diagram of viscosity ratio $\mathcal{M}$ and wettability $\mathrm{W} = -\cos\theta$ is the study focus of Chapter 5.

5.2 From unstable to stable front: effects of viscosity

5.2.1 Methodology

Experimental setup

A new Hele-Shaw cell was used in this section as shown in Figure 5.2. To make a linear boundary, adhesive tapes were attached along opposite sides of both top and bottom plates. The surface of the plates were treated using silanization solution as described in Chapter 3. The same hydrophobic beads and granular bed preparation method as in Chapter 3 were used here.

To avoid the liquid leak from the boundary, the surface of the tapes were also treated using silanization solution and the two plates were clamped tightly together. In this case, the tapes on top and bottom had the same thickness (0.55 mm) and also functioned as spacers to define the cell gap. The tape on the bottom plate served as the mold for spreading an even layer of the hydrophobic grains as described in previous chapters. The tapes on the top and the bottom plates were aligned before clamping such that b = 1.10 mm and φ = 0.5.

By mixing glycerol to deionized water, with concentrations of 0%, 30%, 50%, 70%, 80%, 91% and 100% by volume, we get the invasion fluid with the viscosity of 1, 3, 8.4, 35.1, 91.5, 347 and 1414 mPa·s respectively at room temperature 20°C[147].

We injected the aqueous glycerol into the cell using a syringe pump (Harvard Scientific, PHD Ultra). The cell was backlit, such that invaded regions appear bright and compacted regions dark (Figure 5.2). Results were recorded using a Nikon 1 J2 digital camera at 30 frames per second.

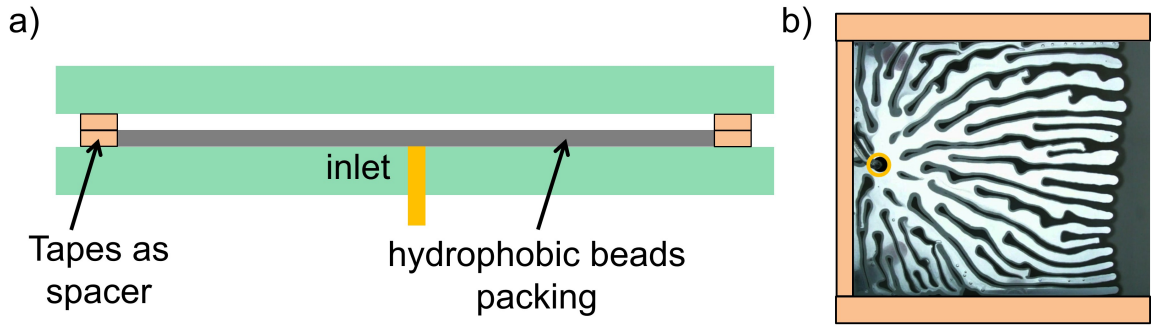

Fig. 5.2 (a) Schematic cross-section of the Hele-Shaw cell. Tapes with the same thickness are attached to both bottom and top plates, producing a granular bed with $\varphi = 0.5$. (b) Top view of invading fingers. The white region has been invaded with water and cleared of grains, while the darkest region (the compaction front) has been completely filled with grains. The packing is confined within three boundaries that are illustrated by the brown strips in the figure.

Simulation method

For the numerical simulation, we used the same code introduced in Chapter 3, but the cell was set to be rectangular instead of radial, with the dimension of 23.0 $\times$ 26.4 cm. The invasion was started from one of the short edges to match the inlet position in the experiments. In the previous cases the simulation would be stopped once the finger tips reached the boundary of the cell, while the simulations here ran until complete invasion of the beads field. The boundary width was 1.5 cm at each side, such that the beads concentration field is 20.0 $\times$ 23.4 cm, the same as that in the experiment. The viscosity and the injection rate were changed correspondingly to match the experiment results.

5.2.2 Results and discussion

In this section we investigate the effect of the degree of viscous stabilization on the frictional fingering pattern in a linear geometry. The Hele-Shaw cell is sealed along three sides with the injection point at one end opposite the open such that the flow occurs in a straight channel. One important characteristic of a channel cell is that the width available for flow remains constant. The compactness of the pattern is thus clearer to ascertain compared to in a radial cell where the pattern circumference expands over time and the average growth velocity along the perimeter therefore slows down as the pattern becomes bigger.

Figures 5.3 a and b show the experimental and simulation results for the channel, where we control the pattern formation by changing the the viscosity of the invading fluid, keeping the injection rate the same (Q = 10 ml/min). Note that in the previous sections D_{visc} was

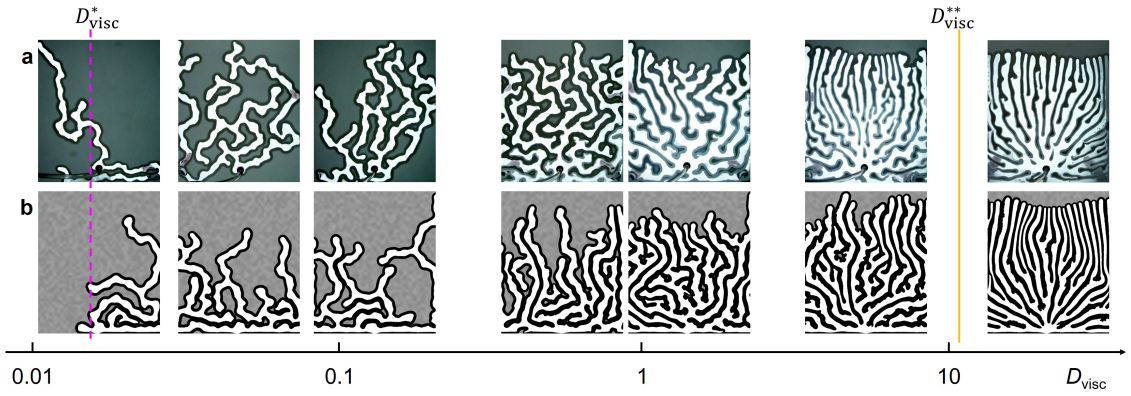

Fig. 5.3 (a) Experiment and (b) simulation results at different viscosity ratio but all at injection rate 10 mL/min. Each rectangle has the dimension 20.0 × 23.4 cm. Simulation frames are chosen such that the injection time and volume matches the corresponding experimental frames. All panels: $\varphi = 0.5$, $b = 1.10$ mm.

controlled by varying the injection rate. In this section, η_{inv} is varied, which means both $\mathcal{M}$ and D_{visc} varies. We have defined $\mathcal{M}$ and D_{visc} such that the degree of viscous stabilization increases for larger negative values of $\mathcal{M}$ or larger values of D_{visc}. Figure 5.3 presents the results on a D_{visc} axis with the leftmost panel ($-\mathcal{M} = 1.7$, $D_{\mathrm{visc}} = 0.02$) being injection of pure water into dry hydrophobic grains, and the rightmost panel ($-\mathcal{M} = 4.9$, $D_{\mathrm{visc}} = 30.3$) injection of pure glycerol. The intermediate values are achieved by mixing water and glycerol in different ratios.

The results show a clear transition from an unstable advancing front where the capillary-frictional instability dominates, to a stable advancing front as viscous stabilization increasingly plays a role in shaping the pattern. For water injection, there is just one finger advancing at a time. Increasing η to make the viscosity difference between the invading fluid and the defending fluid larger, we observe more fingers advancing simultaneously and the growth becomes more directional, parallel to the flow along the channel. The response to increased viscosity in the invading phase is thus similar to the effect of increased injection rate which is unsurprising since both lead to increased D_{visc}.

The two most noticeable changes to the pattern as a function of D_{visc} is that the displacement front becomes increasingly stabilized into a level front, and that the pattern behind the front becomes more compact and space-filling. Similar to Chapter 4, the critical viscous deformability for the transition from multiple fingers to level front, D^{**}_{visc}, can be calculated by Eq. 5.1. However, the calculation of N^{**} is different from the previous. When the critical distance Δr_b becomes smaller than the finger width $2R$, branching will be suppressed not only by the presence of neighboring fingers but also the boundary to the linear cell with a width S_{cell}. The number of growing fingers is then $N^{**} = S_{\mathrm{cell}}(1-\varphi)/R$.

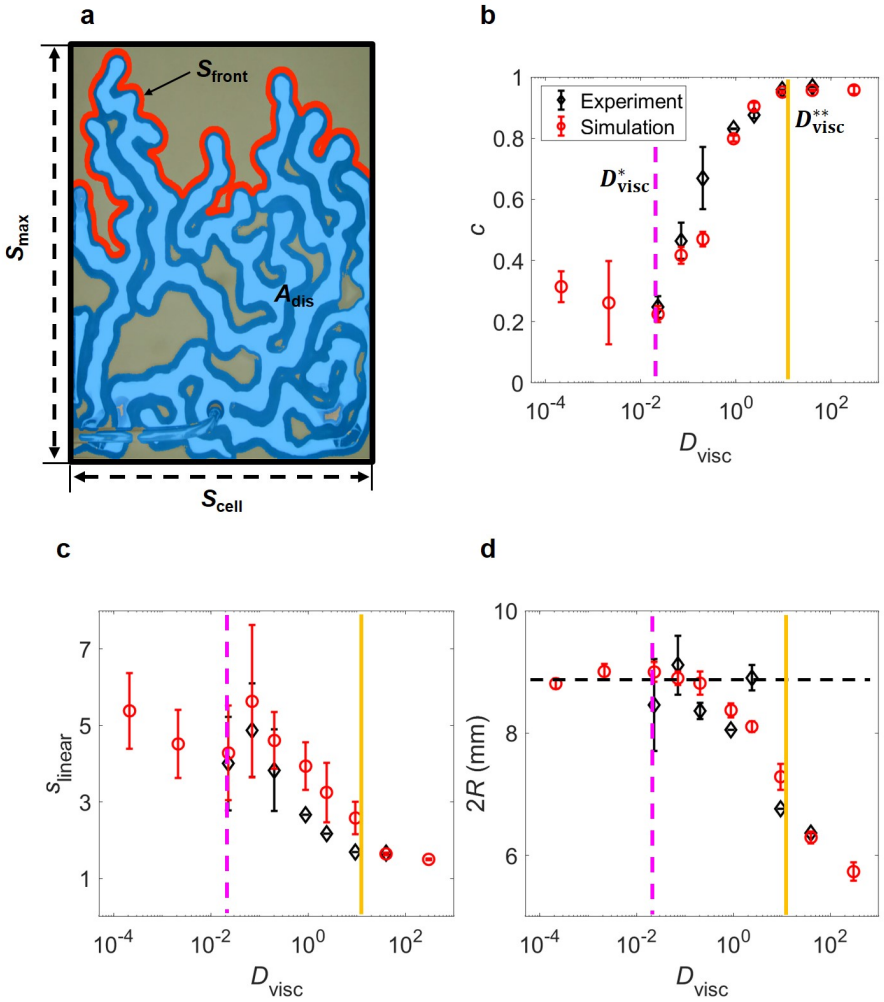

Fig. 5.4 Pattern characteristics: (a) definitions of front length S_{front} (red curve) and displaced area A_{dis} (invaded area plus compaction front, blue region), with $S_{\max}$ the reach of the most advanced finger and S_{cell} the cell width. Then, (b) pattern compactness $c = A_{\text{dis}}/(S_{\max}S_{\text{cell}})$, (c) front stability number $s_{\text{linear}} = S_{\text{front}}/S_{\text{cell}}$, and (d) finger width $2R$ as functions of D_{visc}. Black dashed line in (d): Theoretical prediction for 2R in frictional regime (Eq. 3.11). The error bars of the in the panels are obtained from three repeat experiments/simulations with the same parameters. All panels: $\varphi = 0.5$, $b = 1.10$ mm.

Using the general expression for $R(\varphi)$ (Equation (3.11)), becomes

$$D^{**}_{\text{visc}} = \frac{\Delta P_b b S_{\text{cell}} \sigma_0 \varphi}{24 G d \gamma} \approx 22, \tag{5.1}$$

where we have used $\varphi = 0.5$ and $S_{\text{cell}} = 20$ cm to compare directly to the experiments and simulations in the phase diagrams of Figure 5.3 a and b, D^{**}_{visc} agrees well with the visual

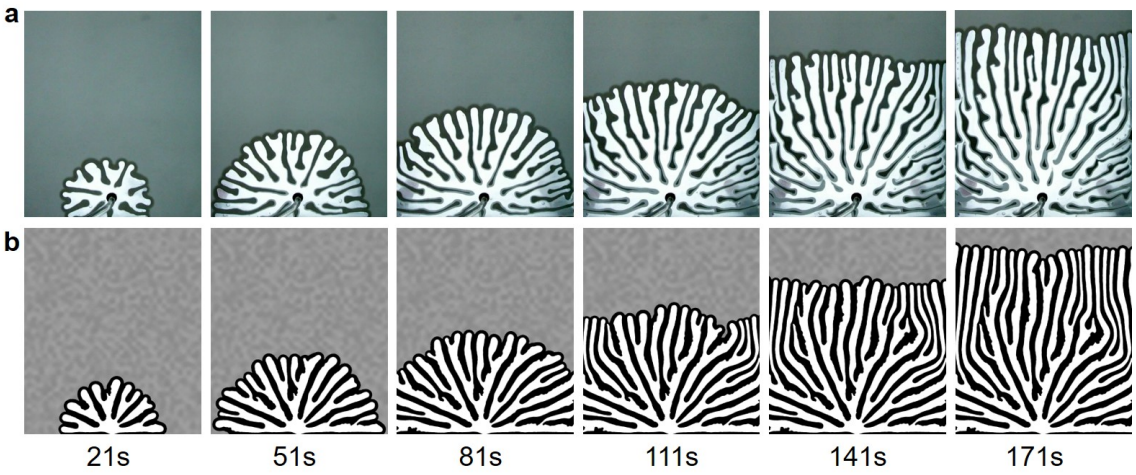

Fig. 5.5 Time sequence of fluid invasion in (a) Experiment and (b) simulation at D_{visc} = 30.3. Each rectangle has the dimension 17.0 $\times$ 20.3 cm. Simulation frames are chose after the same injection time and fluid injection volume with the experiment.

characteristics of the patterns, transitioning from multiple fingers to a level marching pattern, although the transition is clearly a gradual one.

In the opposite limit of small D_{visc}, a single finger will grow without spawning a new finger while the breakout length Δr_b exceeds max length $S_{\max}$ of the flow cell. Taking the transition from a single finger to multiple fingers to occur at the value D^*_{visc} at which $\Delta r_b = S_{\max}$, the same substitution that gave D^{**}_{visc} now yields

$$D^*_{\text{visc}} = \frac{b^2 \Delta P_b}{12 G d r_{\text{cell}}} \approx 0.02, \tag{5.2}$$

where $S_{\max} = 23.4$ cm, $N = 1$, and other parameters are as in Equation (5.1). Note the dependence on system size: for a viscous invading fluid, branching will always occur if the system is large enough. Note also that the fingers in the experiments (and simulations) do not grow in a straight path toward the edge of the cell, but take tortuous paths dictated by local variations in packing density and the filling fraction. As a result, one should expect to see sprouting of a second finger at or slightly below D^*_{visc} as estimated above.

To quantify the characteristics of these patterns, we define 'pattern compactness' as $c = A_{\text{dis}}/S_{\max}S_{\text{cell}}$ where A_{dis} is the area covered by the finger structure including compaction front, and $S_{\max}$ is linear extent of the most advanced finger. Figure 5.4b shows how c increases with D_{visc} from an extreme low for a single finger to a value approaching unity for the fully stabilised case when all fingers march on a level front, leaving no gaps behind.

We define a 'front instability number' of linear cell $s_{\text{linear}} = S_{\text{front}}/S_{\text{cell}}$, where S_{front} is the outer perimeter of the connected advancing front (red line in Figure 5.4a) and S_{cell} is the width of the linear cell. As shown in Figure 5.4c, s_{linear} approaches 1 for extreme level of viscous stabilization and decreases beyond D^{*}_{visc} as fingers increasingly meet to form a common front, plateauing at D^{**}_{visc} (Figure 5.4c).

The finger width $2R$ (Fig. 5.4d) is independent of D_{visc} for individual fingers, but starts to gradually decrease with D_{visc} as the self-confinement increases due to an increasing number of neighbouring fingers competing for space. There is a gradual transition from multiple individual fingers to side-by-side level marching as viscous stabilisation becomes stronger and stronger as seen by $2R$ starting to decrease before the system reaches D^{**}_{visc}.

5.3 Effects of plate spacing on pattern formation

5.3.1 Methodology

Effects of plate spacing on pattern formation are studied in this section. The experimental method is the same as introduced in Section 4.2. We here changed the plate spacing b by changing the thickness of the tapes attached on the plate surface. Deionized water was injected to the packing at Q = 1 mL/min. The experiment was limited by the packing preparation technique, b was only able to be changed to 0.67, 0.91 and 1.10 mm. However, based on the studies in Chapter 3 and Section 4.2, we can reasonably trust the simulation results and do more parameter study with the numerical method described in Chapter 3. We kept the filling fraction φ constant and equal to 0.5 in every simulation. The plate spacing b was varied between 0.3 and 1.5 mm in different simulations. The cell dimension was set to be $x \times y$ = 20 $\times$ 30 cm. In this initial study we focus on the frictional regime, and the injection rate was set as 1 mL/min to limit viscous effects.

Furthermore, we studied the effect of gradient of b on pattern formation. In the same simulation, while φ kept constant, the plate spacing of the cell was set to be changed in a gradient of either increasing or decreasing gap height from the inlet towards the opposite edge of the cell. (as illustrated in Figure 5.6 a). The plate spacing b in the simulation was replaced by the equation:

$$b = \frac{db}{dy} y + b_{\text{start}} \tag{5.3}$$

where db/dy is the gap gradient along y direction, b_{start} the spacing of on the start line, y is y-coordinate of the current position with the plate spacing b.

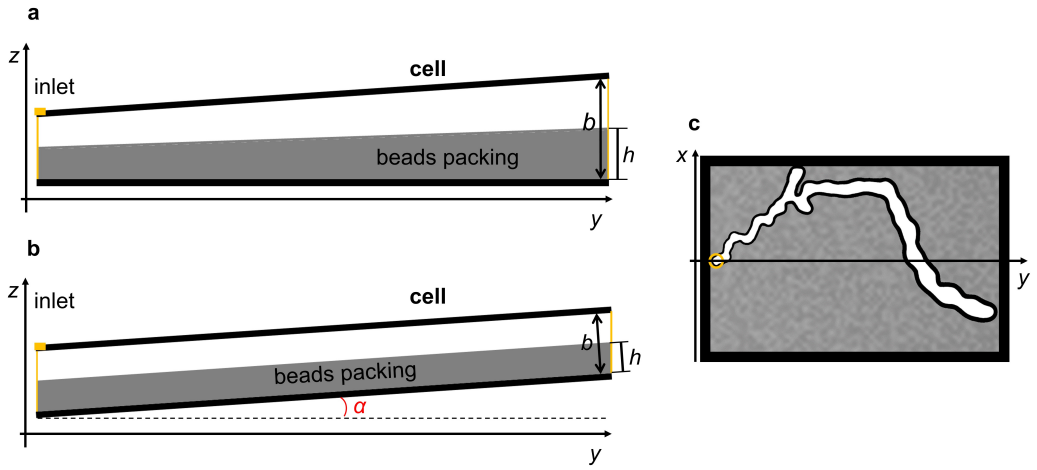

Fig. 5.6 (a) Schematic of the gap gradient simulation. Plates gap b and height h of the beads packing changed simultaneously keeping the filling fraction φ constant in all the regions of the cell. Note that "plates gap" and "beads packing" here are only for demonstration, the beads concentration field in the simulation is actually represented by an array of values. (b) Schematic of the tilted cell simulation. The cell is tilted in an angle α, and b and h are kept constant. (c) Simulation result of an invading finger in a simulation with gap b increasing from left to right. The white region has been invaded while the black region around the finger is the compaction front. In all panels, z axis is along the height of the cell, y axis is along the length of the cell, and x axis is along the width of the cell.

In addition to studying the effect of a gap gradient, we also study the effect of a gradient in the elavation (keeping the gap spacing constant) to investigate the role of gravitational stabilisation. We define a tilt angle α as shown in Figure 5.6 b. In the same simulation, while other parameters kept constant, α was changed to be either larger than 0 (inlet was the lower point of the cell) or smaller than 0 (inlet was the higher point of the cell.). The value of α ranged from -6° to 6°. In all the cases here, the invading fluid (water) has a higher viscosity than the defending fluid (air). The patterns at different α are compared and the principles behind are discussed.

5.3.2 Restults and discussion

Finger width as a function of plate spacing

Figure 5.7 shows the experimental results at different plate spacing b (no gradient), and Figure 5.8 shows a series of simulation results at different b ranging from 0.3 to 1.5 mm. As b increases, we observe a widening of the finger.

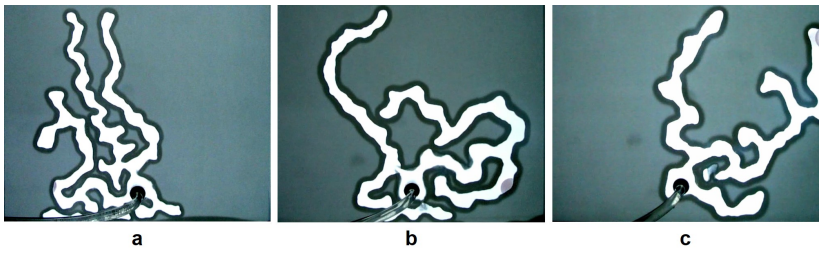

Fig. 5.7 Experiment results at different spacing b (a) 0.67 mm, (b) 0.91 mm, (c) 1.10 mm. All panels: $\varphi = 0.5$, and the dimension is 24.5×20 cm.

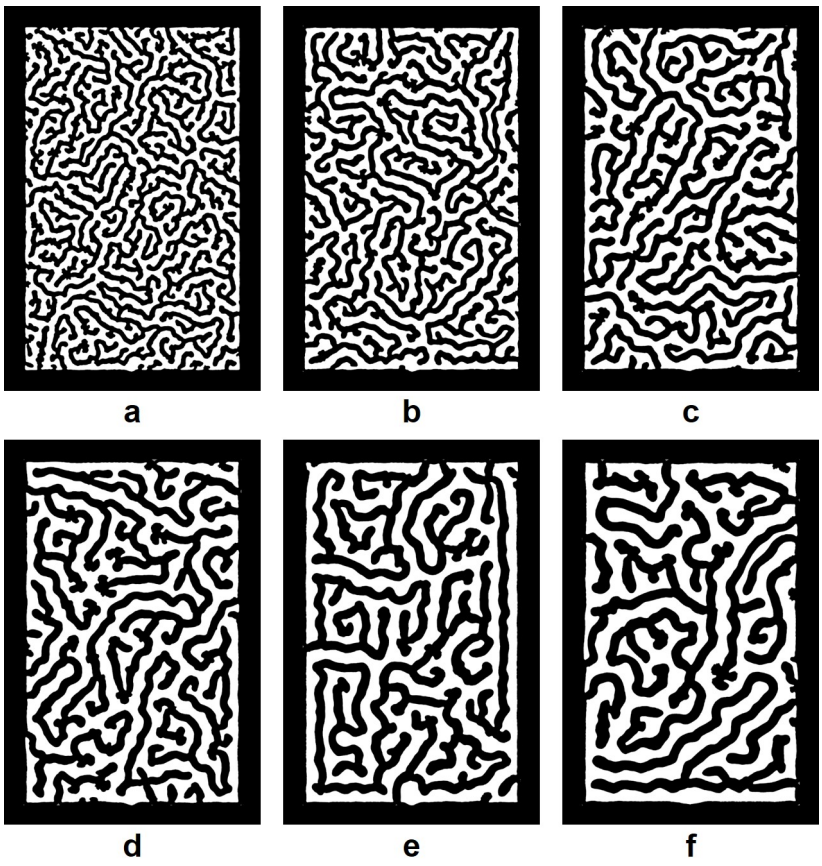

Fig. 5.8 Simulation results at different spacing b (a) 0.5 mm, (b) 0.7 mm, (c) 0.9 mm, (d) 1.1mm, (e) 1.3 mm and (f) 1.5 mm. All panels: $\varphi = 0.5$, and the dimension is 20×30 cm (including the black frames). The black frames are the boundaries of the cell, finger will turn back if it hits to the boundary.

We have previously found that filling fraction φ determines the finger width: finger width $2R$ increases with the decrease of φ. This is because the frictional stress σ becomes smaller when decreasing φ, as expressed in the approximate linear expression of σ introduced in Chapter 3 (Eq. 3.7):

$$\sigma = \sigma_0 \frac{R}{b} \frac{\varphi}{1-\varphi} \tag{5.4}$$

Here we keep the filling fraction constant and run the simulation at low D_{visc}, only two forces are significant: surface tension and friction. According to the expression of R introduced in Chapter 3, one may find that R is also determined by plate spacing b, or, more specifically, R is predicted by the model to increase with the square root of b:

$$R = \left[\frac{\gamma(1-\varphi)}{\sigma_0 \varphi}\right]^{\frac{1}{2}} b^{\frac{1}{2}} \tag{5.5}$$

We plot the finger width $2R$ as a function of spacing b in Figure 5.9 for experiments, theory and simulations. There is a strong match between the simulation data and the theoretical curve, and a reasonable match to the limited experimental results..

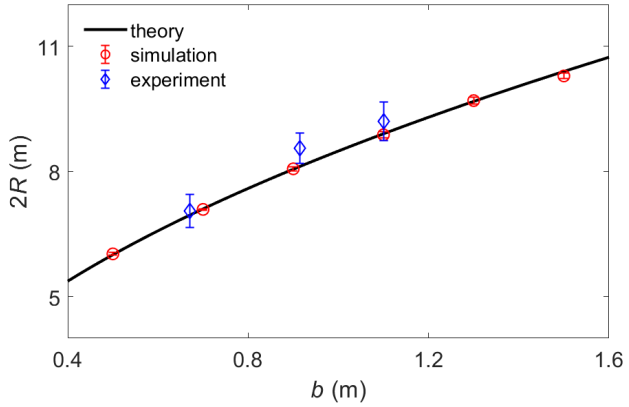

Fig. 5.9 Finger width $2R$ as a function of spacing b. The error bars of the experimental data show the standard deviation of three measured finger width from three different stages, and the error bars of the simulation data show the standard deviation of three measured finger width from three simulation results. $\varphi = 0.5$.

Transition in finger alignment controlled by gap gradient

In this section, the effect of gap height gradient on pattern formation is studied using the calibrated numeric model. We set the spacing of the cell distributed in a gradient from the inlet towards the opposite edge according to Equation 5.3. We here use db/dy to represent a positive gradient (b increases along the cell from the inlet onwards), use -db/dy to represent a negative gradient (b decreases along the cell from the inlet onwards).

A large b difference 0.12 mm (0.15 mm and 0.03 mm at two ends respectively) is used to produce distinct results. As shown in Figure 5.10, two clearly different finger growing

patterns are formed in the initial stages when we invert the gap gradient db/dy. When db/dy = -0.004, i.e., b decreases along +y direction, the finger is more likely to grow laterally, the beads concentration field is invaded or filled gradually from the inlet onward to the opposite end of the cell. When db/dy = 0.004, i.e., b increases along +y direction, finger tends to grow along +y direction or vertically in the images, the beads concentration field is initially invaded by a continuously advancing finger. After the finger reaches the opposite end of the cell, the finger start to grow in a manner similar to when db/dy = -0.004 but downward.

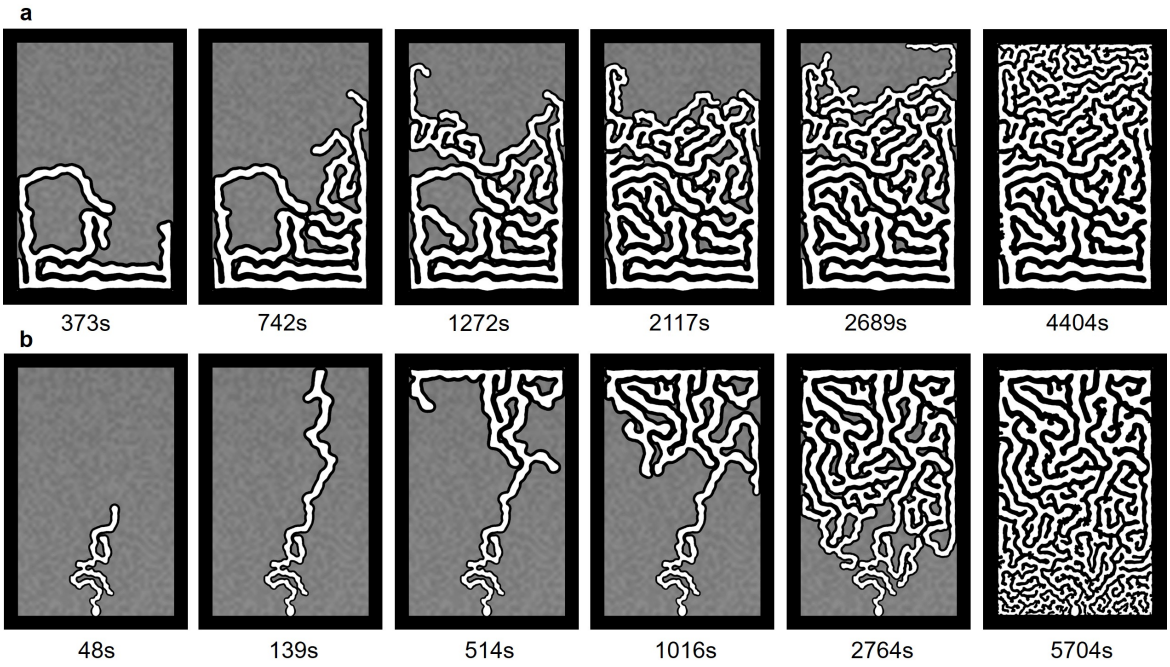

Fig. 5.10 Time evolution of finger growth when gap gradient db/dy equal to (a) - 0.004 and (b) 0.004. All panels: $\varphi = 0.5$, and the dimension is 24.5×20 cm (including the black frames). The black frames are the boundaries of the cell, finger will turn back if it hits to the boundary.

Figure 5.11 a shows the patterns formed at different (-db/dy). The finger grows in a random way towards the opposite end of the cell when there is no gap gradient, i.e., db/dy = 0. Once (-db/dy) > 0, the finger prefers to stay in high b region and tends to grow laterally. This trend becomes more obvious when we increase (-db/dy). To better illustrate this trend, we use the pattern compactness as described in the last section and Figure 5.4, $c = A_{\text{dis}}/(S_{\max}S_{\text{cell}})$. Figure 5.11 b shows that the compactness c of the pattern increases with (-db/dy), illustrating that the ways of the finger growth tend to change from random loose to compact and the invaded fingers tend to align and occupy more regions of the packing (i.e., compactness number c approaches 1) at higher (-db/dy). The front instability

number $s_{\text{linear}} = S_{\text{front}}/S_{\text{cell}}$ is also calculated here, where S_{front} is the length of the connected advancing front (red line in Figure 5.4 a) and S_{cell} is the cell width. Figure 5.4 c shows that s decreases with (-db/dy) and approaches 1 at higher (-db/dy).

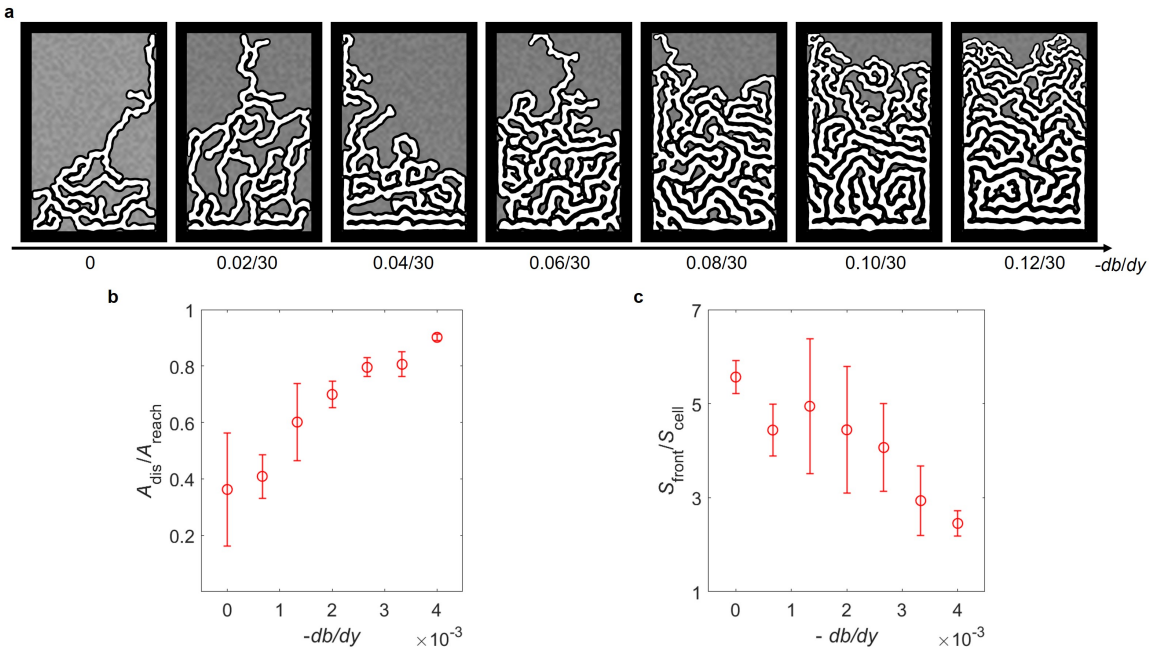

Fig. 5.11 (a) Patterns formed at different -db/dy. (b) Compactness $c = A_{\text{dis}}/A_{\text{reach}}$ and (c) Instability ratio $s = S_{\text{front}}/S_{\text{cell}}$ as a function of -db/dy. All panels: $\varphi = 0.5$, and the dimension is 20×30 cm (including the black frames). The black frames are the boundaries of the cell, finger will turn back if it hits to the boundary.

For the patterns formed at positive db/dy in Figure 5.12 a, the growth of the finger tends to be more directional — towards the opposite end of the cell. We define a directionality number $d_f = L_{\text{finger}}/L_{\text{cell}}$, where L_{finger} is the length of the finger, L_{cell} is the length of the cell along y direction in Figure 5.6. Figure 5.12 b shows how d_f increases with db/dy.

The principles behind can be explained by Equation 3.9 and Equation 5.5. The increase of b will decrease the friction stress and increase the finger width thereby decreasing the capillary pressure, causing a smaller threshold pressure P_t. This means the finger will grow preferentially in high-b region. When $db/dy < 0$, the region close to the inlet has higher b, the finger is more likely to grow in this region until it is occupied, such that horizontal alignment is observed. When $db/dy > 0$, the region far from the inlet has higher b, the finger is more likely to grow towards the high-b region, and this trend becomes more obvious at high db/dy.

Growth of frictional fingers are therefore unstable in the direction of an increasing gap, resulting in preferential growth in the direction of the steepest gradient db/dy. In a confined

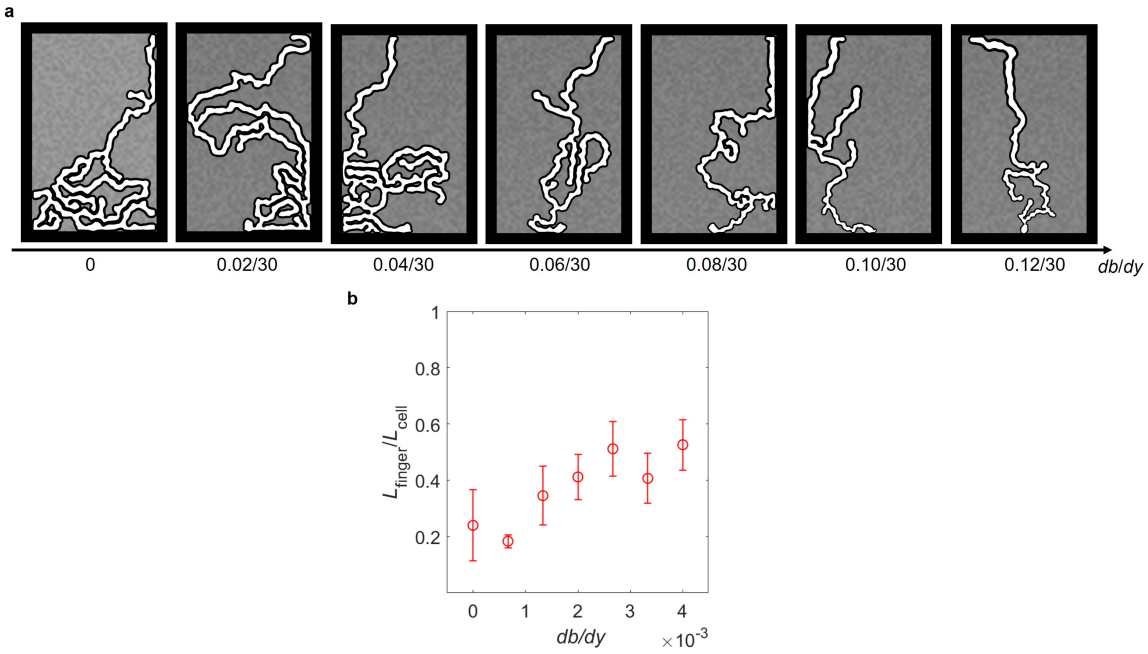

Fig. 5.12 (a) Patterns formed at different db/dy. (b) Directionality of the finger $d_f = L_{\text{finger}}/L_{\text{cell}}$ as a function of db/dy. All panels: $\varphi = 0.5$, and the dimension is 20×30 cm (including the black frames). The black frames are the boundaries of the cell, finger will turn back if it hits to the boundary.

system where the fingers are already at the high b point, forced growth into a decreasing gap region will result in a stabilisation of the front and a more compact pattern. For a system with fixed boundaries like we study here, a system that starts off unstable with the inlet at the narrow gap end, the pattern will revert to the stabilised compact growth once the initially unstable finger reaches the high gap end.

5.4 Effects of tilt angle on pattern formation

Gravitational stabilization of frictional fingers in a tilted cell was studied by Eriksen *et al.* who found that in a horizontally placed cell, finger growth was random and nondirectional, the cell space was partially displaced by the air and other places remained undisturbed. While in a tilted cell, the air invaded the whole space of the cell in a compact pattern of aligned fingers (shown in Figure 1.6). Here we complement these findings by comparing gravitational stabilisation to a case where the invading fluid has a higher viscosity in contrast to their study. Only numerical simulation results are discussed briefly here, experiments are left for future work.

The cell was set to be tilted in a certain angle as shown in Figure 5.6 b. We here use α to represent the positive tilt angle (inlet is the lower point of the cell), use -α to represent the negative tilt angle (inlet is the higher point of the cell).

Figure 5.13 shows two distinct patterns at α = 4° and -4°. At α = 4°, the finger is more likely to grow laterally, the beads concentration field is invaded gradually from the inlet onward to the opposite end of the cell. The denser invading fluid naturally grows in a stabilised manner from the lower towards the higher elevation in the cell. At α = -4°, the finger tends to grow along +y direction or vertically in the images, the beads concentration field is initially invaded by a continuously advancing finger. Here, the denser invading fluid is unstable when elevated above a less dense defending fluid containing the grains, and density driven unstable flow occurs. After the finger reaches the opposite end of the cell, the finger start to grow in a manner similar to when α = 4° but downward.

Figure 5.14 a shows the patterns formed at different α, the finger grows in a more random way at low α and tends to grow horizontally at high α. Figure 5.14 b shows that the compactness c of the pattern increases with α, illustrating that the ways of the finger growth tend to change from random loose to compact and the invaded fingers tend to align and occupy more regions of the packing (i.e., compactness number c approaches 1) at higher α. The instability ratio s is also calculated here, Figure 5.4 c shows that s decreases with α and approaches 1 at higher α. The results demonstrates the stabilizing mechanism of gravity in a tilted system, where the denser invading fluid preferentially occupies the lower elevation parts of the cell, and where the degree of stabilization increases with increasing tilt angle.

Figure 5.15 a shows the finger consisting of the denser invading fluid invading from the high elevation end of the cell, and the growth is therefore gravitationally unstable, the finger tending to sink towards the lower elevation edge of the cell. Figure 5.15 b shows directionality number d_f increases with the increase of (-α) and tends to approach 1 at high (-α).

The patterns formed at $\alpha > 0$ is very similar to when $db/dy < 0$, and the patterns formed at $\alpha < 0$ is very similar to when $db/dy > 0$, but the principles behind are different. In the situation when the cell is horizontally placed, the threshold pressure P_t that enables the finger to grow is the sum of the frictional stress σ and the capillary pressure as described in Equation 3.9. However, at $\alpha \neq 0$, hydrostatic pressure difference of the invading fluid caused by the gravity starts to affect the pattern formation, this pressure difference is written as $\rho g y \sin\alpha$, where y is the coordinate along y-axis as shown in Figure 5.6, $y\sin\alpha$ is the height difference across y, ρ is the density of the invading liquid, g is the gravitational acceleration.

At $\alpha > 0$, the component along the cell of the gravitational force of the invading liquid points to the inlet side, adding an extra resistant force for finger growth. At $\alpha < 0$, the

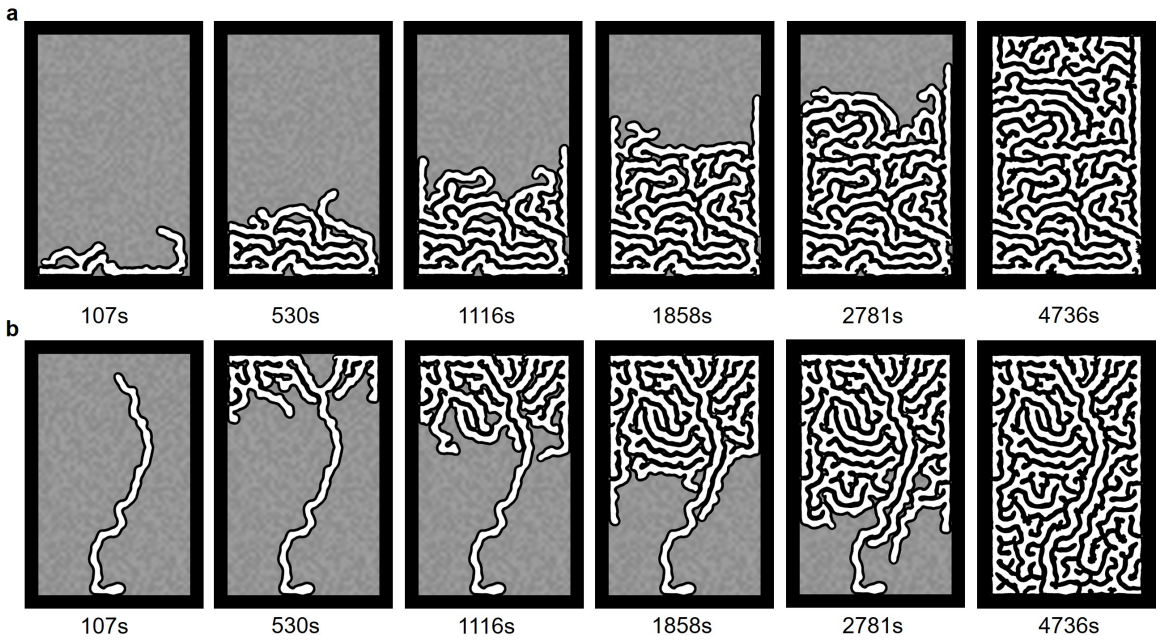

Fig. 5.13 Time evolution of finger growth when tilt angle α equals to (a) 4° and (b) -4°. All panels: $\varphi = 0.5$, and the dimension is 20×30 cm (including the black frames). The black frames are the boundaries of the cell, finger will turn back if it hits to the boundary.

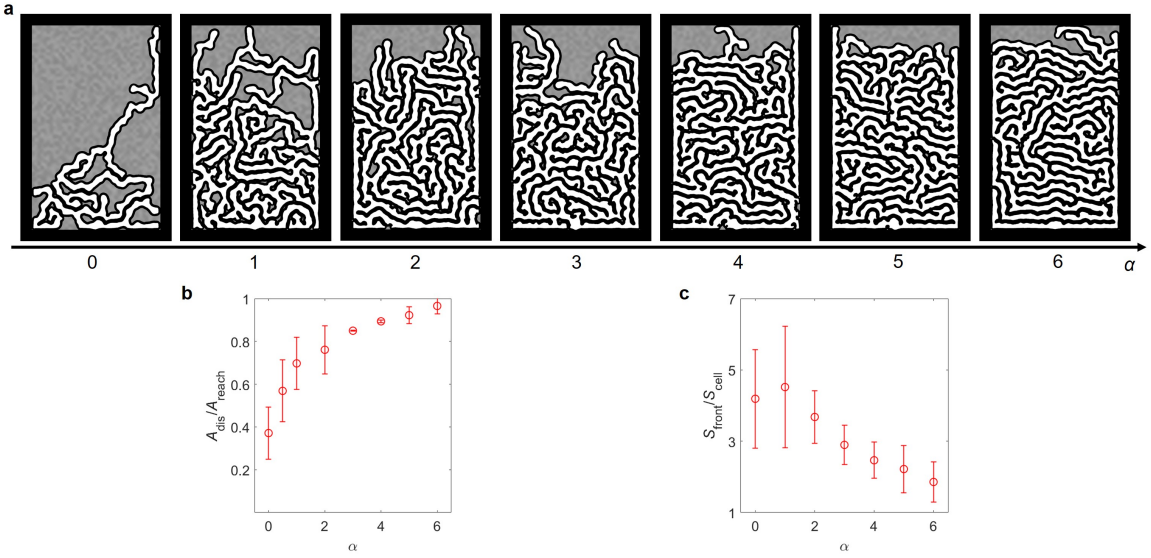

Fig. 5.14 (a) Patterns formed at different α. (b) Compactness c and (c) Instability ration s as a function of α. The black frames are the boundaries of the cell, finger will turn back if it hits to the boundary.

component along the cell of the gravitational force of the invading liquid points to the opposite side of the inlet, providing a force for finger growth. Omit the effect of gravitational

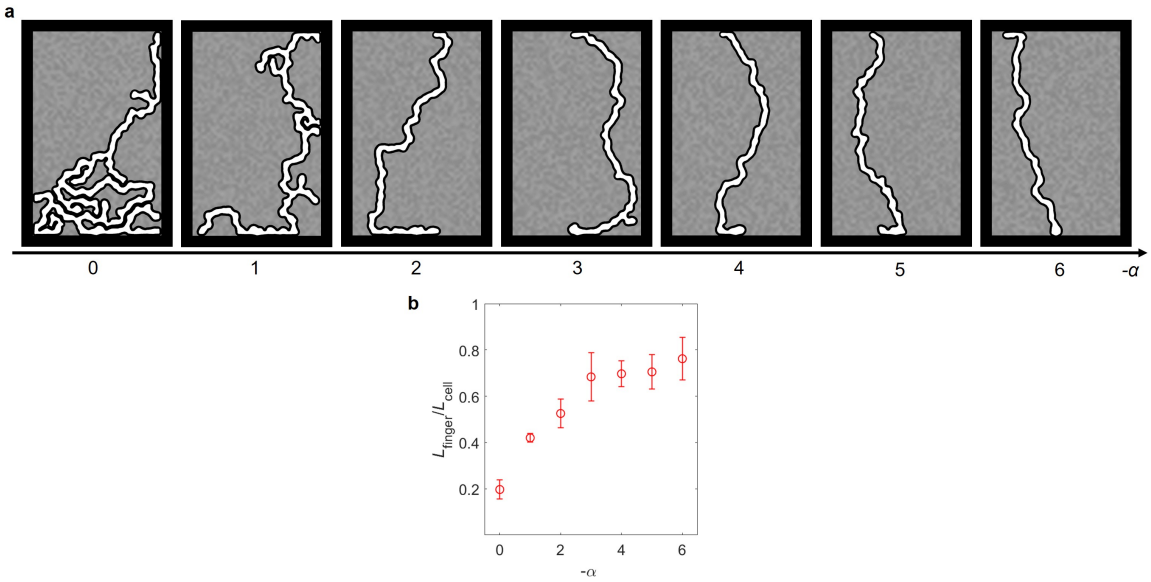

Fig. 5.15 Patterns formed at different tilt angle -α. (b) Directionality of the finger d_f as a function of -α. All panels: $\varphi = 0.5$, and the dimension is 20×30 cm (including the black frames). The black frames are the boundaries of the cell, finger will turn back if it hits to the boundary.

force of the beads, pressure on the finger tip needed for finger growth, $P_t^{'}$, now may be written:

$$P_t^{'} = P_t + \rho g y \sin\alpha = \sigma_0 \frac{R}{b} \frac{\varphi}{1-\varphi} + \frac{\gamma}{R} + \rho g y \sin\alpha \tag{5.6}$$

According to the equation above, at $\alpha > 0$, the finger is more likely to grow along the lower region in the cell to minimize the pressure needed to move the front forward. This preference can be disturbed by local particle arrangement (noise in the simulation) which results in imperfect horizontal alignment of the finger body. At higher α because higher α causes a larger $P_t^{'}$ difference at different y, hence this disturbance becomes less significant compared to $P_t^{'}$ difference and the horizontal alignment becomes more obvious. At $\alpha < 0$, to minimize the work in the system, the finger choose the easiest way to advance — head over to the lower region in the cell. This trend becomes more obvious at higher (-α) also because of the increase of $P_t^{'}$ difference at different y. Note that the finger width $2R$ in the tilted cell is the same as that in a horizontally placed cell in the simulations.

5.5 Conclusion

We have experimentally and numerically studied the stabilising effect of three separate mechanisms: viscous pressure gradients, gap gradients, and elevation gradients in gravity. A linear Hele-Shaw cell with three boundaries is used. By increasing the viscosity of the invading fluid, a transition from unstable invasion front to stable front is achieved similar to the results for the radial cell in the previous chapters. The increase of the viscosity η causes a larger D_{visc} and the number of instantaneously growing fingers increases to the point where the entire cell width is occupied, and the fingers grow on a level front. Once the available width is occupied, a further increase in D_{visc} causes an increase in the number of fingers by squeezing the finger width as seen by the decreasing 2R as function of D_{visc} (Fig. 5.4 d).

The effect of the plate spacing b on the finger width is verified by the experiment and the simulation, i.e., the finger width increases as b increases as described in Equation 5.5. The effect of the gap gradient db/dy on finger alignment is studied. At $db/dy < 0$, the fluid invades from a wider spacing to a narrower spacing, the finger tends to grow sideways and preferentially occupy the large gap region. The pattern is stabilised and made more compact by the increased frictional resistance associated with a narrowing gap. A finger that grows from a narrow gap towards a larger gap will experience a lower frictional resistance in the direction of growth and hence grow preferentially along the increasing gap gradient towards the edge with the highest gap spacing.

The effect of the tilt angle α has also been studied with numerical simulations. The patterns formed at $\alpha > 0$ is very similar to when $db/dy < 0$, and the patterns formed at $\alpha < 0$ is very similar to when $db/dy > 0$, but the principles behind are different. The gap gradient db/dy changes the friction at different regions in the cell while the tilted cell adds an extra gravitational force to the system, both mechanisms contributing to the stress the finger needs to overcome to grow. In this study, the invading fluid has the higher density (mirroring the experiments with injection of water/glycerol into dry hydrophobic layers), and with the injection at the base of the cell, the invasion is stabilised in a similar manner to that discussed by Eriksen *et al*. [26], while the injection of dense fluid from the top cause a gravitationally unstable sinking of the invading finger, it's path made more tortuous by the frictional noise it experiences along the way.

Chapter 6

From capillary fracturing to blasting in wet granular packing

6.1 Introduction

Air invasion into very dense packings of grains, still deformable, but not possible to bulldoze long distances to create fingers, is referred as to capillary fracturing [36]. Capillary fracturing is formed when the capillary forces overcome the frictional strength of the material. Chevalier *et al.* increased the volume fraction ϕ of the granular packing to 0.55 and observed capillary fracturing [31]. Holtzman *et al.* described a transition from fingering to capillary fracturing by changing the confining force exerted on the glass beads [36].

We here develop an experimental system to investigate capillary fracturing by air injection at much higher pressures than in previous studies [32–35, 27, 28]. The fracturing patterns are sensitive to changes in injection pressure and packing fraction of the granular bed. We also discuss effects of air pressure and plate spacing on the pattern formation. The studies in this chapter are within (+W, $+\mathcal{M}$) quadrant as shown in Figure 5.1.

6.2 Methodology

A new Hele-Shaw setup and filling method was developed for this study. Because granular materials are prone to sedimentation, erosion, segragation and pattern formation, it can be challenging to achieve the uniform initial filling of the cell which is required for controlled experiments. Here we use a new strategy of injecting water through a grain-filled hopper such that the fluid-driven grain-flow eventually fills the cell. A semi-permeable outer boundary allows fluid to exit while containing the grains in the cell. The boundary is made of a strip of

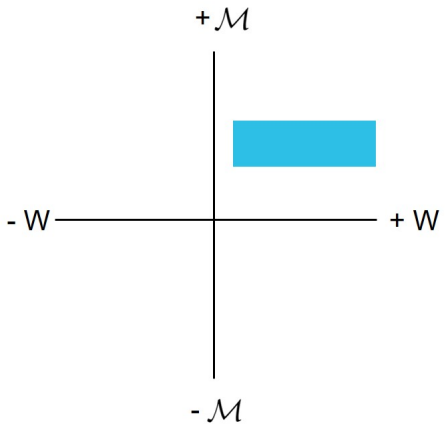

Fig. 6.1 Quadrantal diagram of viscosity ratio $\mathcal{M}$ and wettability $\mathrm{W} = -\cos\theta$ to show the study focus of Chapter 6

foam glued to the bottom plate in a circle with inner diameter 27.5 cm, centered on the inlet. Spacers with the thickness of 0.60, 0.75 and 0.90 mm at different experiments were put on the corners of the bottom plate. The two plates were then clamped together.

For the filling process, a large syringe (Labelled A in Fig. 6.2 a) is mounted directly above the inlet of the cell, connected by a short piece of tubing. This syringe is filled with water and a bed of sedimented grains, and acts as a silo/hopper for the filling. Grains are settled in syringe A and finally reach the steady state. To maintain this steady state before packing preparation, we fixed syringe A vertically to the cell and through a hole in the top of syringe A, water is injected from another syringe B mounted on a syringe pump. The water flow, assisted by gravity, forces into the cell a dense mixture of water/grains, which spreads out in a circular shape until the grains come in contact with the foam boundary. Now a gradual compaction process follows, where the grain bed in the cell compactifies with continued injection. A certain control of the spatial uniformity and final filling fraction can be achieved by varying the imposed flow rate and the length of time the flow is maintained to compactify the packing, however the method has limitations in terms of the range of filling fractions that can be achieved, and problems with non-uniformity can still persist. After many trial-and-error studies, a flow rate of 10 ml/min was chosen to produce the most uniform beds, with the time (total injected volume) varied to produce different filling fractions within a limited range. The grains were glass beads sieved to a diameter range of 75 - 100 um.

After the filling procedure was completed, the silo syringe was removed, and the inlet was then connected up to a container with pressurised air. The container had been pressurised using an inflator (a bicycle pump). Air pressures used in this study ranged from 0.07 to 3 bar.

The experiments commenced by rapid opening of a valve to let the pressurised air enter the cell at the central inlet.

The volume of the container was approximately 1 L which is large compared to the internal volume of the cell (≈ 50 cm^3 at the largest gap size), with the volume displaced during the course of an experiment smaller still. We therefore make the assumption that the pressure decrease because of air expansion has negligible effect during an experiment. That is not to say that the pressure is everywhere equal to the reservoir pressure: there can be a significant pressure drop associated with the air flow through the very narrow fractures.

Initial experiments with different filling fractions reported in the next section were conducted using a syringe pump instead of the pressure reservoir. This allowed the fracturing process to be characterised at low pressure and constant injection rate similar to previous studies [27, 28], before moving on to experiments investigating higher pressures.

The cell was backlit using a white LED board. The experiment process was filmed using a high-speed camera (Photron Fastcam 1024-PCI). The camera had a resolution of 1024×1024 and a highest frame rate of 1000 fps. The longest experiment lasted for 2 min and the shortest experiment lasted for 0.06 s.

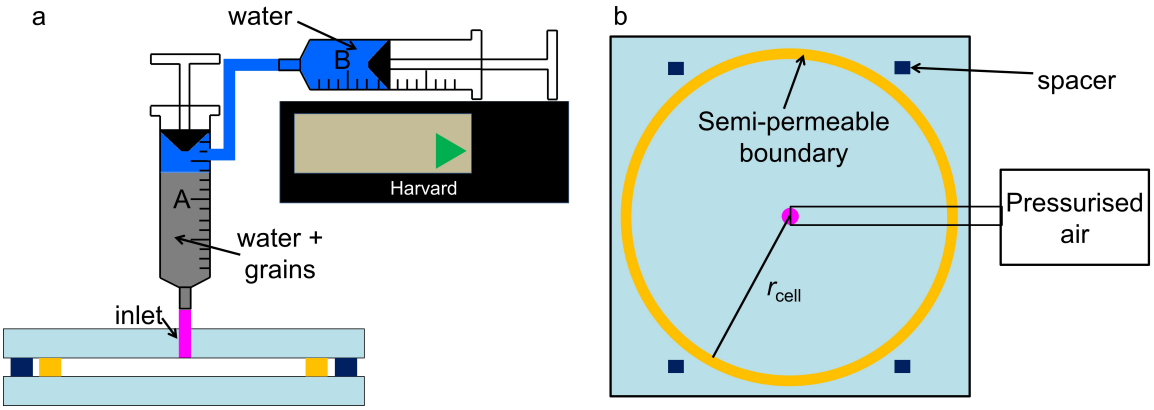

Fig. 6.2 Illustration of the setup for fracturing experiments. (a) Preparation of granular packing. Water in syringe B was pushed into syringe A thereby pushing mixture of water and beads in syringe A into the cell. (b) Top view of the experimental setup. The inner radius of the granular packing confined by the semi-permeable boundary $r_{\text{cell}} = 13.75$ cm.

6.3 Results and discussion

6.3.1 Effect of granular bed volume fraction

The filling process of the grain-water mixture affects the volume fraction and hence the patterns formed. In practice, after the injection of a total volume of 44 mL, the mixture of the grains and the liquid was able to fill the whole region inside the boundary, and a volume fraction $\phi \approx 0.53$ of the packing was achieved. If 48 or 52 mL water was injected, a volume fraction $\phi \approx 0.55$ or ≈ 0.58 of the packing was achieved.

Allowing the pumping to continue even after the mixture had reached the edge cause a gradual compaction of the granular bed, with excess water exiting through the foam boundary. An injection volume of 48 mL produced a filling fraction phi = 0.55 ± 0.01, and an injection volume of 52 mL produced phi = 0.58 ± 0.01. ϕ was obtained after the experiment. The mixture was collected and dried, the actual volume of the grains V_{grain} was calculated by measured mass over the density of the material. The total volume of the mixture $V_{\text{total}} = A_{\text{cell}}b$, where A_{cell} is the area inside the boundary, b is the gap between the plates. Later ϕ was calculated by $V_{\text{grain}}/V_{\text{total}}$.

Figure 6.3 shows the patterns formed after slow air injection at 0.01 mL/min into the granular packings of different ϕ, demonstrating that a small change on ϕ can cause a very different pattern. At $\phi = 0.53$, the fractures appear as white channels, this means the fractures are fully opened to enable the light from the panel above the cell to pass through to the camera placed beneath the cell. At $\phi = 0.55$, the fractures appear darker than the surrounding granular packing, the fractures are not fully opened and direct light is not able to pass unhindered through.

The experiment at the highest ϕ tested here, $\phi = 0.58$ (Fig. 6.3 c), produced a very different pattern. The invasion started with partially opened, narrow fractures (dark appearance), similar to in Fig. 6.3 b. The fractures were followed by a secondary process visible as a darkening of the material inbetween fractures. This is caused by air invading the pore space between the grains, displacing the defending fluid (water).

In Holtzman *et al.* [36], the authors achieved a transition from capillary fracturing to pore invasion by applying force on the water-grain packing. This transition is explained by the competition between the force provided by the invading air meniscus and the mechanical forces of the packing itself. If the frictional forces exceeds the force provided by the air meniscus, then the capillary forces are not able to move the grains, and pore invasion occurs once the pore invasion threshold has been passed. In the opposite case, when the frictional strength is lower than the capillary pressure, then the meniscus can deform the packing and open up fractures.

The experiments with different ϕ presented here all produce fractures, meaning that the initial material is packed loose enough that the invading air/water meniscus is able to overcome friction and deform the packing. Higher ϕ constrains the amount of deformation, producing narrower fractures. At the highest ϕ, the fracturing process has compacted all the material close to the inlet producing a higher frictional strength which exceeds the pore invasion pressure. Now it is easier to invade the pore space compared to deforming the hardened packing. In the experiment here, ϕ is directly varied by the filling process and the similar results are achieved. In the study below, we will use $\phi = 0.55$ to study the fracturing in different circumstances.

6.3.2 Effect of air pressure

Figure 6.4 and Figure 6.11 b show the patterns formed after air invasion at air pressure P_{air} 0.07 to 3 bar. We observe three different invasion dynamics among these experiments: partially-opened fracturing, fully-opened fracturing, and fractures that keep widening. At P_{air} = 0.07 bar, the fractures are darker than the surrounding granular packing, the fractures are not fully opened and the back-lighting is not able to penetrate the fractures. Fully opened fractures (white channel in the image) start to appear at $P_{\text{air}} = 0.1$ bar as shown in Figure 6.11 b.

At $P_{\text{air}} \geq 0.2$ bar, fully-opened fracturing dominates the invading process. In the mean time, we observe a gradual widening of the existing fractures with the invasion of air. This phenomenon becomes even more clear as we increase the initial air pressure. At $P_{\text{air}} = 3$ bar, fractures initially propagate in a sweeping manner and followed by a "blast" forming an empty region close to the inlet.

To quantify the fracturing here, we define several characteristic parameters after the first branch of the fractures reaches the boundary: normalized radius $r_n = r_{\text{full}}/r_{\text{cell}}$ where r_{full} is the radius of fully-opened fracturing region and r_{cell} the inner radius of the boundary (shown is Figure 6.5), invaded area A_{inv}, all area within the boundary A_{cell}, fracture density $A_{\text{inv}}/A_{\text{cell}}$. We measure r_n and A_{inv}, and plot r_n and $A_{\text{inv}}/A_{\text{cell}}$ as a function of air pressure as shown in Figure 6.5.

In Figure 6.5 b, r_n increases with the increase of the air pressure P_{air} when $P_{\text{air}} \leq 0.2$ bar. Above 0.2 bar, r_n will keep at the same level. The fracture density $A_{\text{inv}}/A_{\text{cell}}$ increases with the increase of P_{air}, which means that the air tends to invade more completely at a higher pressure.

To characterise the gradual widening of fractures close to the inlet, we monitor the changes of grey level Δg_v of a selected region of interest (ROI) with time. The starting frame is chosen when the fractures within this region haven't become fully-opened. The

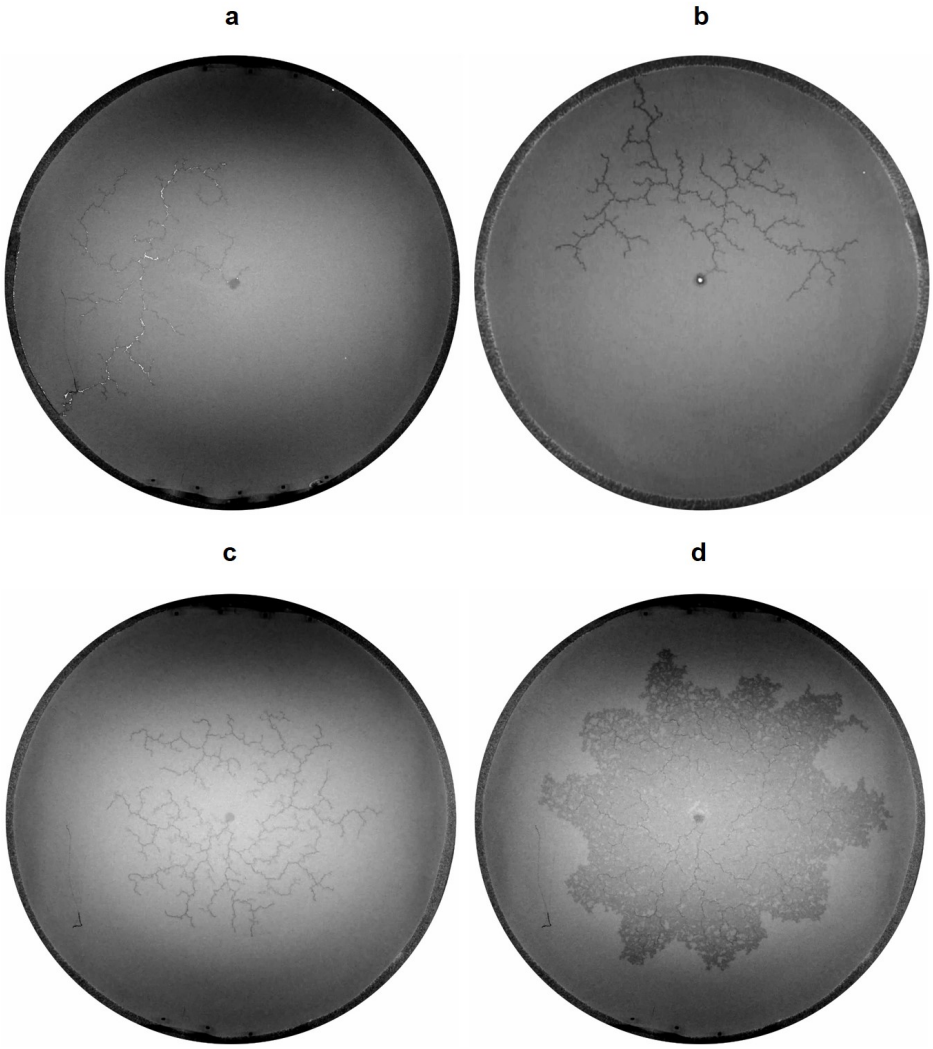

Fig. 6.3 Patterns formed after air invading the grain-liquid packing with different volume fraction ϕ (a) 0.53, (b) 0.55 and (c-d) 0.58. (c) is the early stage of the experimental results at $\phi = 0.5$ showing the fractures before the pore invasion, and (d) shows the final pattern of the fracturing followed by pore invasion. In all panels, the diameter inside the boundary is 27.5 cm, injection rate is 0.01 mL/min.

grey level indicates the brightness of the image. We use a white LED board as back-light in the experiment, which results in the empty area in the packing appearing white in the image. Corresponding to the grey level of the monitored region, higher grey level means more fully-opened fractures.

As seen in Figure 6.5 c, Δg_v shows a clear different trend at different P_{air}. The grey level remains more or less the same when $P_{\text{air}} \leq 0.1$ bar and Δg_v remains approximately 0 throughout the experiment. This means there is no widening happening in already formed fractures.

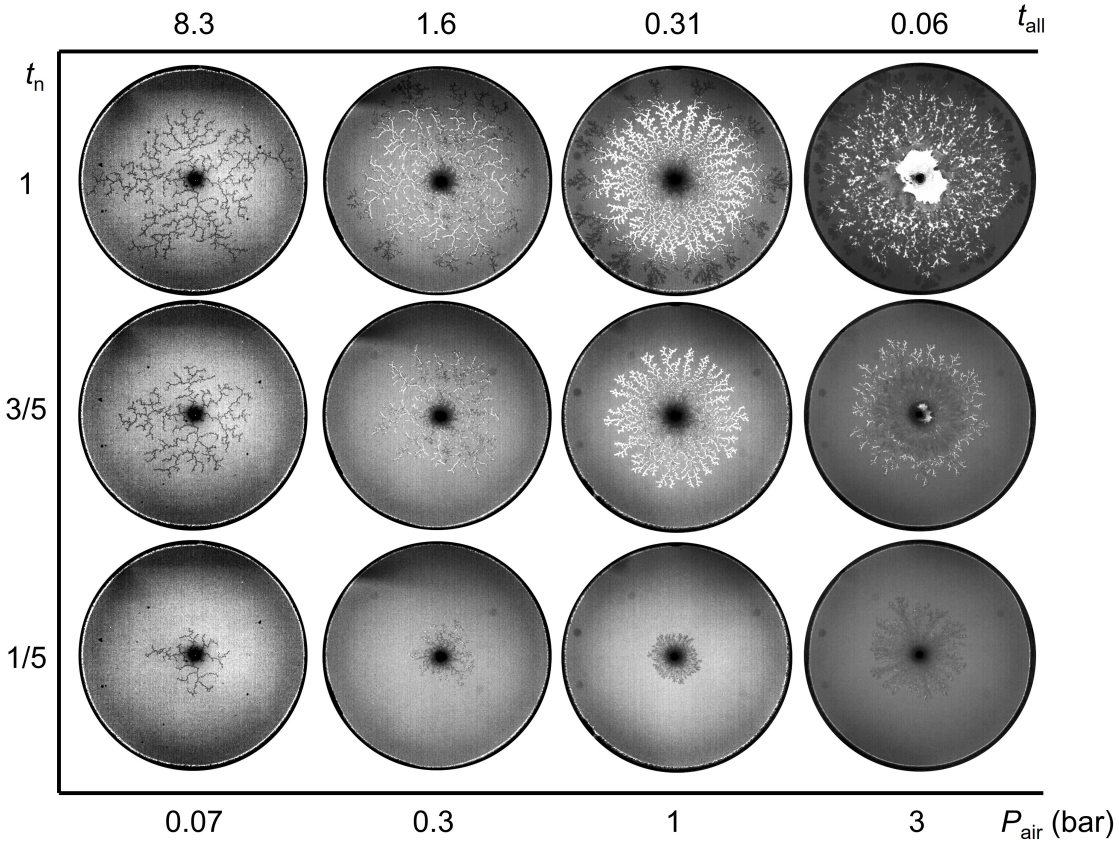

Fig. 6.4 Patterns formed at different stages t_n after air invading to granular packing at air pressure P_{air} 0.07 bar, 0.3 bar, 1 bar and 3 bar. $t_n = t/t_{all}$ is a nornalized time where t is the real time over the period of pattern formation and t_{all} is the whole time of pattern formation within the experiment system.

At P_{air} 0.3 and 0.4 bar, the grey level shows a clear increase with time, which means some of the fractures within the monitored region are widened and become fully opened with time. At P_{air} 0.5 and 1 bar, the grey level in the ROI decreases with time. However, one can actually observe a widening of the fracture with time by eyes in Figure 6.4 e and f. This may be because there are more fractures branched in the center region with time. New fractures can cause a decrease of the grey level and if this decrease contributes more to the changes of grey level than the widening of the fracture, the overall grey level will decrease with time.

At the highest pressures studied here, we observe a clear darker ring (compaction zone) forming behind the fracture front (green ring in Figure 6.8). This is caused by a displacement of the material by the high pressure air after the initial fracturing. At P_{air} below 3 bar there are sometimes small-scale secondary displacements but not to a significant extent, and it has little effect on the patterns formed. At P_{air} 3 bar, this subsequent displacement becomes

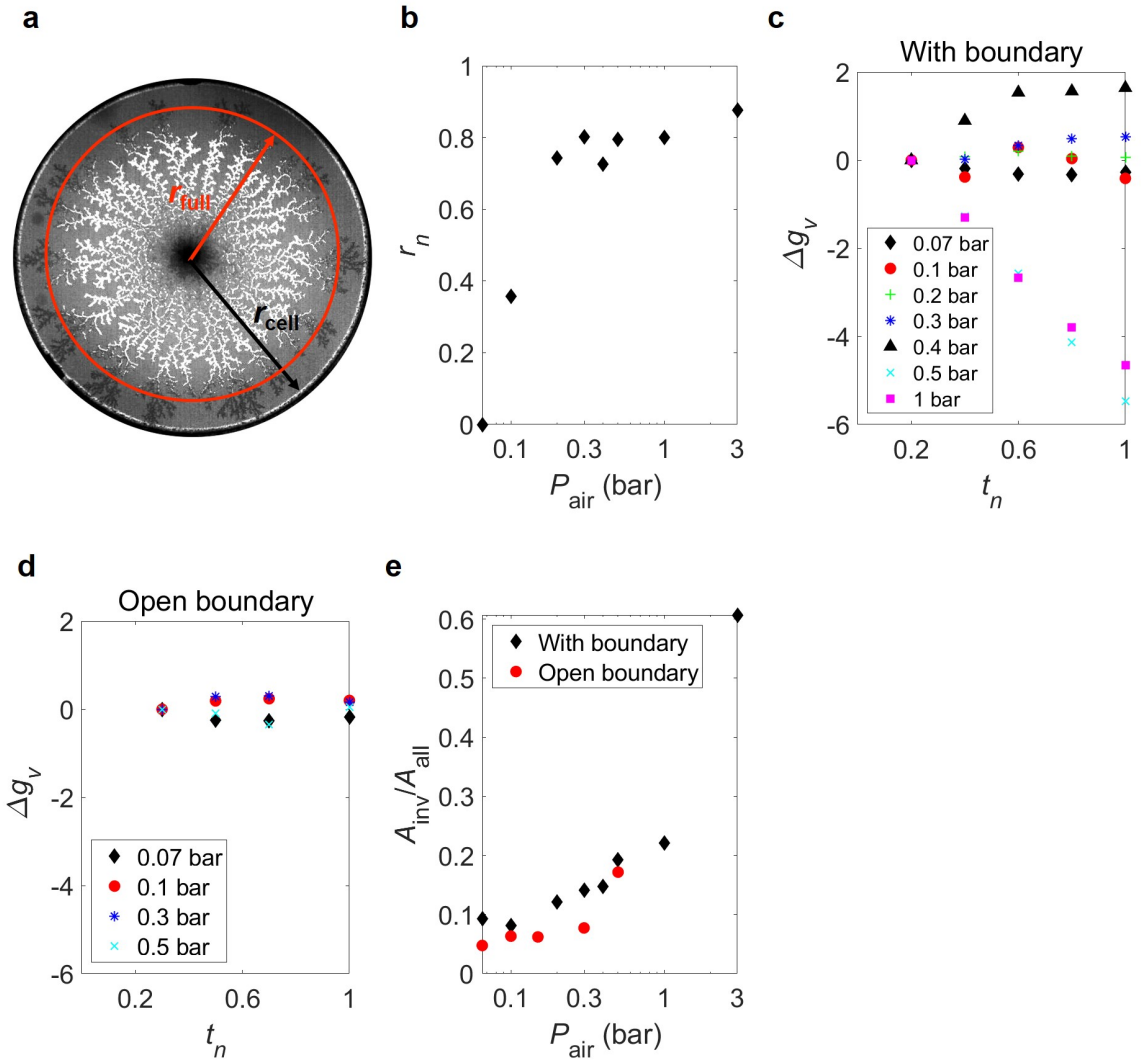

Fig. 6.5 (a) Illustration of radius of fully-opened fracturing region r_{full} and radius of the granular packing r_{cell}. (b) Relationship between normalized radius $r_n = r_{\text{full}}/r_{\text{cell}}$, and air pressure P_{air} in with-boundary experiments. X-axis is in log scale for better visualization. Grey level changes Δg_v at different stages t_n and different P_{air} of the with-boundary experiments (c) and the open-boundary experiments (d). (e) Relationship between fracture density $A_{\text{inv}}/A_{\text{cell}}$ and air pressure.

significant and causes the formation of a cavitation zone. The highly-compressed air blows the mixture of granular beads and water away from the center after the initial fracturing, caving the center area by the following air. The grey level decreases first and then increases dramatically.

Campbell *et al.* [28] studied the gas-driven fracturing at different injection rates Q and used the fracture density D to illustrate the patterns formed. They found a self-avoiding

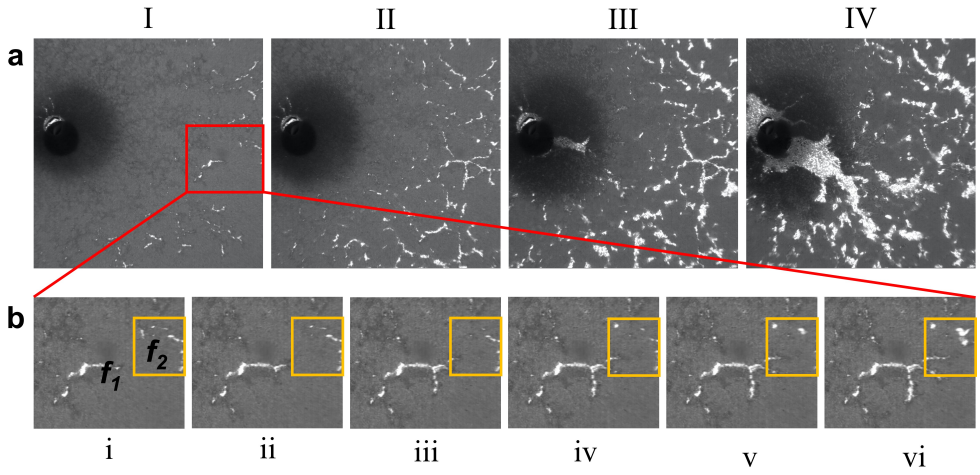

Fig. 6.6 (a) Close-up images of air invasion at different time stages I–IV. (b) Processes i–vi of the elimination of the existing fracture. P_{air} = 1 bar in all the panels.

nature of the fracture network at low Q before the granular packing was fluidized. This self-avoiding phenomenon was caused by the resistance from the compaction front of the existing fracture. The width of the compaction front here was determined by the property of the packing itself, thereby almost the same fracture density was observed at different Q that could not fluidize the packing. After Q larger than the critical fluidization injection rate, the granular packing is fluidized and this resistance becomes smaller, causing an increase of D with Q. However, even at the maximum injection rate (Q = 100 mL/min), the fracture patterns remained static once formed, and there was no reorganisation or subsequent deformation of the fractured zone.

In the current study, we start the experiment at an air pressure 0.07 bar which is close to the peak pressure at Q = 100 mL/min and similar experimental results are observed. At $P_{\text{air}} > 0.1$ bar, we observe a new phenomenon — the elimination of existing fractures with air invasion. Figure 6.6 a shows the close-up images of fracture growth. Initially the "competition" between the fractures are small because there is enough space for them to grow. Later, new fractures nucleate behind, causing deformation of the already fractured material and the elimination of the existing fractures. Figure 6.6 b shows how a fracture (f_2) is eliminated by another (f_1). f_1 moves towards f_2 pushing forward the grain/liquid between them, fracture body of f_2 is gradually squeezed and finally closes up.

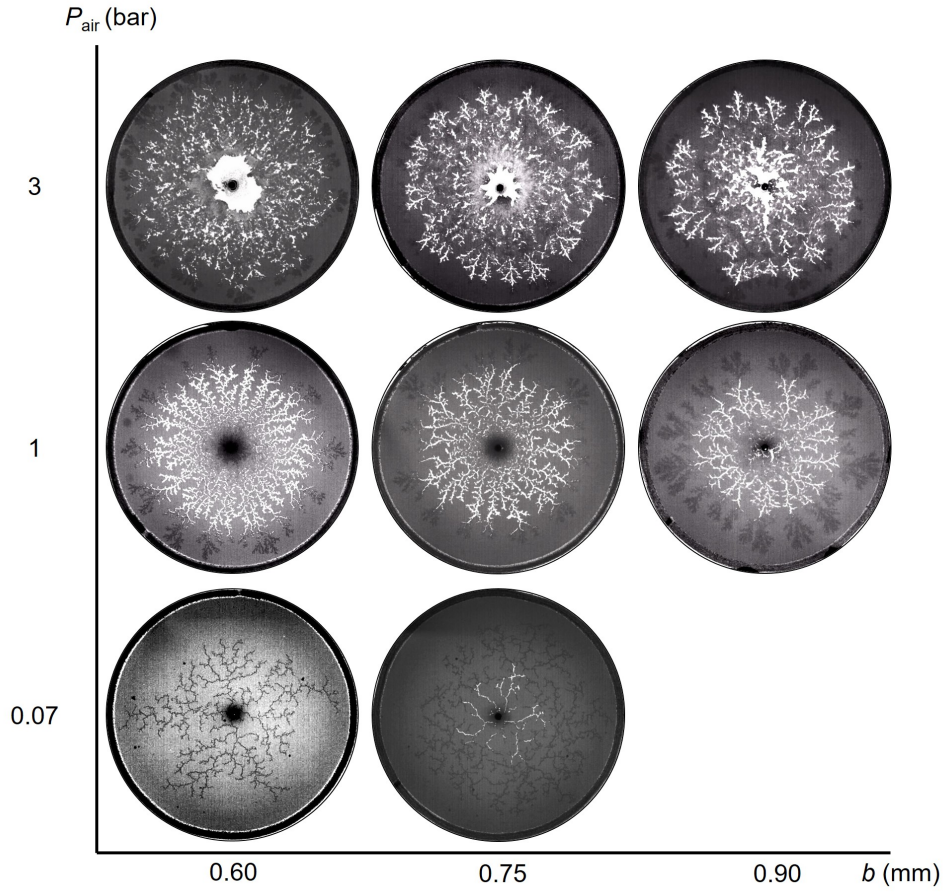

Fig. 6.7 Air invasion patterns at different plate spacing b and air pressure P_{air}.

6.3.3 Effect of plate spacing

We have also studied the effect of plate spacing b on pattern formation. Figure 6.7 shows the patterns formed by air invasion at different b and air pressure P_{air}. In Chapter 5, the effect of plate spacing on frictional fingers were studied, and it was found that larger b produced wider fingers because of the relative decrease in friction. Although the granular packing has been fluidized in all the experiments here and a fixed compaction front with certain width does not exist, differences in patterns formed at different b are clear to observe.

In Figure 6.7, At $P_{air} = 0.07$ bar, the fractures are shown as partially opened in $b = 0.60$ mm, and the fully-opened fractures start to occur in the center area in $b = 0.75$ mm. At $P_{air} = 1$ bar, fully-opened fractures occur in the central region in all the cases here. We also observe a clear decrease of r_n at larger b as shown in Figure 6.9 a.

At $P_{air} = 3$ bar, the area of cavitation zone (white region in the pictures) in the packing center shows a clear decrease with the increase of b. The secondary displacement of granular materials by the air becomes significant on patterns formed only at $P_{air} = 3$ bar, we subtract

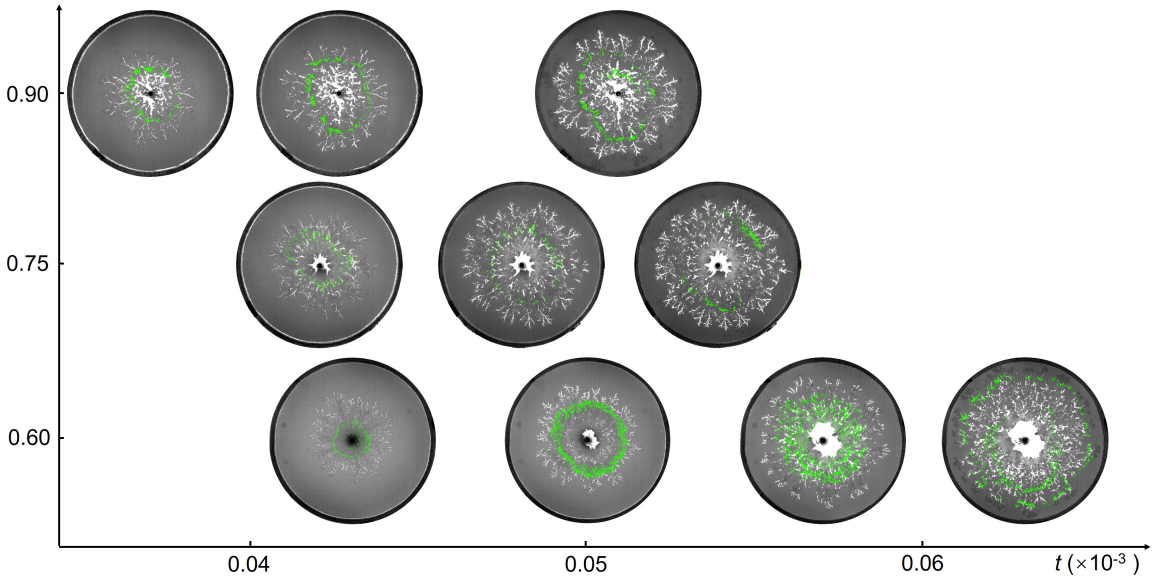

Fig. 6.8 Time evolution of air invasion patterns at different plate spacing b at P_{air} = 3 bar.

the pictures of invasion patterns at four stages before air breaks through the boundary and get the evolution of the compaction zones (green ring in Figure 6.8) caused by the secondary displacements. To quantify the scale of the secondary displacement, we define another normalized radius for the compaction zone $r_{nc} = r_{\text{comp}}/r_{\text{cell}}$ where r_{comp} is the maximum radius of the compaction zone.The normalized radius r_{nc} increases with time at most of the cases. At higher b, the secondary displacement seems to occur earlier and the invading front reaches the boundary earlier. The compaction zone caused by the secondary displacement becomes smaller at higher b. One of the reason for these phenomena is the friction stress from the granular packing becomes smaller at higher b, and air is easier to move ahead than pushing the beads behind the invasion tips. In addition, larger b provides more spaces for the decompression of air, the pressure of the invasion air drops faster and becomes insufficient for large scale of secondary displacement.

6.3.4 Effect of boundary

In the study above, the experiments were performed with the granular packing confined by a semi-permeable boundary. The following results were obtained with the boundary removed after the filling of the grain/liquid mixture was finished. Figure 6.10 shows the time evolution of air invasion at different air pressure. The main difference compared to the with-boundary experiments is that the fully-opened fractures occur in all cases and become wider in the region closer to the packing edge instead of in the center region. The partially-opened

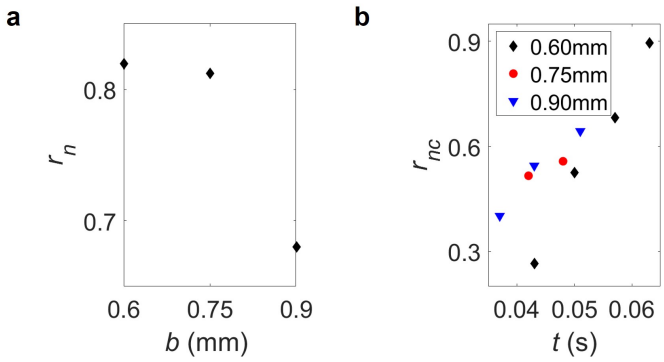

Fig. 6.9 (a) r_n as a function of b and $P_{\text{air}} = 1$ bar. (b) Time evolution of r_{nc} at different b.

fractures are only observed in the center region of the packing and fewer at high-pressure experiments.

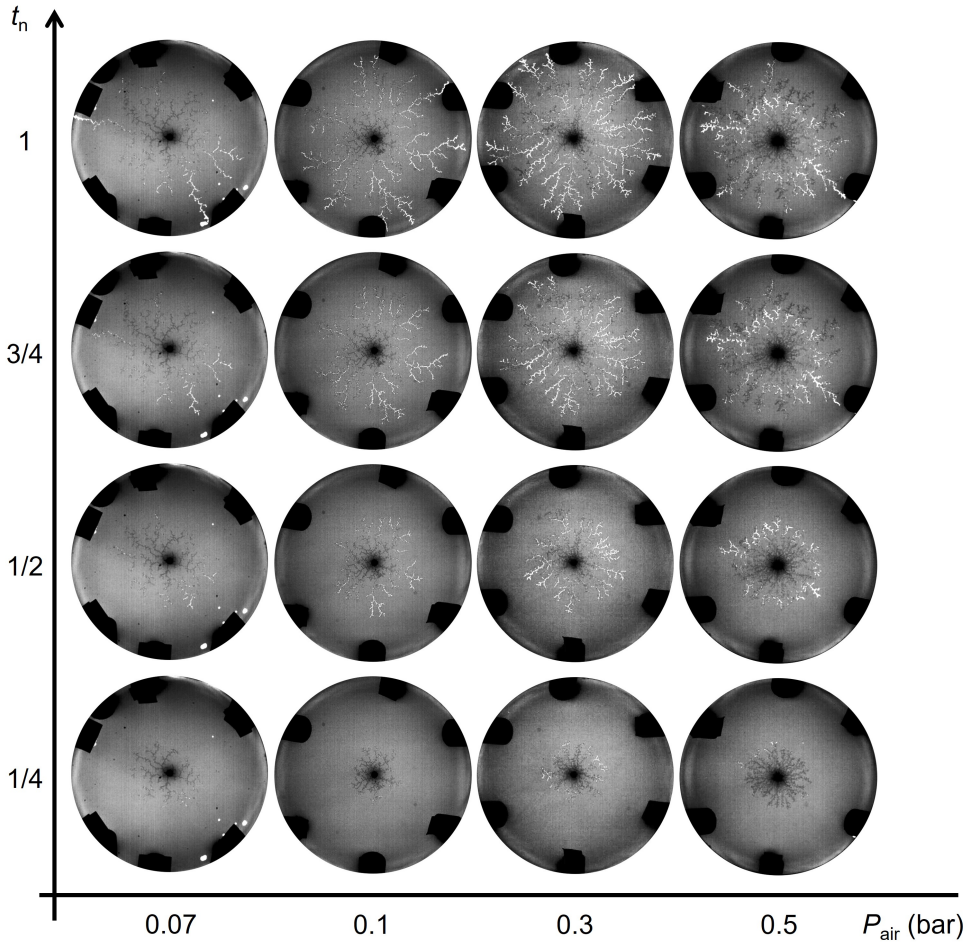

Fig. 6.10 Time evolution of air invasion into the granular packing open boundary at different air pressure P_{air}.

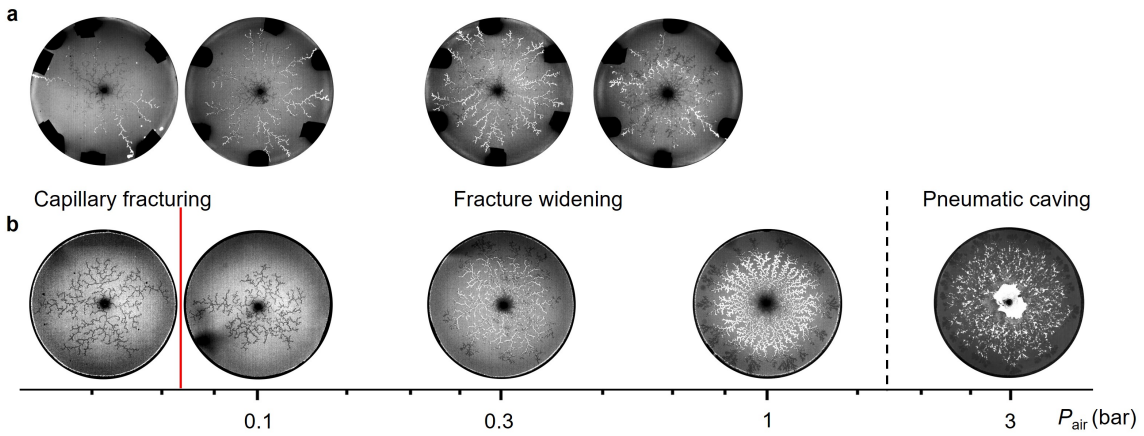

Fig. 6.11 Pattern comparison in (a) open- and (b) with-boundary experiments at different air pressure. The red line in (b) distinguishes the capillary fracturing and the fracture widening, the black line distinguishes the pneumatic caving caused by a dramatic secondary displacement of the granular materials by the air. Figure a and b share the same axis of P_{air}.

With an open boundary, the grains are not held back at the perimeter of the cell, and the invading air set up a flow that pushes material outwards, leaving more space for widening of fractures. At P_{air} 0.07 bar, there are partially-opened fractures occurring in the center region, but their branches expand in the region closer to the packing edge and become fully-opened (Figure 6.11 a), unlike the situation in with-boundary experiments (Figure 6.11 b). The region closer to the packing edge is easier to be fluidized than the inner region, because the force chains between the particles resist the fluidization of the packing and this resistance becomes much smaller in region close to the open edge. At higher pressure, the granular packing is fludized further, thereby the fully-opened fractures are able to occur early in the center region.

Figure 6.11 shows the patterns formed in with- and open-boundary experiments at different P_{air}. Figure 6.5 c and d compare the grey level changes with time of the with- and open-boundary experiments at different pressure. The grey level almost has no change with time in with-out boundary experiments, which means there may be no widening of the fractures happened, while the grey level changes a lot in most of the cases of with-boundary experiments as has been described before. The process of the fracture widening is the process of pushing the compaction front between the fractures further, which is much harder than pushing the looser region ahead of the invasion front, thereby the air choose to move forward instead of widening the fracture.

6.4 Conclusion

We have experimentally studied capillary fracturing of a water-saturated granular packing by pressurised air. The effects of filling fraction, pressure, bounndary conditions and plate spacing are investigated. The capillary fracturing described in [36] is identified as partially-opened fracturing, and is achieved at the volume fraction $\phi = 0.55$ in the current study. At slightly smaller $\phi = 0.53$, fully-opened fracturing is observed, and at slightly larger ϕ 0.58, capillary invasion after the fracturing is observed. We observe a clear darker ring (compaction zone) formed by the subsequent displacement of the air at higher pressure. The patterns formed at different pressures are different and can be divided into three phases: capillary fracturing, fracture widening, and pneumatic caving. In the experiments with larger plate spacing b, we observe a transition from partially-opened fracturing to fully-opened fracturing at lower pressure, and a reduction of the caving at higher pressure. The boundary also plays a significant role in pattern formation, more fully-opened fracturing is observed because the granular packing becomes easier to be fluidized in this case.

Chapter 7

Frictional flow patterns in repelling, imbibing and mixed-wet granular material

Wettability of a solid surface, quantified by the contact angle, governs many phenomena in both nature and industry. A water-repellent, or hydrophobic, surface such as a lotus leaf [48] has a contact angle larger than 90° (measured within the water phase at the triple line), the water therefore beads and rolls off the surface. Hydrophilic surfaces attract water and produce contact angles smaller than 90°. Self-cleaning textiles based on either hydrophobic or hydrophilic approaches have been studied widely [49]. Water-repellent soil received extensive attention because of its hazards to erosion and plant growth [50]. Fluid-fluid displacements governed by wettability have been universally studied in the fields of CO_2 storage [3–5] and oil recovery [6, 7].

Hydrophobic and hydrophilic regions generally co-exist in porous media. Ahmed *et al.* identified a broad distribution of contact angles in porous media using X-ray tomography [75]. The relationship between the wettability and surface roughness has also been investigated. Amir *et al.* used direct numerical simulations to discover effects of the heterogeneous wettability on fluid displacement in porous media [76]. Kamaljit *et al.* measured the conductance of oil in oil-wet corners of the mixed-wet porous media during brine flooding [77], in contrast to the disconnected oil ganglia in pure water-wet systems [78]. Invasion patterns in mixed-wet porous media different to what has observed in pure water-wet (immbibition) and water-repellent (drainage) systems has been discovered by Scanziani *et al.* [79]. Using X-ray imaging, they observed a phenomenon of interface pinning which prevented the interface recession and snap-off during the invading process.

In the previous chapters, we have studied the multiphase frictional flows in the viscously stable and unstable situations yet all in the drainage regime. Here we develop a system where water displaces a granular packing varying from heterogeneously to homogeneously wetted and from water-wet to water-repellent. The system is controlled by the "viscous deformability" D_{visc}, "capillary deformability" D_{cap} and friction strength G. Three basic invasion processes are observed: pore invasion, capillary bulldozing and erosion. These occurs individually, simultaneously or sequentially. The studies in this chapter are within ($-$W to $+$W, $-\mathcal{M}$) quadrants as shown in Figure 5.1.

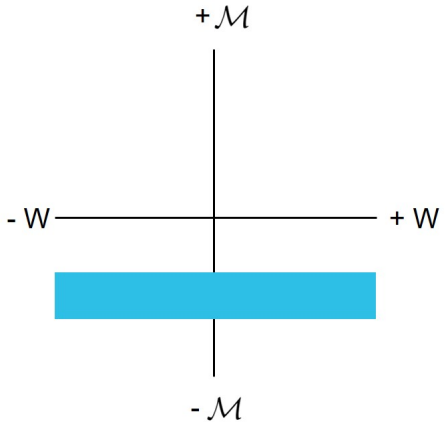

Fig. 7.1 Quadrantal diagram of viscosity ratio $\mathcal{M}$ and wettability $\text{W} = -\cos\theta$ to show the study focus of Chapter 7

7.1 Methodology

Our Hele-Shaw cell comprises two 1.5 cm thick glass plates, both top and bottom plates measuring 40×40 cm. A 6 mm diameter hole was drilled through the centre of the top plate to provide an inlet. Water or water/glycerol was injected through this inlet to displace a layer of dry grains. The inward facing surfaces of both plates were treated with silanization solution to render them hydrophobic. Otherwise, if left hydrophilic, the water/glycerol would preferentially invade along the surface of the top plate.

The plate silanization and grain preparation procedures were the same as described in Chapter 3. Both the hydrophilic beads and hydrophobic beads with diameter 75–100 μm were used in the current study. The pure hydrophilic beads, pure hydrophobic beads and mixtures of the two types were prepared for the experiment. We here use $C_b = M_{\text{hydrophobic}}/M_{\text{total}}$ where $M_{\text{hydrophobic}}$ is the mass of the hydrophobic beads in the mixture and M_{total} is the total mass of the mixture, to represent the proportion of hydrophobic beads in the packing, that is

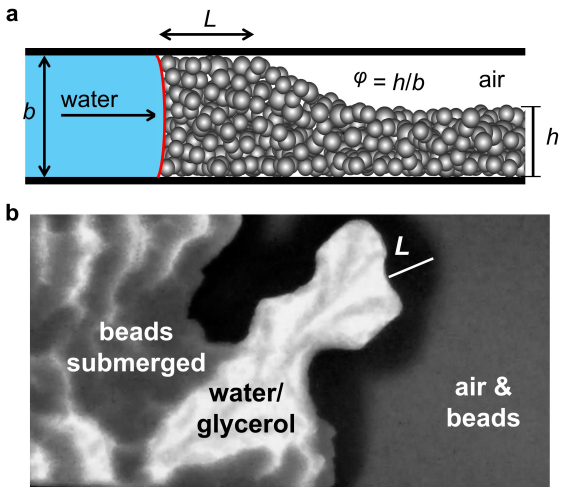

Fig. 7.2 Schematic side view of an invading fluid interface. The water meniscus bulldozes the grains, forming a compaction front of thickness L. The filling level φ is defined as the ratio of initial granular layer thickness h to cell gap thickness b. (b) Photographic top view of the invading channel. The white region has been invaded with water, while the black region (the compaction front) has been completely filled with grains. The ripples behind the air-water interface are the compaction front penetrated by water.

to say $C_b = 0$ represents pure hydrophilic beads, $C_b = 1$ represents pure hydrophobic beads, and the values between 0 and 1 represents the mixture. Note that $C_b = 0$ and $C_b = 1$ both represent uniformly wetting beads (all hydrophilic or all hydrophobic respectively), while the in-between experiments have mixed-wet grains with both hydrophilic and hydrophibic grains mixed together. An alternative way to manipulate the wetting condition would have been to chemically treat batches of grains to alter the contact angle. Whether the overall wetting behavior is changed by the mixed-wet ratio (like in this study) or by a uniform change in contact angle, we expect to see a general transition from imbibition-type behaviour to drainage-type behaviour, although the details of the invasion dynamics might differ in important aspects.

The prepared beads were spread out on the bottom plate. In order to achieve a layer of uniform thickness, two strips of adhesive tape were placed along opposite sides of the bottom plate, and a straight-edged tool resting on both tape strips was used to scrape the granular material along the plate. The top plate was then put in place, separated from the bottom plate with 0.09 mm spacers, which were slightly higher than the strips of tape so as to produce a granular bed with filling level $\varphi < 1$. The cell was clamped together firmly after assembly to prevent the top plate from lifting. All four edges of the cell were left open to the atmosphere.

We injected water/glycerol mixture into the cell using a syringe pump (Harvard Scientific, PHD Ultra), maintaining a constant rate for each experiment, with flow rates tested here

ranging from 1 to 100 mL/min. The cell was backlit, such that invaded regions appeared bright and compacted regions dark (see Figure 7.2 and 7.3). Images and movies of the pattern formation were recorded using a Nikon 1 J2 and Z6 II digital cameras at 30 fps, while a Nikon 1 J4 camera fitted with a 60 mm macro lens recording between 120 and 1200 fps was used for close-up filming.

7.2 Results and discussion

7.2.1 Pattern regimes and spatiotemporal evolution

The experiments presented here range from frictional fingering in repellent media (wetting, similar to in Chapter 3), to water imbibition in hydrophilic beads. The back-lit images reveal the state of the granular packing and fluid: Areas that have been cleared of grains by a bulldozing meniscus are completely transparent and appear white in the images. The darkest, almost black, pixels in the images are typically the compaction fronts of bulldozed grains. These consist of dry grains filling the entire gap as illustrated in Fig. 7.2 a. The initial layer of dry material partially filling the gap appears gray. When water/glycerol imbibes into the packing, the index of refraction difference between the grains and the fluid is reduced such that less light is scattered, and the wet grains appear a lighter shade of gray.

The invasion patterns here are governed by viscous, friction and capillary forces. In Chapter 4, we defined the viscous deformability parameter D_{visc} that measures the strength of viscous forces relative to friction, $D_{\text{visc}} = \eta u/(Gd)$ where $G = \mu\rho g\varphi b$ describes the friction strength and where d is the mean grain diameter. As before we use $u = Q/(bw_c)$ where $w_c = 1$ cm is a nominal finger width which is close to the finger width in each experiment. We keep G constant using $\varphi = 0.64$ in all experiments while we vary the viscous forces the system is subjected to (Q and/or η_{inv}) across the full range of C_b. Low D_{visc} experiments were achieved by injecting water at low injection rates Q. Experiments at higher D_{visc} was achieved by increasing Q up to 100 mL/min which is the limit on the pump. Glycerol water solutions were used to increase the value of D_{visc} further, similar to the methodology used in Chapter 3.

We observe three basic invasion processes that occur individually, simultaneously or sequentially: pore invasion, capillary bulldozing and erosion. According to the type and order we categorize the invasion dynamics into five regimes: (I) pure pore invasion, (II) pure capillary bulldozing, (III) capillary bulldozing followed by pore invasion, pore invasion followed by erosion, and (V) capillary bulldozing followed by pore invasion and erosion. This classification scheme is focused on the grain-scale processes and whether the granular

bed is deformed by the fluid or not. On top of this we have the effect of increased viscous stabilisation with increasing D_{visc} as discussed in Chapters 3 and 4. The results are summarized in the $D_{\text{visc}} - C_b$ phase diagram in Fig. 7.3.

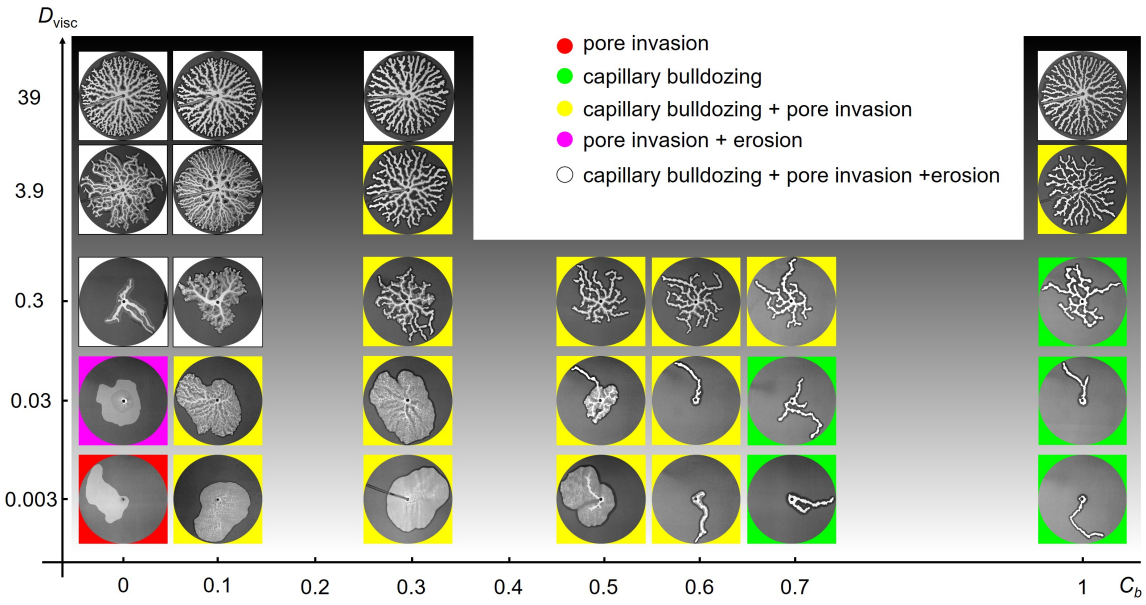

Fig. 7.3 Phase diagram of invasion patterns at different proportion of hydrophobic beads C_b and viscous deformability D_{visc}. The picture in lower-left corner with red background is regime I: pure pore invasion regime. The pictures with green background are within regime II: pure capillary bulldozing. The pictures with yellow background are within regime III: capillary bulldozing followed by pore invasion. The pictures with magenta background are within regime IV: pore invasion followed by erosion. The pictures with white background and black frame are within regime V: capillary bulldozing followed by pore invasion and erosion. The gradient background from white to black illustrates the increase of viscous effects on pattern formation. In all panels, $\varphi = 0.64$, the diameter of the circular packing is 26.8 cm.

Regime I: Pure pore invasion

Pure pore invasion only happens at $C_b = 0$ and the lowest water injection rate (Q = 1 mL/min, $D_{\text{visc}} = 0.003$) (see Figure 7.4 and the image in the lower left corner with red background in Figure 7.3). In this regime, the packing contains only hydrophilic beads, the water is pulled into the pore space by capillary action, and spontaneously imbibes the layer of hydrophilic grains. The creeping flow of the fluid in this case is not able to disturb the packing and the viscosity is not playing any role in the pattern formation.

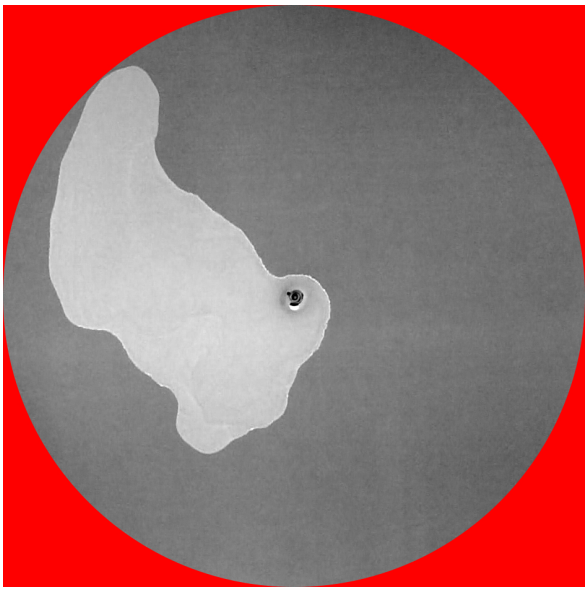

Fig. 7.4 Regime I: Pure pore invasion. Water imbibes into the layer of hydrophilic grains which is otherwise left undisturbed by the fluid flow. The water wet packing appears brighter than the dry packing since water/glass has a lower index of refraction difference compared to air/glass, reducing scattering in the back-lit cell. $C_b = 0$, $Q = 1$ mL/min, $D_{\text{visc}} = 0.003$ and $\varphi = 0.64$. The diameter of the circle is 26.8 cm.

Regime II: Pure capillary bulldozing

Pure capillary bulldozing occurs when the packing contains mostly hydrophobic beads and viscous pressure of the invading fluid has not exceeded the pore-enter pressure (see Figure 7.5 and the images with green background in Figure 7.3). The grains are wetted by the defending fluid (air) and repelled by the invading water/glycerol. The capillary forces exerted by the meniscus on the grains overcome friction and capillary bulldozing shapes the invading fluid into fingers. In this regime, the effect of increasing D_{visc} is to increase the viscous stabilisation resulting in the system transitioning from growth of a single finger to multi-fingering, and finally stabilised radial spoke patterns as described in Chapters 3 and 4.

Regime III: Capillary bulldozing followed by pore invasion

The images in Figure 7.7 and the panels with yellow background in Figure 7.3) are in Regime III: Pore invasion followed by capillary bulldozing. There are in principle two mechanisms that can lead to pore invasion: 1) The wetting condition reducing the pore entry pressure or even favouring spontaneous imbibition, and 2) The flow and associated viscous pressure gradient increasing the fluid pressure such that it overcomes the pore entry pressure regardless of the wetting state of the grains.

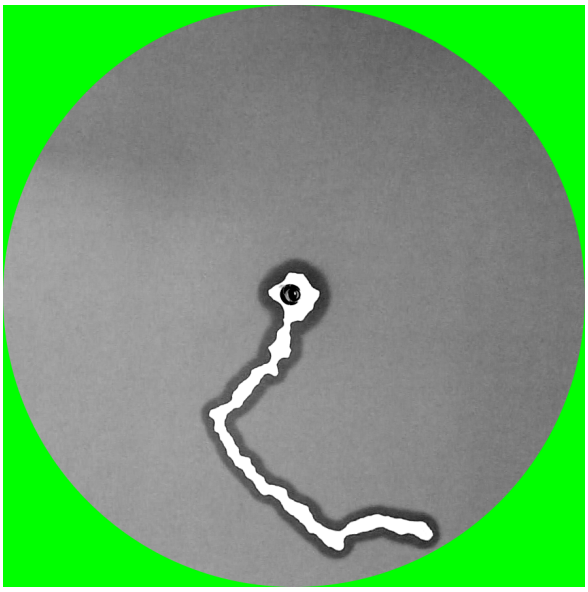

Fig. 7.5 Regime II: Pure capillary bulldozing. The invading fluid meniscus repels the grains and bulldozes up a compaction front of dry hydrophobic grains. $C_b = 1$, $Q = 1$ mL/min, $D_{\text{visc}} = 0.003$ and $\varphi = 0.64$. The diameter of the circle is 26.8 cm.

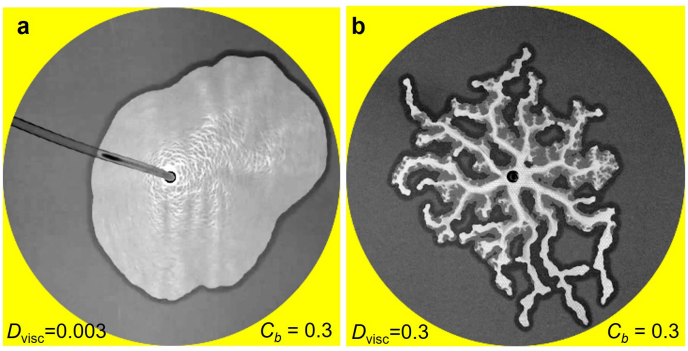

Fig. 7.6 Regime III: Bulldozing followed by pore invasion. (a) A small inclusion of hydrophobic grains triggers capillary bulldozing, but water soon imbibes into the front, preventing formation of fingers. $C_b = 0.3$, $Q = 1$ mL/min, $D_{\text{visc}} = 0.003$. (b) Capillary and viscous bulldozing creates finger structures, but the walls of the fingers are gradually imbibed with the invading fluid. $C_b = 0.3$, $Q = 100$ mL/min, $D_{\text{visc}} = 0.3$ and $\varphi = 0.64$. The diameter of the circle is 26.8 cm.

Consider first the bottom row ($D_{\text{visc}} = 0.003$) in the phase diagram (Fig. 7.3) where we can neglect any influence of viscous forces. Along this row, the grain wetting goes from imbibition ($C_b = 0$) to drainage (capillary bulldozing, $C_b = 1$) through increasing fraction of hydrophobic grains. An interesting new dynamic is observed at intermediate mixed-wet ratios, e.g. $C_b = 0.3$ (Fig. 7.6). The inclusion of hydrophobic grains prevents spontaneous imbibition, yet the capillary bulldozing is not strong enough to create fingers. Instead, a large

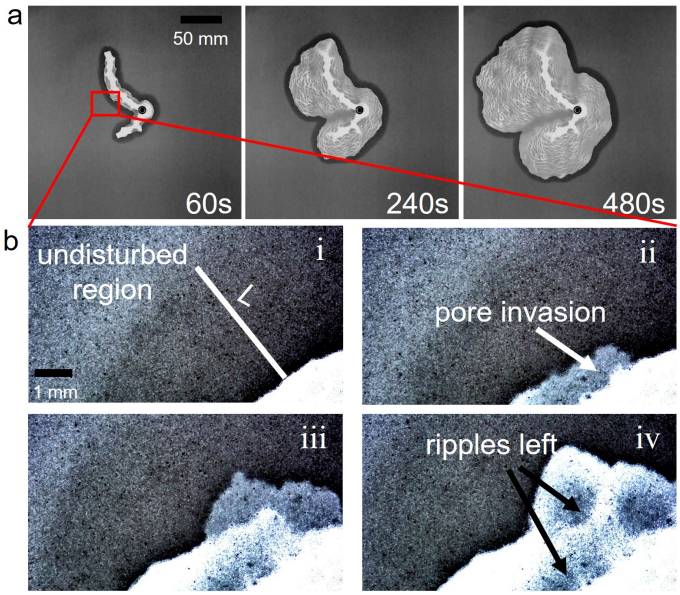

Fig. 7.7 (a) Time evolution of pore invasion followed by capillary bulldozing at $C_b = 0.5$ and $Q = 1$ mL/min, $D_{\text{visc}} = 0.003$ and $\varphi = 0.64$. (b) The close-up pictures to show the formation of beads ripples.

area around the inlet becomes invaded. The invasion is led by capillary bulldozing as can be clearly seen by the accumulated compaction front which appears like a dark band around the perimeter of the invaded area in the figure. Behind the front, granular material left behind is saturated by the invading fluid such that it appears a lighter shade of grey. Close inspection (Fig. 7.7 a) reveals that the saturated material behind the front has become patterned into a patchwork of fine ripples or "dunes" only a few millimeters in width and length. Fig. 7.7 (b) i - iv shows a close up time-sequence of the water penetration into the bulldozed compaction front. Even a small fraction of hydrophobic grains is able to arrest the meniscus creating a bulldozing action. As the accumulated front grows thicker, the friction increases, and at some point the water invades the packing in the front, leaving immersed granular material behind. The cycle of bulldozing and pore invasion occurs with high spatial frequency, creating the small-scale dune patterning.

At higher injection rates ($D_{\text{visc}} \geq 0.3$), the front speed is faster and fingering patterns are formed, even for $C_b = 0$ (see Regime V discussion below). The viscous flow along the increases the fluid pressure close to the inlet such that the pore invasion threshold is overcome. Fig. 7.6 b) ($D_{\text{visc}} = 0.3$, $C_b = 0.3$) shows a frictional fingering pattern where bulldozed material has been invaded by fluid (lighter grey areas). The front sections at the outer fingertips are still dry (dark) while pore invasion has taken place to an increasing degree closer to the inlet. Two factors contribute: the fluid pressure is higher closer to the inlet,

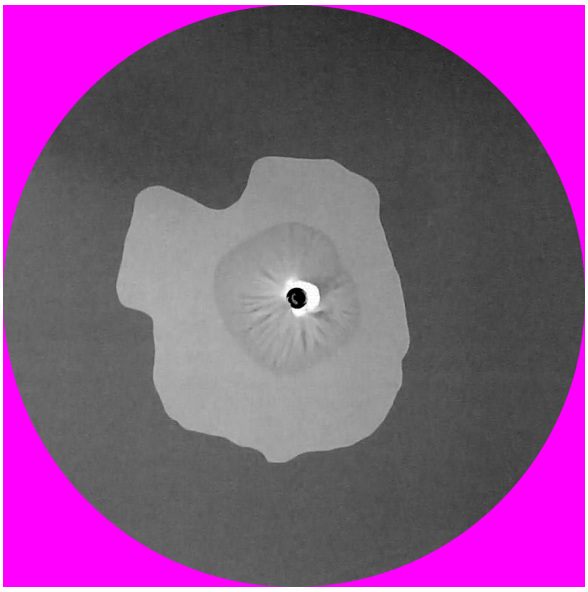

Fig. 7.8 Regime IV: Pore invasion followed by erosion of the granular bed close to the inlet. $C_b = 0$, $Q = 10$ mL/min, $D_{\text{visc}} = 0.03$ and $\varphi = 0.64$. The diameter of the circle is 26.8 cm.

pushing fluid into the packing. Secondly, the pore-invasion flow has had longer time to develop simply since the areas near the inlet are affected from the start of the experiment, while the fingertips at the perimeter has freshly bulldozed material.

Regime IV: Pore invasion followed by erosion

In Figure 7.8 and the image with magenta background in Figure 7.3, at $C_b = 0$, $Q = 10$ mL/min, and $D_{\text{visc}} = 0.03$, a pore invasion followed by bed erosion takes place. In this regime, the invading liquid imbibes imbibes the hydrophilic granular material in the same way as in Regime I. But because the injection rate is higher, the flow over the top of the sedimented granular bed is able to entrain grains and carry them along with the flow. The process is similar to sediment bedload transport [152] and in principle the criteria for onset of sediment motion is given by the Shield's number $\tau_* = \tau/((\rho_s - \rho)gD)$ where τ is a dimensional shear stress, ρ_s is the density of the sediment, ρ is the density of the fluid, g is the acceleration due to gravity, D is a characteristic particle diameter of the sediment, i.e. when fluid shear stress overcomes the gravitational stress. The flow transports grain from the centre and radially outwards, and erodes the bed into a channel pattern as can be seen in the close-up in Fig. 7.7 b). In the radial cell, the flow spreads out and the fluid velocity decreases with radius. Erosion stops once the velocity has decreased below the threshold given by the Shield's number. Pure imbibition (as in Regime I) is therefore the only active process beyond the "Shield's radius".

Regime V: capillary bulldozing followed by pore invasion and erosion

In Figure 7.9 and the images with white background and black frame at larger D_{visc}, we identified a fifth regime: capillary bulldozing followed by pore invasion followed by erosion.

When we increase D_{visc} by increasing the injection rate Q and viscosity of the invading fluid η_{inv}, the viscosity of the invading fluid becomes a main factor contributing to the pattern formation. One effect is the viscous erosion of the immersed granular material. Similar to Regime III, the capillary bulldozing is followed by the pore invasion in this regime, but the saturated region is gradually eroded by the viscous force of the invading fluid (as shown in Figure 7.10).

At high D_{visc}, the patterns are always fingers with a radial flow created by the viscous stabilisation. Fluid flows along the fingers, and protruding parts of the finger wall becomes eroded as grains are entrained with the fluid and carried along with the flow (Fig. 7.10). Erosion can only happen for grains that have been overrun by the meniscus and find themselves inside the invading fluid phase and not protected by the meniscus between the two fluids. Note that the erosion in Regime V acts on the compacted walls of the fingers, while the erosion referred to in Regime IV acted on the flat, sedimented bed.

It is interesting to note that the high D_{visc} results all feature finger patterns where the grains are bulldozed away by the invading fluid. For $C_b = 0$, the granular material is hydrophilic and should be wetted by the invading fluid causing spontaneous imbibition (which is what we observe at low injection rate). So why do we get bulldozing? Two possible contributing factors are 1) dynamic wetting effects and 2) viscous bulldozing.

It is well known that wetting phenomena are rate-dependent, and a "dynamic contact angle" is often used to describe the change in advancing contact angle as a function of meniscus velocity or imbibition rate [153–156]. Therefore, even though the grains are notionally wetted by the invading fluid, the high velocity of the incoming fluid may reduce the capillary suction or even reverse the wetting momentarily such that the grains are pushed away by the meniscus.

Secondly, the viscous deformability, D_{visc}, is high such that viscous forces dominate over the frictional strength of the layer. We saw in Chapters 3 and 4 how the viscous forces change the shape of the overall fingering pattern, the fingers having initially been created by capillary bulldozing. Here, we see another way in which viscous forces contribute to pattern formation. Even without any capillary effects, the viscous pressure acting on the frontline grains can be high enough to push the grains and bulldoze up a compaction front. We therefore define a new term, ‘viscous bulldozing’, to describe the formation of compaction fronts caused by a sharp ‘shock’ of a high viscosity invading fluid. The high viscosity fluid pushes the grains

ahead, while on the other side of the front, the low viscosity fluid flows without moving the grains and the grains therefore compact onto the invading mass.

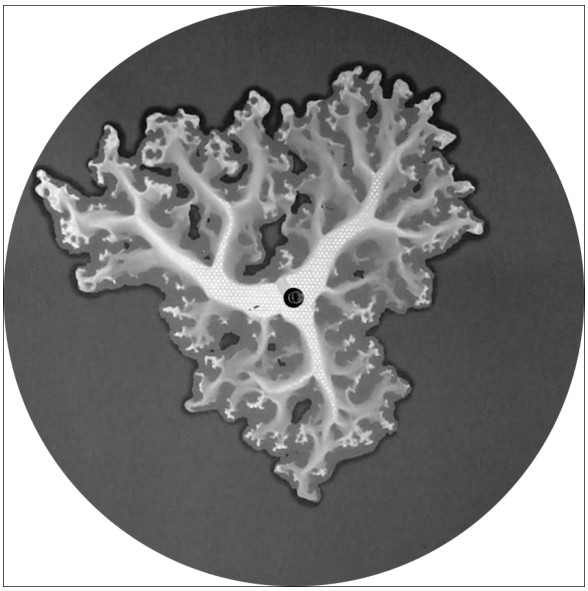

Fig. 7.9 Regime V: Bulldozing followed by pore invasion and erosion with the eroded mass flushed down along the fingers. $C_b = 0.1$, $Q = 100$ mL/min, $D_{\text{visc}} = 0.3$ and $\varphi = 0.64$. The diameter of the circle is 26.8 cm.

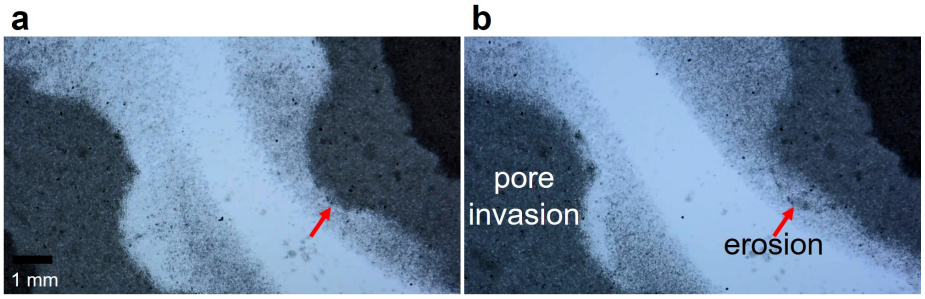

Fig. 7.10 Invading fluid erodes the saturated beads alongside the finger body. (a) The status before erosion, and (b) the status after erosion, the area pointed by the red arrow is clearly eroded.

7.2.2 Measurements of pattern features

To measure the degree of pore invasion in the granular material we define $S_a = (A_{\text{sat}} - A_{\text{finger}})/A_{\text{sat}}$ where A_{finger} is the clear area where the mass has been bulldozed away and A_{sat} is the total saturated area including the fingers. Fig. 7.11 shows as can be expected

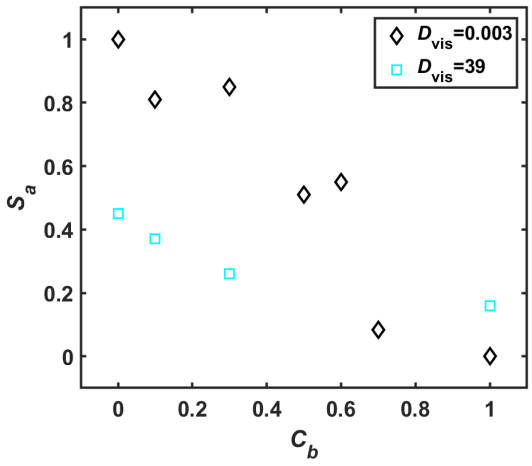

Fig. 7.11 Saturation number S_a as a function of C_b at two extremes $D_{\text{visc}} = 0.003$ and 39.

that the measured S_a is approximately 1 for Regime I (pure pore invasion, $C_b = 0$, $D_{\text{visc}} = 0.003$), decreasing with C_b to approximately 0 for C_b=1. The effect of D_{visc} on the degree of pore invasion is more complicated. Towards the hydrophobic end (low C_b), S_a shows full saturation for low D_{visc}, but decreases with increasing D_{visc} because of the formation of clear finger structures because of viscous bulldozing. Towards the hydrophilic end (high C_b), S_a is near 0 for low D_{visc} as the pattern consists of finger structure with dry side walls. At higher D_{visc}, however, we can see a small increase in S_a, which is indicative of some pore invasion, forced by viscous pressure near the inlet.

7.2.3 Effect of filling level

Pattern formation is also significantly affected by filling level φ. Figure 7.12 compares the patterns formed at $C_b = 0$ (hydrophobic grains, imbibition) and $C_b = 1$ (hydrophilic grains, drainage), in the high D_{visc} viscously stabilized regime (Q = 100mL/min, η_{inv} 141 mPa·s, $D_{\text{visc}} = 39$). Results for three filling levels are shown: $\varphi = 0.5$, 0.64 and 0.85.

Focusing first on the hydrophobic system ($C_b = 1$), at $\varphi = 0.5$ we have the same radial spoke pattern as discussed in Chapter 4. Increasing φ means that the compacted granular material takes up more space, and there are fewer fingers, separated by thicker compaction fronts. The importance of frictional stress increases with increasing φ. As friction increases, so does the heterogeneity and noise in the packing [129], and the fingers become less smooth, more jagged in appearance. At $\varphi = 0.85$, the expansion of a finger causes a large surrounding area to get compacted, and there are now much fewer fingers growing. The system is still

viscously stabilized, but the effect of frictional noise acting to break up the stabilization is much more noticeable.

The hydrophilic system ($C_b = 0$) shows a very similar trend, the only significant difference is the fact that the wetting condition favors pore invasion. At this high D_{visc}, the viscous bulldozing combined with the dynamic contact angle effect shapes the fluid penetration into fingers, but imbibition of fluid into the finger walls are seen just behind the finger tips. It is interesting to note that the hydrophibic system ($C_b = 1$) also displays some pore invasion, especially for high φ and close to the inlet. The higher frictional resistance causes an increased fluid pressure, and viscous stabilization causes this pressure to be the highest near the inlet.

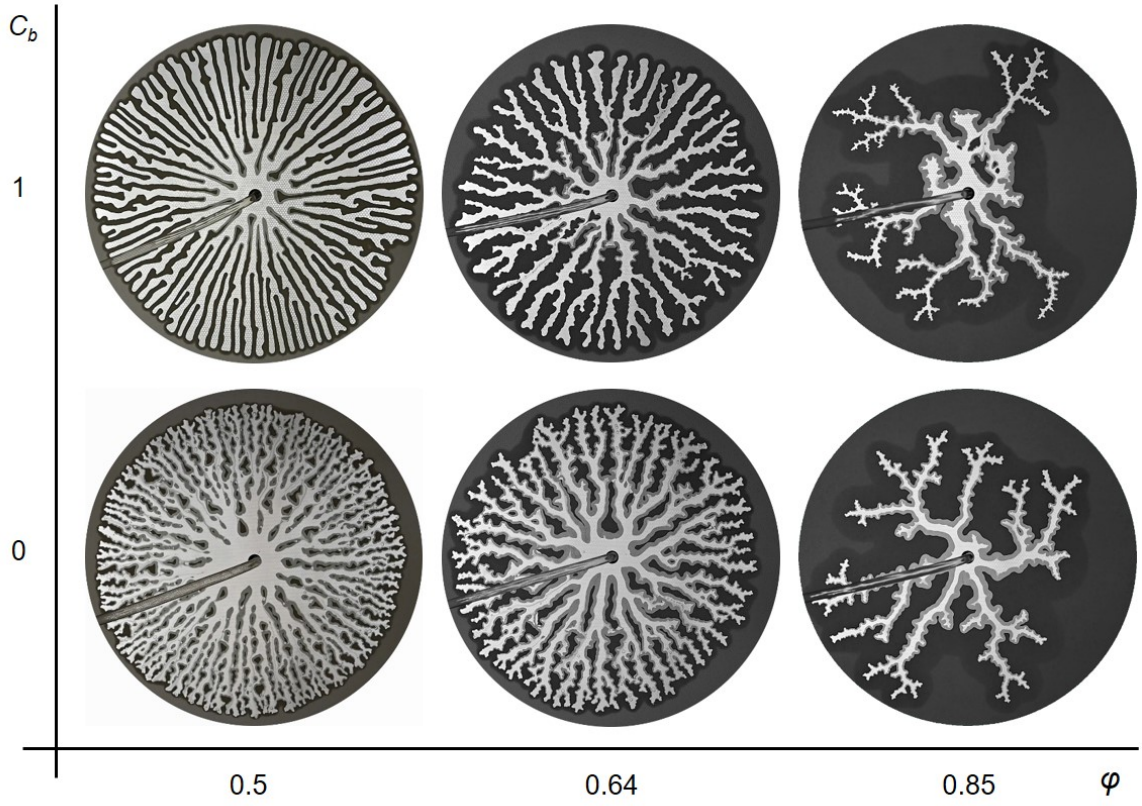

Fig. 7.12 Invasion patterns at $C_b = 0$ and 1, $\varphi = 0.5$, 0.64, 0.85, $Q = 100$ mL/min, $\eta_{\text{inv}} = 141$ mPa·s.

The results presented in Fig. 7.13 focuses on the special case of dune formation at low D_{visc} and intermediate C_b. The capillary bulldozing effect is here in competition with the tendency for imbibition. Reducing the filling level to $\varphi = 0.5$ produces a more clear finger structure with subsequent water penetration into the side walls. Reducing φ has the effect of lowering G such that bulldozing is comparatively easier. Increasing φ means more mass

has to be moved which requires higher fluid pressure, which in turn increases the rate of pore invasion. At $\varphi = 0.64$ the bulldozed front is being penetrated without fingers forming, with the invasion process happening in little stick-slip motions producing the dune pattern discussed in Section 7.2.1 Regime III.

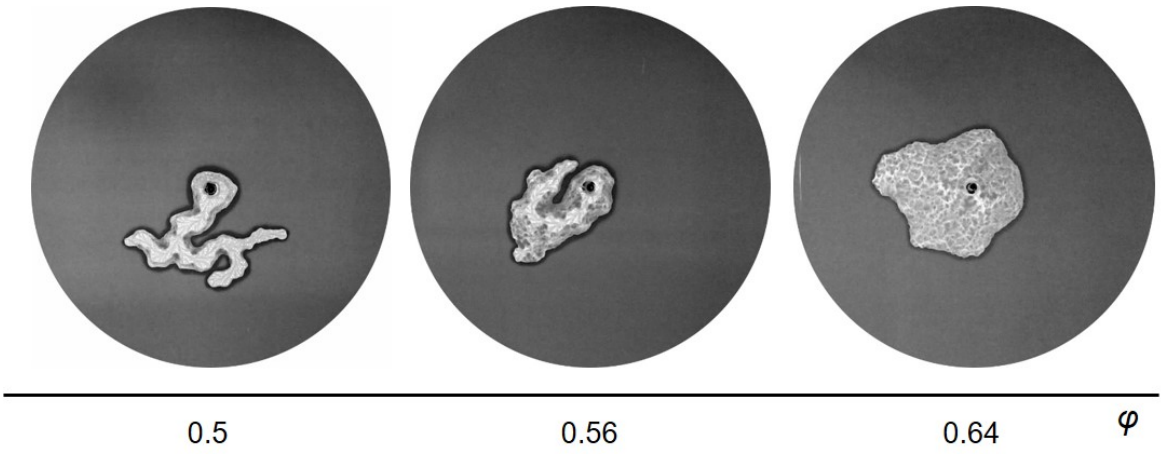

Fig. 7.13 Invasion patterns at $C_b = 0.1$, $\varphi = 0.5, 0.56, 0.64$, $Q = 1$ mL/min, $\eta_{\text{inv}} = 1$ mPa·s.

7.3 Conclusion

We have studied viscously stable frictional fingering patterns forming in imbibition, drainage and mixed-wet conditions. Water/glycerol mixtures were injected into the packing at different rates to produce varying levels of viscous deformability D_{visc}, and the granular material ranged from pure hydrophilic ($C_b = 0$) to pure hydrophobic ($C_b = 1$) with mixed-wet ratios in-between. Across the $D_{\text{visc}} - C_b$ parameter space studied here three basic invasion processes were found to occur either individually, simultaneously or sequentially: pore invasion, bulldozing and erosion. Five distinct regimes of invasion patterns were identified: (I) pure pore invasion, (II) pure capillary bulldozing, (III) capillary bulldozing followed by pore invasion, (IV) pore invasion followed by erosion and (V) bulldozing followed by pore invasion and erosion. These are caused by the relative significance of capillary pressure, friction stress and viscous pressure.

Increasing D_{visc} produced viscously stabilized fingers, eventually developing the radial spoke patterns discussed in Chapters 3 and 4. Even the naturally imbibing material ($C_b = 0$) produced finger structures at high D_{visc}. This is counterintuitive since the wetting condition favors pore invasion, with capillary action pulling fluid into the pore space. We propose a new mechanism: 'viscous bulldozing' to explain the observed phenomena: A viscous shock

front of high viscosity fluid will push grains ahead of it. Ahead of the front, the grains are "submerged" in a low viscosity fluid (air) which will easily flow above/through the packing without moving the grains. The grains therefore get bulldozed up into a compaction front by the oncoming fluid, and the friction of the bulldozed front acts to create fingers.

A naturally imbibing media ($C_b = 0$) will promote pore invasion into the finger walls. In our experiments some degree of pore invasion can also be seen for the hydrophobic grains ($C_b = 1$), caused by the elevated viscous pressures near the inlet.

The final process, erosion, is able to take place following on from pore invasion when the granular bed has been saturated with the invading fluid. Grains at the finger walls that are now submerged in the invading fluid become entrained in the fast-flowing fluid and flushed down along the fingers. This erosion process smoothes out the finger structure and carries material from the central parts towards the periphery of the pattern.

Chapter 8

Conclusions and outlook

8.1 Conclusions

The thesis studies the physics when a high-viscous fluid invades a deformable granular packing surrounded by a low-viscous fluid (viscously stable invasion, -$\mathcal{M}$) and the physics when a low-viscous fluid invades the deformable granular packing saturated by a high-viscous fluid (viscously unstable invasion, +$\mathcal{M}$) in different wetting conditions from a wide range of perspectives.

In Chapter 3, an experimental system in which water invades a hydrophobic granular layer surrounded by air (-$\mathcal{M}$) and forms the frictional fingers, is developed. On the basis of the experiment results, numerical simulations and theoretical models are developed to explain the underlying physics. Wider fingers are observed at lower granular filling fractions, in common with earlier experiments where fingers of air invaded a wet hydrophilic packing. A transition from single finger growth to multiple finger growth as we increase the injection rate, is observed, which has been demonstrated to be a consequence of viscous pressure gradients along the growing fingers. This study helps to fill an important gap in our knowledge of invasion patterns: understanding systems which produce complex patterns despite having an invading fluid of higher viscosity than the defending fluid.

Chapter 4 firstly expands the study in Chapter 3 by injecting high viscosity glycerol/water mixtures allowing to push the system to extreme levels of viscous stabilisation. A transition from the single-fingering to the radial spoke pattern is observed, and three domains are classified: 1) A frictional regime c ompletely dominated by the capillary-frictional instability producing a single finger.

2) A transitional regime where viscous pressure can sustain the simultaneous growth of multiple fingers.

3) A viscous-frictional regime, where the capillary-frictional instability breaks the front up into fingers but the shape of the overall pattern is governed by viscous stabilisation producing a level front.

A noticeable phenomenon in the experimental result is that the patterns formed are almost the identical even they are performed at different injection rates Q and viscosities η. The reason behind is because the response to increased viscosity in the invading phase is similar to the effect of increased injection rate which is unsurprising since both lead to increased capillary number Ca. This phenomenon is verified by the simulation. In the simulation, I am able to increase the injection rates well beyond what is achievable in the experiment. Generally, a close agreement between experiment and simulation was found.

Further more, the opposite case of viscously *unstable* ($+\mathcal{M}$) was explored in the same radial cell configuration. In the experiments, the viscously unstable growth at low Ca produced the frictional fingering accompanied with a fixed compaction front, while at high Ca experiments produced non-compact growth. The main mechanism controlling the pattern formation in the $+\mathcal{M}$ scenario at high Ca is the lubrication of the granular material by the high viscosity defending fluid in which it is submerged. The granular packing starts to become partly fluidized when increasing Ca, forming the wider fingers and thereby a thicker granular front. Here, the viscous instability mechanism acts both on the system scale, and also locally: the fluidized accumulation front itself is unstable to perturbations, and tiny air fingers grow into the front along the moving sections, creating the "coral" pattern. Increase Ca further produces fluid flow that is fast enough to mobilise the entire granular layer, and the system reverts to what is essentially viscous fingering in a granular suspension.

Chapter 5 focuses on the alignment of the frictional fingering under different stabilizing conditions in a linear Hele-Shaw cell with three fixed boundaries. The viscously stable invasion of water/glycerol into a hydrophobic granular packing as described in Chapter 4 is repeated but this time in a linear cell. The results are mostly similar to the results in Chapter 4, but the invasion front marches in one direction because of the confinement and the "stable" invasion creates a straight front from one side of the channel to the other. The effect of the plate spacing b on the finger width is tested in experiments where the finger width is found to increases as a function of b. The simulation was calibrated to reproduce the plate spacing dependency. The effect of plate spacing gradient db/dy on finger alignment was studied. At $db/dy < 0$, the fluid invades from a wider spacing to a narrower spacing, and the finger tends to grow sideways and occupy the wider-spaced region. Propagation towards narrower gaps therefore results in stabilized fronts. At $db/dy > 0$, the fluid invades in a manner opposite to that in $db/dy < 0$. The finger preferentially grows in a direction towards the larger gap, and the invasion is therefore unstable. The effect of the tilt angle α has also

been numerically studied. The patterns formed at $\alpha > 0$ is very similar to when $db/dy < 0$ because in both cases the fronts are under the influence of a stabilizing force. The patterns formed at $\alpha < 0$ are similar to when $db/dy > 0$ in that they both represent unstable scenarios with non-compact growth of a single finger. While both systems feature a Chapter 5 focuses on the alignment of the frictional fingering under different stabilizing conditions in a linear Hele-Shaw cell with three fixed boundaries.

Chapter 6 studies the (viscously unstable) capillary fracturing ($+\mathcal{M}$) under different conditions. The pattern formation is sensitive to the volume fraction ϕ of the granular material filling the gap in the cell. At relatively low $\phi = 0.53$, the fractures are wide and appear fully-opened. Increasing the volume fraction to $\phi = 0.55$ results in narrower, partially open fractures similar to the capillary fracturing studied in the previous literature [36, 28]. At still higher $\phi = 0.58$, capillary invasion was observed following on from the fracturing. The patterns formed at different pressures are different and can be divided into three phases: capillary fracturing, fracture widening, and pneumatic caving. In the experiment with larger plate spacing b, we observe a transition from partially-opened fracturing to fully-opened fracturing at lower pressure, and a reduction of the widening/caving at higher pressure. The boundary also plays a significant role in pattern formation, more fully-opened fracturing is observed because the granular packing becomes easier to fluidized and push out of a cell that has open boundaries.

Chapter 7 studies the patterns formed in imbibing, repelling and mixed-wet granular materials. Hydrophobic and hydrophilic beads are tested separately, and mixed in different ratios to produce granular packings with different wetting conditions ranging from imbibition to drainage. Water and water/glycerol mixtures are injected at different rates into a radial cell partially filled with the granular material. Three invasion events occurred individually, simultaneously or sequentially: pore invasion, capillary bulldozing and erosion, and five regimes of invasion patterns are identified: (I) pure pore invasion, (II) pure capillary bulldozing, (III) capillary bulldozing followed by pore invasion, (IV) pore invasion followed by erosion and (V) capillary bulldozing followed by pore invasion and erosion. A new pattern formation process is discovered at intermediate wetting conditions at low injection rate: Here, the inclusion of hydrophobic beads triggers capillary bulldozing such that the invading water is surrounded by a compaction front. This front is subjected to periodic invasion events that leave behind a pattern of 'dunes'. At high injection rate in imbibing media we discover another new pattern formation mechanism: 'viscous bulldozing' where the viscous shock front accumulates grain in a compaction front that produces frictional fingers in the same way as for capillary bulldozing in repelling media.

8.2 Recommendations for future work

The projects presented in the current thesis greatly extends the studied parameter space of frictional flow patterns shaped by viscous and capillary forces. Some aspects, like the viscous stabilization mechanism, has been explored in considerable detail, while other chapters in the thesis are more exploratory, with further work necessary to develop a full theoretical description of the phenomena. Viscously stable and unstable invasion in drainage has been studied here, as well as viscously stable imbibition. That leaves the combination of unstable low-viscosity invading fluid invading an imbibing granular material to be discovered in future studies. In addition, the effect of the wettability on invasion patterns needs to be studied further. The study in Chapter 7 mixes hydrophobic and hydrophilic beads to change the overall wettability of the granular packing, however other alternatives such as changing the contact angle uniformly should be studied. Even for a mixed-wet system there are many parameters, including spatial heterogeneity and degree of hydrophobicity, that could potentially affect the pattern formation processes. I have performed a preliminary comparison of different stabilizing mechanisms including viscous stabilization, confinement gradient, and gravity stabilization. Future work should investigate these in more detail. Also unknown at this time is how different stabilising or destabilising mechanisms will interact together if more than one is present within the system.

References

[1] James A Tindall, James R Kunkel, Dean E Anderson, et al. *Unsaturated zone hydrology for scientists and engineers*, volume 3. Prentice Hall Upper Saddle River, NJ, 1999.

[2] Salah Jellali, Paul Muntzer, Olivier Razakarisoa, and Gerhard Schäfer. Large scale experiment on transport of trichloroethylene in a controlled aquifer. *Transport in Porous Media*, 44(1):145–163, 2001.

[3] Samuel Krevor, Martin J Blunt, Sally M Benson, Christopher H Pentland, Catriona Reynolds, Ali Al-Menhali, and Ben Niu. Capillary trapping for geologic carbon dioxide storage–from pore scale physics to field scale implications. *International Journal of Greenhouse Gas Control*, 40:221–237, 2015.

[4] Stefan Bachu. Co2 storage in geological media: Role, means, status and barriers to deployment. *Progress in energy and combustion science*, 34(2):254–273, 2008.

[5] Ali S Al-Menhali, Hannah P Menke, Martin J Blunt, and Samuel C Krevor. Pore scale observations of trapped co2 in mixed-wet carbonate rock: applications to storage in oil fields. *Environmental science & technology*, 50(18):10282–10290, 2016.

[6] Norman R Morrow. Wettability and its effect on oil recovery. *Journal of petroleum technology*, 42(12):1476–1484, 1990.

[7] AR Kovscek, H Wong, and CJ Radke. A pore-level scenario for the development of mixed wettability in oil reservoirs. *AIChE Journal*, 39(6):1072–1085, 1993.

[8] Bernard P Boudreau, Chris Algar, Bruce D Johnson, Ian Croudace, Allen Reed, Yoko Furukawa, Kelley M Dorgan, Peter A Jumars, Abraham S Grader, and Bruce S Gardiner. Bubble growth and rise in soft sediments. *Geology*, 33(6):517–520, 2005.

[9] Benjamin P Scandella, Liam Pillsbury, Thomas Weber, Carolyn Ruppel, Harold F Hemond, and Ruben Juanes. Ephemerality of discrete methane vents in lake sediments. *Geophysical Research Letters*, 43(9):4374–4381, 2016.

[10] Sungyon Lee, Jeremy Lee, Robin Le Mestre, Feng Xu, and Christopher W MacMinn. Migration, trapping, and venting of gas in a soft granular material. *Physical Review Fluids*, 5(8):084307, 2020.

[11] Benjamin P Scandella, Charuleka Varadharajan, Harold F Hemond, Carolyn Ruppel, and Ruben Juanes. A conduit dilation model of methane venting from lake sediments. *Geophysical Research Letters*, 38(6), 2011.

[12] Janet Hooke. River meander behaviour and instability: a framework for analysis. *Transactions of the Institute of British Geographers*, 28(2):238–253, 2003.

[13] Stefano Lanzoni and Giovanni Seminara. On the nature of meander instability. *Journal of Geophysical Research: Earth Surface*, 111(F4), 2006.

[14] RA Callander. River meandering. *Annual Review of Fluid Mechanics*, 10(1):129–158, 1978.

[15] G Hulme. The interpretation of lava flow morphology. *Geophysical Journal International*, 39(2):361–383, 1974.

[16] Anthony Philpotts and Jay Ague. *Principles of igneous and metamorphic petrology*. Cambridge University Press, 2009.

[17] Haim Tsoar. Bagnold, ra 1941: The physics of blown sand and desert dunes. london: Methuen. *Progress in physical geography*, 18(1):91–96, 1994.

[18] Jim Best. The fluid dynamics of river dunes: A review and some future research directions. *Journal of Geophysical Research: Earth Surface*, 110(F4), 2005.

[19] Mary C Bourke, Nick Lancaster, Lori K Fenton, Eric JR Parteli, James R Zimbelman, and Jani Radebaugh. Extraterrestrial dunes: An introduction to the special issue on planetary dune systems. *Geomorphology*, 121(1-2):1–14, 2010.

[20] JAMES P. BLAIR. Oxbow lake. [EB/OL]. https://www.nationalgeographic.org/encyclopedia/oxbow-lake/#oxbow-lake. Accessed: 2020-11-15.

[21] CHRIS JOHNS. Mount nyiragongo. [EB/OL]. https://www.nationalgeographic.org/photo/magmacosta-volcanic-990-60862/#mount-nyiragongo. Accessed: 2020-11-15.

[22] Thomas Eliasson. Igneous intrusions. [EB/OL]. https://australian.museum/learn/minerals/shaping-earth/igneous-intrusions/. Accessed: 2020-11-15.

[23] CC0 Public Domain. Beach sand ripples. [EB/OL]. https://phys.org/news/2018-09-beach-sand-ripples-fingerprints-ancient.html. Accessed: 2020-11-15.

[24] B Sandnes, H A Knudsen, K J Måløy, and E G Flekkøy. Labyrinth patterns in confined granular-fluid systems. *Phys. Rev. Lett.*, 99(3):038001, 2007.

[25] Philip Geoffrey Saffman and Geoffrey Ingram Taylor. The penetration of a fluid into a porous medium or hele-shaw cell containing a more viscous liquid. *Proc. R. Soc. Lond. A*, 245(1242):312–329, 1958.

[26] Jon Alm Eriksen, Renau d Toussaint, Knut Jørgen Måløy, Eirik Flekkøy, Olivier Galland, and Bjørnar Sandnes. Pattern formation of frictional fingers in a gravitational potential. *Phys. Rev. Fluids*, 3(1):013801, 2018.

[27] B Sandnes, E G Flekkøy, H A Knudsen, K J Måløy, and H See. Patterns and flow in frictional fluid dynamics. *Nature Comms.*, 2(1):1–8, 2011.

[28] James M Campbell, Deren Ozturk, and Bjørnar Sandnes. Gas-driven fracturing of saturated granular media. *Phys. Rev. Appl.*, 8(6):064029, 2017.

[29] Haiying Huang, Fengshou Zhang, Patrick Callahan, and Joseph Ayoub. Granular fingering in fluid injection into dense granular media in a hele-shaw cell. *Physical review letters*, 108(25):258001, 2012.

[30] Bertrand Levaché and Denis Bartolo. Revisiting the saffman-taylor experiment: imbibition patterns and liquid-entrainment transitions. *Physical review letters*, 113(4):044501, 2014.

[31] C Chevalier, A Lindner, M Leroux, and E Clément. Morphodynamics during air injection into a confined granular suspension. *J. Non-Netwon. Fluid Mech.*, 158(1-3):63–72, 2009.

[32] Amina Islam, Sylvie Chevalier, Imen Ben Salem, Yves Bernabe, Ruben Juanes, and Mohamed Sassi. Characterization of the crossover from capillary invasion to viscous fingering to fracturing during drainage in a vertical 2d porous medium. *International journal of multiphase flow*, 58:279–291, 2014.

[33] Jeong-Hoon Choi, Yongkoo Seol, Ray Boswell, and Ruben Juanes. X-ray computed-tomography imaging of gas migration in water-saturated sediments: From capillary invasion to conduit opening. *Geophysical Research Letters*, 38(17), 2011.

[34] Fredrik K Eriksen, Renaud Toussaint, Antoine L Turquet, Knut J Måløy, and Eirik G Flekkøy. Pneumatic fractures in confined granular media. *Physical Review E*, 95(6):062901, 2017.

[35] Fredrik K Eriksen, Renaud Toussaint, Knut J Måløy, and Eirik G Flekkøy. Invasion patterns during two-phase flow in deformable porous media. *Frontiers in Physics*, 3:81, 2015.

[36] Ran Holtzman, Michael L Szulczewski, and Ruben Juanes. Capillary fracturing in granular media. *Physical review letters*, 108(26):264504, 2012.

[37] Kun Xue, Panpan Han, Kaiyuan Du, Yixiang Gan, Ziwei Wang, and Chunhua Bai. Morphodynamics of a dense particulate medium under radial explosion. *Soft matter*, 16(6):1498–1517, 2020.

[38] Xiang Cheng, Lei Xu, Aaron Patterson, Heinrich M Jaeger, and Sidney R Nagel. Towards the zero-surface-tension limit in granular fingering instability. *Nature Physics*, 4(3):234–237, 2008.

[39] Deren Ozturk, Miles L Morgan, and Bjørnar Sandnes. Flow-to-fracture transition and pattern formation in a discontinuous shear thickening fluid. *Communications Physics*, 3(1):1–9, 2020.

[40] Petri Fast, L Kondic, Michael J Shelley, and Peter Palffy-Muhoray. Pattern formation in non-newtonian hele–shaw flow. *Physics of Fluids*, 13(5):1191–1212, 2001.

[41] Marie-Julie Dalbe and Ruben Juanes. Morphodynamics of fluid-fluid displacement in three-dimensional deformable granular media. *Physical Review Applied*, 9(2):024028, 2018.

[42] Germán Varas, Valérie Vidal, and Jean-Christophe Géminard. Venting dynamics of an immersed granular layer. *Physical Review E*, 83(1):011302, 2011.

[43] Joachim Falck Brodin. A new vision for 3d experiments on flow in porous media. Master's thesis, 2019.

[44] Hanita Ovdat and Brian Berkowitz. Pore-scale study of drainage displacement under combined capillary and gravity effects in index-matched porous media. *Water resources research*, 42(6), 2006.

[45] Xiang-Zhao Kong, Markus Holzner, Fritz Stauffer, and Wolfgang Kinzelbach. Time-resolved 3d visualization of air injection in a liquid-saturated refractive-index-matched porous medium. *Experiments in fluids*, 50(6):1659–1670, 2011.

[46] Prerna Sharma, P Aswathi, Anit Sane, Shankar Ghosh, and S Bhattacharya. Three-dimensional real-time imaging of bi-phasic flow through porous media. *Review of Scientific Instruments*, 82(11):113704, 2011.

[47] Kamaljit Singh, Hagen Scholl, Martin Brinkmann, Marco Di Michiel, Mario Scheel, Stephan Herminghaus, and Ralf Seemann. The role of local instabilities in fluid invasion into permeable media. *Scientific reports*, 7(1):1–11, 2017.

[48] Lin Feng, Shuhong Li, Yingshun Li, Huanjun Li, Lingjuan Zhang, Jin Zhai, Yanlin Song, Biqian Liu, Lei Jiang, and Daoben Zhu. Super-hydrophobic surfaces: from natural to artificial. *Advanced materials*, 14(24):1857–1860, 2002.

[49] Shabana Afzal, Walid A Daoud, and Steven J Langford. Superhydrophobic and photocatalytic self-cleaning cotton. *Journal of Materials Chemistry A*, 2(42):18005–18011, 2014.

[50] Glen McHale, MI Newton, and NJ Shirtcliffe. Water-repellent soil and its relationship to granularity, surface roughness and hydrophobicity: a materials science view. *European Journal of Soil Science*, 56(4):445–452, 2005.

[51] Knut Jørgen Måløy, Jens Feder, and Torstein Jøssang. Viscous fingering fractals in porous media. *Physical review letters*, 55(24):2688, 1985.

[52] Thomas A Witten Jr and Leonard M Sander. Diffusion-limited aggregation, a kinetic critical phenomenon. *Physical review letters*, 47(19):1400, 1981.

[53] Knut Jørgen Måløy, Liv Furuberg, Jens Feder, and Torstein Jøssang. Dynamics of slow drainage in porous media. *Physical review letters*, 68(14):2161, 1992.

[54] Franziska Moebius and Dani Or. Interfacial jumps and pressure bursts during fluid displacement in interacting irregular capillaries. *Journal of colloid and interface science*, 377(1):406–415, 2012.

[55] Ryan T Armstrong and Steffen Berg. Interfacial velocities and capillary pressure gradients during haines jumps. *Physical Review E*, 88(4):043010, 2013.

[56] Steffen Berg, Holger Ott, Stephan A Klapp, Alex Schwing, Rob Neiteler, Niels Brussee, Axel Makurat, Leon Leu, Frieder Enzmann, Jens-Oliver Schwarz, et al. Real-time 3d imaging of haines jumps in porous media flow. *Proceedings of the National Academy of Sciences*, 110(10):3755–3759, 2013.

[57] Roland Lenormand and Cesar Zarcone. Invasion percolation in an etched network: measurement of a fractal dimension. *Physical review letters*, 54(20):2226, 1985.

[58] Roland Lenormand. Liquids in porous media. *Journal of Physics: Condensed Matter*, 2(S):SA79, 1990.

[59] Benzhong Zhao, Christopher W MacMinn, and Ruben Juanes. Wettability control on multiphase flow in patterned microfluidics. *Proceedings of the National Academy of Sciences*, 113(37):10251–10256, 2016.

[60] M Dong and I Chatzis. The imbibition and flow of a wetting liquid along the corners of a square capillary tube. *Journal of colloid and interface science*, 172(2):278–288, 1995.

[61] Paul Concus and Robert Finn. On the behavior of a capillary surface in a wedge. *Proceedings of the National Academy of Sciences of the United States of America*, 63(2):292, 1969.

[62] TC Ransohoff and CJ Radke. Laminar flow of a wetting liquid along the corners of a predominantly gas-occupied noncircular pore. *Journal of colloid and interface science*, 121(2):392–401, 1988.

[63] LA Romero and FG Yost. Flow in an open channel capillary. *Journal of Fluid Mechanics*, 322:109–129, 1996.

[64] Mark M Weislogel and Seth Lichter. Capillary flow in an interior corner. *Journal of Fluid Mechanics*, 373:349–378, 1998.

[65] Jose Bico and David Quéré. Rise of liquids and bubbles in angular capillary tubes. *Journal of colloid and Interface Science*, 247(1):162–166, 2002.

[66] Benzhong Zhao, Christopher W MacMinn, Bauyrzhan K Primkulov, Yu Chen, Albert J Valocchi, Jianlin Zhao, Qinjun Kang, Kelsey Bruning, James E McClure, Cass T Miller, et al. Comprehensive comparison of pore-scale models for multiphase flow in porous media. *Proceedings of the National Academy of Sciences*, 116(28):13799–13806, 2019.

[67] Daniel A Cogswell and Michael L Szulczewski. Simulation of incompressible two-phase flow in porous media with large timesteps. *Journal of Computational Physics*, 345:856–865, 2017.

[68] Ran Holtzman and Enrico Segre. Wettability stabilizes fluid invasion into porous media via nonlocal, cooperative pore filling. *Physical review letters*, 115(16):164501, 2015.

[69] Ran Holtzman. Effects of pore-scale disorder on fluid displacement in partially-wettable porous media. *Scientific reports*, 6(1):1–10, 2016.

[70] Ryan T Armstrong, Chenhao Sun, Peyman Mostaghimi, Steffen Berg, Maja Rücker, Paul Luckham, Apostolos Georgiadis, and James E McClure. Multiscale characterization of wettability in porous media. *Transport in Porous Media*, 140(1):215–240, 2021.

[71] Peter Mora, Gabriele Morra, Dave A Yuen, and Ruben Juanes. Optimal wetting angles in lattice boltzmann simulations of viscous fingering. *Transport in Porous Media*, 136(3):831–842, 2021.

[72] Bauyrzhan K Primkulov, Amir A Pahlavan, Xiaojing Fu, Benzhong Zhao, Christopher W MacMinn, and Ruben Juanes. Wettability and lenormand's diagram. *Journal of Fluid Mechanics*, 923, 2021.

[73] Li Chen, An He, Jianlin Zhao, Qinjun Kang, Zeng-Yao Li, Jan Carmeliet, Naoki Shikazono, and Wen-Quan Tao. Pore-scale modeling of complex transport phenomena in porous media. *Progress in Energy and Combustion Science*, 88:100968, 2022.

[74] Julie Murison, Benoît Semin, Jean-Christophe Baret, Stephan Herminghaus, Matthias Schröter, and Martin Brinkmann. Wetting heterogeneities in porous media control flow dissipation. *Physical Review Applied*, 2(3):034002, 2014.

[75] Ahmed AlRatrout, Martin J Blunt, and Branko Bijeljic. Wettability in complex porous materials, the mixed-wet state, and its relationship to surface roughness. *Proceedings of the National Academy of Sciences*, 115(36):8901–8906, 2018.

[76] Amir Jahanbakhsh, Omid Shahrokhi, and M Mercedes Maroto-Valer. Understanding the role of wettability distribution on pore-filling and displacement patterns in a homogeneous structure via quasi 3d pore-scale modelling. *Scientific reports*, 11(1):1–12, 2021.

[77] Kamaljit Singh, Branko Bijeljic, and Martin J Blunt. Imaging of oil layers, curvature and contact angle in a mixed-wet and a water-wet carbonate rock. *Water Resources Research*, 52(3):1716–1728, 2016.

[78] Stefan Iglauer, MA Fernø, Paul Shearing, and MJ Blunt. Comparison of residual oil cluster size distribution, morphology and saturation in oil-wet and water-wet sandstone. *Journal of colloid and interface science*, 375(1):187–192, 2012.

[79] Alessio Scanziani, Qingyang Lin, Abdulla Alhosani, Martin J Blunt, and Branko Bijeljic. Dynamics of fluid displacement in mixed-wet porous media. *Proceedings of the Royal Society A*, 476(2240):20200040, 2020.

[80] Yue Meng, Bauyrzhan K Primkulov, Zhibing Yang, Chung Yee Kwok, and Ruben Juanes. Jamming transition and emergence of fracturing in wet granular media. *Physical Review Research*, 2(2):022012, 2020.

[81] Tsimur Davydzenka, Samuel Fagbemi, and Pejman Tahmasebi. Wettability control on deformation: Coupled multiphase fluid and granular systems. *Physical Review E*, 102(1):013301, 2020.

[82] Tsimur Davydzenka, Samuel Fagbemi, and Pejman Tahmasebi. Coupled fine-scale modeling of the wettability effects: Deformation and fracturing. *Physics of Fluids*, 32(8):083308, 2020.

[83] Pascale Aussillous and David Quéré. Liquid marbles. *Nature*, 411(6840):924–927, 2001.

[84] Pascale Aussillous and David Quéré. Properties of liquid marbles. *Proceedings of the Royal Society A: Mathematical, Physical and Engineering Sciences*, 462(2067):973–999, 2006.

[85] Glen McHale and Michael I Newton. Liquid marbles: principles and applications. *Soft Matter*, 7(12):5473–5481, 2011.

[86] Stefan H Doerr, RA Shakesby, and RPDm Walsh. Soil water repellency: its causes, characteristics and hydro-geomorphological significance. *Earth-Science Reviews*, 51(1-4):33–65, 2000.

[87] John Letey. Causes and consequences of fire-induced soil water repellency. *Hydrological Processes*, 15(15):2867–2875, 2001.

[88] Julie L Roy and William B McGill. Assessing soil water repellency using the molarity of ethanol droplet (med) test. *Soil Science*, 167(2):83–97, 2002.

[89] PD Hallett and IM Young. Changes to water repellence of soil aggregates caused by substrate-induced microbial activity. *European Journal of Soil Science*, 50(1):35–40, 1999.

[90] Richard A Shakesby, CDA Coelho, Antonio D Ferreira, James P Terry, and Rory PD Walsh. Wildfire impacts on soil-erosion and hydrology in wet mediterranean forest, portugal. *International Journal of Wildland Fire*, 3(2):95–110, 1993.

[91] Yong-Hoon Byun, M Khoa Tran, Tae Sup Yun, and Jong-Sub Lee. Strength and stiffness characteristics of unsaturated hydrophobic granular media. *Geotechnical Testing Journal*, 35(1):193–200, 2012.

[92] Glen McHale, Neil J Shirtcliffe, Michael I Newton, F Brian Pyatt, and Stefan H Doerr. Self-organization of hydrophobic soil and granular surfaces. *Applied physics letters*, 90(5):054110, 2007.

[93] Carl Friedrich Gauß. Besprechung des buchs von la seeber: Untersuchungen uber die eigenschaften der positiven ternaren quadratischen formen usw. *Gottingensche Gelehrte Anzeigen*, 2:188–196, 1876.

[94] G David Scott. Packing of spheres: packing of equal spheres. *Nature*, 188(4754):908–909, 1960.

[95] Tomaso Aste, Mohammad Saadatfar, and TJ Senden. Geometrical structure of disordered sphere packings. *Physical Review E*, 71(6):061302, 2005.

[96] George Y Onoda and Eric G Liniger. Random loose packings of uniform spheres and the dilatancy onset. *Physical review letters*, 64(22):2727, 1990.

[97] Melissa Jerkins, Matthias Schröter, Harry L Swinney, Tim J Senden, Mohammad Saadatfar, and Tomaso Aste. Onset of mechanical stability in random packings of frictional spheres. *Physical review letters*, 101(1):018301, 2008.

[98] G David Scott and D Marc Kilgour. The density of random close packing of spheres. *Journal of Physics D: Applied Physics*, 2(6):863, 1969.

[99] Salvatore Torquato, Thomas M Truskett, and Pablo G Debenedetti. Is random close packing of spheres well defined? *Physical review letters*, 84(10):2064, 2000.

[100] Anthony D Rosato, Oleksandr Dybenko, David J Horntrop, Vishagan Ratnaswamy, and Lou Kondic. Microstructure evolution in density relaxation by tapping. *Physical Review E*, 81(6):061301, 2010.

[101] V Ratnaswamy, AD Rosato, D Blackmore, X Tricoche, N Ching, and L Zuo. Evolution of solids fraction surfaces in tapping: simulation and dynamical systems analysis. *Granular Matter*, 14(2):163–168, 2012.

[102] Aleksandar Donev, Ibrahim Cisse, David Sachs, Evan A Variano, Frank H Stillinger, Robert Connelly, Salvatore Torquato, and Paul M Chaikin. Improving the density of jammed disordered packings using ellipsoids. *Science*, 303(5660):990–993, 2004.

[103] Gye-Chun Cho, Jake Dodds, and J Carlos Santamarina. Closure to "particle shape effects on packing density, stiffness, and strength: Natural and crushed sands" by gye-chun cho, jake dodds, and j. carlos santamarina. *Journal of geotechnical and geoenvironmental engineering*, 133(11):1474–1474, 2007.

[104] Ahmet Burak Göktepe and Alper Sezer. Effect of particle shape on density and permeability of sands. *Proceedings of the Institution of Civil Engineers-Geotechnical Engineering*, 163(6):307–320, 2010.

[105] Iman Mehdipour and Kamal H Khayat. Effect of particle-size distribution and specific surface area of different binder systems on packing density and flow characteristics of cement paste. *Cement and Concrete Composites*, 78:120–131, 2017.

[106] Hong Yong Sohn and C Moreland. The effect of particle size distribution on packing density. *The Canadian Journal of Chemical Engineering*, 46(3):162–167, 1968.

[107] Kenneth W Desmond and Eric R Weeks. Influence of particle size distribution on random close packing of spheres. *Physical Review E*, 90(2):022204, 2014.

[108] Robert S Farr and Robert D Groot. Close packing density of polydisperse hard spheres. *The Journal of chemical physics*, 131(24):244104, 2009.

[109] AB Yu and N Standish. A study of the packing of particles with a mixture size distribution. *Powder Technology*, 76(2):113–124, 1993.

[110] Henry Selby Hele-Shaw. Flow of water. *Nature*, 58(1509):520–520, 1898.

[111] Louis Melville Milne-Thomson. *Theoretical hydrodynamics*. Courier Corporation, 1996.

[112] H Darcy. Les fontaines publiques de la ville de dijon, paris: Dalmont, 1856. *Google Scholar*.

[113] Morris Muskat and Ralph Dewey Wyckoff. The flow of homogeneous fluids through porous media. 1946.

[114] Josef Kozeny. Uber kapillare leitung der wasser in boden. *Royal Academy of Science, Vienna, Proc. Class I*, 136:271–306, 1927.

[115] Philip Crosbie Carman. Fluid flow through granular beds. *Trans. Inst. Chem. Eng.*, 15:150–166, 1937.

[116] Philip Crosbie Carman. Flow of gases through porous media. 1956.

[117] Lingran Zhang, Nho Gia Hien Nguyen, Stéphane Lambert, François Nicot, Florent Prunier, and Irini Djeran-Maigre. The role of force chains in granular materials: from statics to dynamics. *European Journal of Environmental and Civil Engineering*, 21(7-8):874–895, 2017.

[118] ME Cates, JP Wittmer, J-P Bouchaud, and Ph Claudin. Jamming, force chains, and fragile matter. *Physical review letters*, 81(9):1841, 1998.

[119] Takao Wakabayashi. Photo-elastic method for determination of stress in powdered mass. *Journal of the Physical Society of Japan*, 5(5):383–385, 1950.

[120] Trushant S Majmudar and Robert P Behringer. Contact force measurements and stress-induced anisotropy in granular materials. *Nature*, 435(7045):1079–1082, 2005.

[121] Dapeng Bi, Jie Zhang, Bulbul Chakraborty, and Robert P Behringer. Jamming by shear. *Nature*, 480(7377):355–358, 2011.

[122] Veronique Trappe, V Prasad, Luca Cipelletti, PN Segre, and David A Weitz. Jamming phase diagram for attractive particles. *Nature*, 411(6839):772–775, 2001.

[123] Andrea J Liu and Sidney R Nagel. Jamming is not just cool any more. *Nature*, 396(6706):21–22, 1998.

[124] Dan Howell, RP Behringer, and Christian Veje. Fluctuations and dynamics for a two-dimensional sheared granular material. In *APS Division of Fluid Dynamics Meeting Abstracts*, pages Gf–03, 1997.

[125] Daniel Howell, Robert P Behringer, and Christian Veje. Stress fluctuations in a 2d granular couette experiment: a continuous transition. *Physical Review Letters*, 82(26):5241, 1999.

[126] CT Veje, DW Howell, RP Behringer, S Schöllmann, S Luding, and HJ Herrmann. Fluctuations and flow for granular shearing. In *Physics of Dry Granular Media*, pages 237–242. Springer, 1998.

[127] H A Janssen. Versuche uber getreidedruck in silozellen. *Z. Ver. Dtsch. Ing.*, 39(35):1045–1049, 1895.

[128] Henning Arendt Knudsen, Bjørnar Sandnes, Eirik Grude Flekkøy, and Knut Jørgen Måløy. Granular labyrinth structures in confined geometries. *Phys. Rev. E*, 77(2):021301, 2008.

[129] Jon Alm Eriksen, Renaud Toussaint, Knut Jørgen Måløy, Eirik Flekkøy, and Bjørnar Sandnes. Numerical approach to frictional fingers. *Phys. Rev. E*, 92(3):032203, 2015.

[130] Arthur Clifford Walshaw and Donald Albert Jobson. *Mechanics of fluids*. Longman, 1962.

[131] Élisabeth Guazzelli and Olivier Pouliquen. Rheology of dense granular suspensions. *Journal of Fluid Mechanics*, 852, 2018.

[132] Samuel H Maron and Percy E Pierce. Application of ree-eyring generalized flow theory to suspensions of spherical particles. *Journal of colloid science*, 11(1):80–95, 1956.

[133] Salvatore P Sutera and Richard Skalak. The history of poiseuille's law. *Annu. Rev. Fluid Mech.*, 25(1):1–20, 1993.

[134] George Gabriel Stokes. On the theories of the internal friction of fluids in motion, and of the equilibrium and motion of elastic solids. 2007.

[135] AY Vorobyev and Chunlei Guo. Multifunctional surfaces produced by femtosecond laser pulses. *Journal of Applied Physics*, 117(3):033103, 2015.

[136] HM Shang, Y Wang, SJ Limmer, TP Chou, K Takahashi, and GZ Cao. Optically transparent superhydrophobic silica-based films. *Thin Solid Films*, 472(1-2):37–43, 2005.

[137] S Hill. Channeling in packed columns. *Chemical Engineering Science*, 1(6):247–253, 1952.

[138] Lincoln Paterson. Radial fingering in a hele shaw cell. *Journal of Fluid Mechanics*, 113:513–529, 1981.

[139] G M Homsy. Viscous fingering in porous media. *Annual Review of Fluid Mechanics*, 19(1):271–311, 1987.

[140] Ruben Juanes, Yue Meng, and Bauyrzhan K. Primkulov. Multiphase flow and granular mechanics. *Phys. Rev. Fluids*, 5:110516, Nov 2020.

[141] Christophe Chevalier, A Lindner, and E Clément. Destabilization of a saffman-taylor fingerlike pattern in a granular suspension. *Phys. Rev. Lett.*, 99(17):174501, 2007.

[142] A. K. Jain and R. Juanes. Preferential mode of gas invasion in sediments: Grain-scale mechanistic model of coupled multiphase fluid flow and sediment mechanics. *Journal of Geophysical Research: Solid Earth*, 114(B8), 2009.

[143] Julie Oppenheimer, Alison Rust, Katharine Cashman, and Bjornar Sandnes. Gas migration regimes and outgassing in particle-rich suspensions. *Frontiers in Physics*, 3, 2015.

[144] Ahmed Jarray, Vanessa Magnanimo, Marco Ramaioli, and Stefan Luding. Scaling of wet granular flows in a rotating drum. In *EPJ web of conferences*, volume 140, page 03078. EDP Sciences, 2017.

[145] Paul Dierckx. *Curve and surface fitting with splines*. Oxford University Press, 1995.

[146] Jon Alm Eriksen, Benjy Marks, Bjørnar Sandnes, and Renaud Toussaint. Bubbles breaking the wall: Two-dimensional stress and stability analysis. *Physical Review E*, 91(5):052204, 2015.

[147] Nian-Sheng Cheng. Formula for the viscosity of a glycerol- water mixture. *Industrial & engineering chemistry research*, 47(9):3285–3288, 2008.

[148] Francisco J Carrillo and Ian C Bourg. Capillary and viscous fracturing during drainage in porous media. *Physical Review E*, 103(6):063106, 2021.

[149] Jacques Duran. *Sands, powders, and grains: an introduction to the physics of granular materials*. Springer Science & Business Media, 2012.

[150] Fernando J Muzzio, Troy Shinbrot, and Benjamin J Glasser. Powder technology in the pharmaceutical industry: the need to catch up fast, 2002.

[151] Eric Dickinson. Food emulsions and foams: Stabilization by particles. *Current Opinion in Colloid & Interface Science*, 15(1-2):40–49, 2010.

[152] Leo C Van Rijn. Sediment transport, part i: bed load transport. *Journal of hydraulic engineering*, 110(10):1431–1456, 1984.

[153] Š Šikalo, H-D Wilhelm, IV Roisman, S Jakirlić, and C Tropea. Dynamic contact angle of spreading droplets: Experiments and simulations. *Physics of Fluids*, 17(6):062103, 2005.

[154] Zhang Shi, Yi Zhang, Mingchao Liu, Dorian AH Hanaor, and Yixiang Gan. Dynamic contact angle hysteresis in liquid bridges. *Colloids and Surfaces A: Physicochemical and Engineering Aspects*, 555:365–371, 2018.

[155] Igor V Kuchin and Victor M Starov. Hysteresis of the contact angle of a meniscus inside a capillary with smooth, homogeneous solid walls. *Langmuir*, 32(21):5333–5340, 2016.

[156] HB Eral, DJCM t Mannetje, and Jung Min Oh. Contact angle hysteresis: a review of fundamentals and applications. *Colloid and polymer science*, 291(2):247–260, 2013.

Appendix A

Instruction of the simulation code

In the simulation, the granular packing is discretized into grid cell, using a two-dimensional array of values, $f_{m,n}$, to represent the normalized filling fraction φ in the cell at each point in space where φ is equal to 1 in compaction front and less than 1 in undisturbed region. The distance of each cell was set to be 0.025 cm, a larger value will speed up the simulation, but fingers will show alignment to underlying square lattice if setting it too high. The code uses a chain of nodes which contain the coordinate information, to represent the interface of the invading fluid. The interface resolution was set to be 0.03cm, and still this value cannot be too high and needs to be much smaller than the finger width. An interface node moves 1/2 of the interface resolution, turn up this value will increase simulation speed at expense of the quality of the results.

To make the concentration field in the simulation more like that in the experiments, we add the noises to the field to mimic the nonuniformity in the real granular packing. We use both noise amplitude and lengthscale to adjust the noise level. The noise amplitude was set to 0.05 and the noise lengthscale was 0.4, increase one of the values can increase the noise level. Noise level cannot be too large otherwise finger growth will have some preference instead of random growth.

The beads concentration field can either be circular or rectangular, and each of them has a corresponding boundary condition. For the circular field, Figure 3.4 b for instance, fingers will stop growing once it touches the boundary. The radius of the circle is free to change to any value. For the rectangular field, Figure 5.10 for instance, finger will keep growing until the whole packing is filled. The width and length of the packing is free to change.

Other free-to-change parameters include plates gap, filling level, injection rate, viscosity of the invading fluid, tilt angle, surface tension, and the density of the grains and the saturated/defending fluid. Different values of the parameters above normally come out different simulation results.

Appendix B

Supplementary images from other experiments

Appendix B will show more images from other experiments than the results in the main body of the thesis, in the same experimental condition or not. One may find some experiments were not finished within the system size and the absence of the experimental results in some conditions. However, they are good enough to achieve the main purpose of this appendix: to show that the experiments are repeatable.

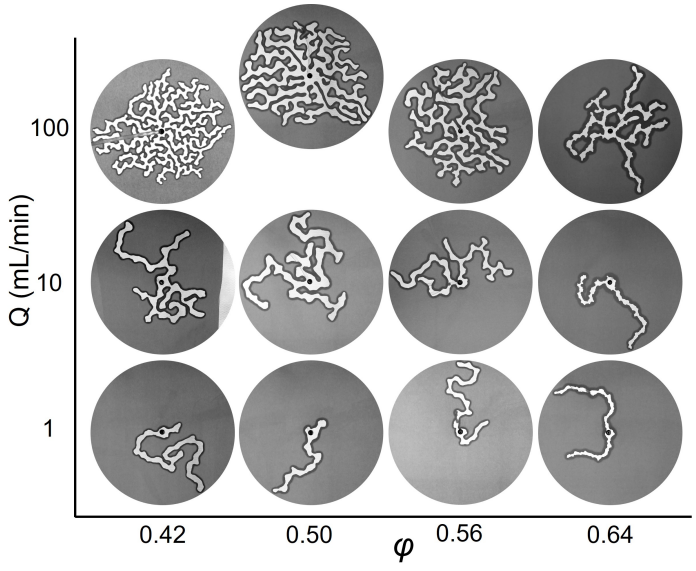

Fig. B.1 Another set of experimental images as shown in Figure 3.4 a. All images are cropped to a circle representing the moment the first finger reached a radius of 13.4 cm. Each disc has a diameter of 26.8 cm. Note that the image at the top row when $\varphi = 0.5$ is not a mistake, the injection rate here is 200 mL/min.

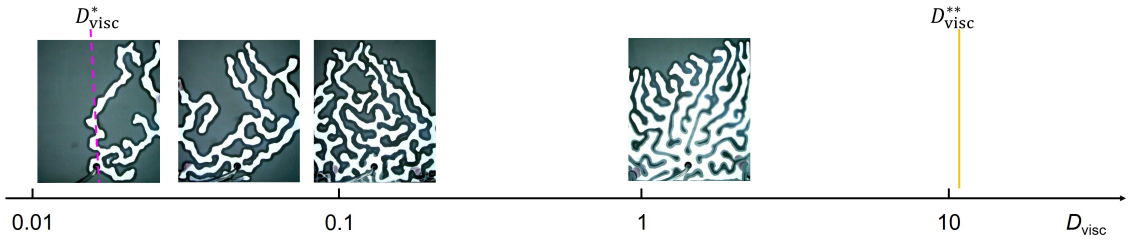

Fig. B.2 Another set of experimental images as shown in Figure 5.3 a. The results at D_{visc} = 0.75, 7.4 and 30.3 are absence. However, the transition from single-fingering to multi-finger has been observed, and there is already a trend of level front at D_{visc} = 2.0.

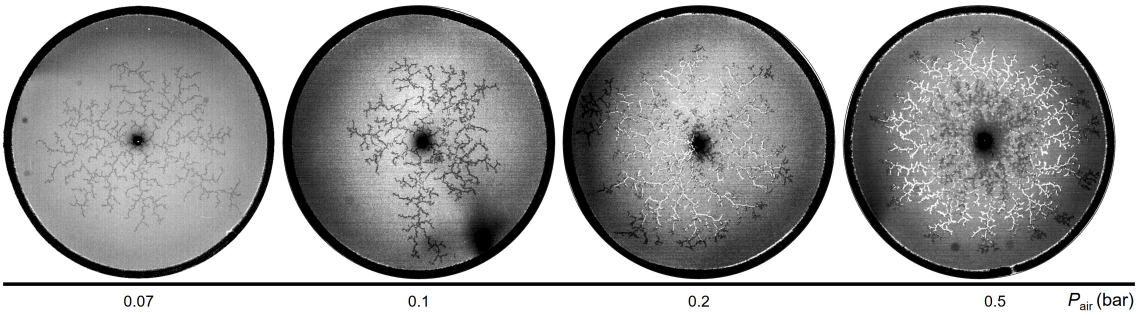

Fig. B.3 More experimental images similar to the images in Figure 6.4 at different air pressure.

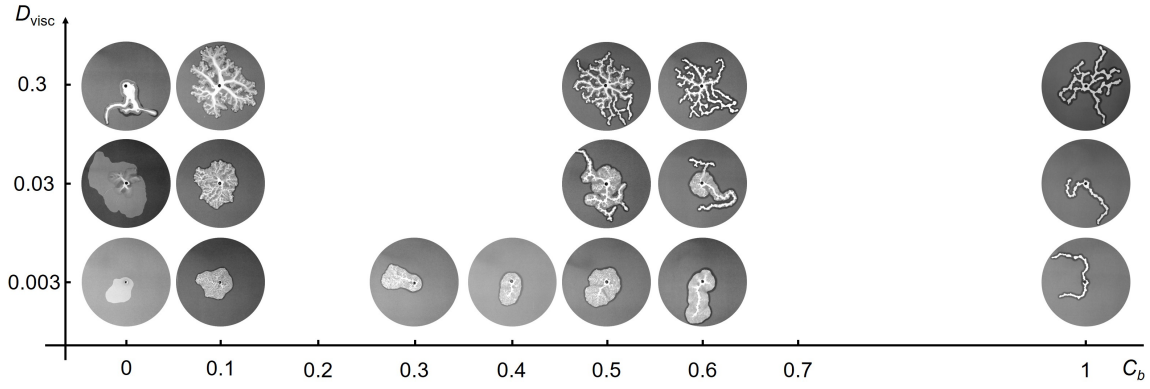

Fig. B.4 Another set of experimental images as shown in Figure 7.3 at different C_b and D_{visc}. Some results especially the results at $D_{visc} > 0.3$ are absent, however there are already sufficient results, such as Figure 7.3 and Figure 7.12 in Chapter 7 to show the repeatability of the experiments.

Appendix C

Descriptions of image processing

In the current thesis, we mainly use the imaging method to record the physics during experiments. We extract the patterns in which we are interested by image processing, and Matlab and Photoshop are the main tools to achieve this. To read the information contained in the images, we normally need to binarize the image and make the region of interest (ROI) white.

To extract the patterns in Chapter 3-5 and Chapter 7, we use 'imsubtract' function to subtract the current frame (or end frame for better illustration) from the starting frame before the experiment is performed. The subtracted image is then convert to grey using 'rgb2gray' which later is binarized using 'imbinarize'. To extract the compaction front, we just need to swap the sequence of the image when doing the image subtracting and other processes are the same. We may also need 'bwareaopen' to delete the white pixels because of the noise in the picture. Photoshop is sometimes used to erase the white regions outside ROI when they are even larger than ROI.

To fill the empty area within the ROI, we can use either 'imfill' or the method below. Firstly , 'imcomplement' is used to convert the white pixels to black and the black pixels to white, then the empty regions within ROI are the white dots surrounded by the black pixels. We can use 'bwareaopen' to delete these dots and use 'imcomplement' again to back the image and make ROI white again but no empty regions. This method is better than simply use 'imfill' in some cases, because we are able to control the size of the empty region to fill and avoid the inlet region being filled.

To calculate the finger width, we use the area of the finger dividing the length of the finger. The area of the finger is obtained using 'regionprops'. The finger is skeletonized using 'bwmorph' and the area of the skeletonized finger is then the length of the finger.

The fracturing patterns in Chapter 6 is harder to extract than those in other chapters. The contrast of the greied picture is normally adjusted using 'adapthisteq' function. A threshold value is set for image binarizing. 'mean2' is used to calculated the average grey level of ROI.